Spintronic terahertz emission: insights and applications

Dissertation

zur Erlangung des Grades eines
Doktors (Dr. rer. nat.)

am Fachbereich Physik
der Freien Universität Berlin

vorgelegt von

Oliver Philipp Gückstock

Berlin, September 2022

Erstgutachter: Prof. Dr. Tobias Kampfrath

Zweitgutachter: Prof. Dr. Georg Woltersdorf

Tag der Disputation: 21. Februar 2023

Abstract[1]

To extend current charge-based electronics by new features and functionalities, the electron spin, as a new degree of freedom, is likely to play a major role in future information technology. Devices using such spin-based electronics (spintronics), for example magnetic random-access memories, are about to enter the market. To be competitive with other information carriers, it is required to push the bandwidth of the elementary spintronic operations to the terahertz (THz) frequency range.

This thesis addresses central open questions regarding ultrafast spin transport in prototypical F|N thin-film stacks. Is ultrafast spin transport mediated by magnons as universal as indicated by previous modelling? What impact does the F/N interface between F and N have on the ultrafast spin-to-charge current conversion (S2C)? How can we exploit spintronic features for new functionalities of spintronic THz emitters (STEs)? By studying spin current dynamics on their natural timescale, one may find new interesting effects or push existing concepts to THz frequencies, which might advance future spintronic applications to work at higher clock rates.

To study ultrafast spin transport in F|N bilayers, we excite them with femtosecond laser pulses. Following absorption of the pulse, a spin current in F is launched and converted into a transverse charge current in N and/or F, giving rise to the emission of a THz electromagnetic pulse. Using this approach, along with an analysis based on symmetry arguments and modeling, the following insights are gained:

First, depending on the conductivity of F, spin currents can be carried by either (i) conduction electrons or (ii) magnons. Remarkably, in the half-metallic ferrimagnet Fe_3O_4 we observe the coexistence of these two spin transport types and disentangle them based on their distinctly different ultrafast dynamics. Our results also indicate that the ultrafast SSE spin current is localized close to the F/Pt interface and its ultrafast dynamics are determined by the relaxation dynamics of the electrons in the Pt layer.

Second, interfaces of metallic heterostructures are known to have a marked impact on the S2C process. We study thin metal films of a ferromagnetic layer F and nonmagnetic layer N with strong and weak spin-orbit coupling. Varying the interface composition allows us to drastically change the amplitude and even invert the polarity of the THz charge current. Symmetry arguments and first-principles calculations strongly suggest that the interfacial S2C arises from skew scattering of spin-polarized electrons at interface imperfections.

Third, we add a functionality to the STE and modulate the polarization of broadband THz electric field pulses at tens of kHz by time-dependent external magnetic field with a contrast exceeding 99 %.

In conclusion, THz emission spectroscopy is a powerful tool to explore and exploit spintronic effects in the ultrafast regime, which will lay the cornerstone for spintronics at THz frequencies.

---

[1] Parts of this abstract have been used in past conference abstracts of our own, some of which are available online.

Kurzfassung

Bei der Weiterentwicklung heutiger Elektronik um neue Funktionen und Funktionalitäten wird der Elektronenspin als zusätzlicher Freiheitsgrad in künftiger Informationstechnologie voraussichtlich eine tragende Rolle spielen. Geräte, die solche spinbasierte Elektronik nutzen (Spintronik), wie zum Beispiel magnetische Random-Access Speicher, stehen kurz vor der Markteinführung. Um mit anderen Informationsträgern konkurrenzfähig zu sein, muss die Bandbreite der grundlegenden spintronischen Operationen auf den Terahertz-Frequenzbereich (THz) ausgeweitet werden.

Diese Arbeit befasst sich mit zentralen offenen Fragen zum ultraschnellen Spintransport in prototypischen F|N-Dünnschichtstapeln. Ist der ultraschnelle, durch Magnonen vermittelte Spintransport so universell, wie es das bisherige Modell nahelegt? Welchen Einfluss hat die F/N-Grenzfläche auf die ultraschnelle Spin-Ladungsstrom-Umwandlung (S2C)? Wie können spintronische THz-Emitter (STEs) um neue Funktionalitäten erweitert werden? Durch die Untersuchung der Spinstromdynamik auf ihrer natürlichen Zeitskala könnten neue Effekte entdeckt oder bestehende Konzepte spintronischer Anwendungen auf THz-Frequenzen ausgedehnt werden.

Um den ultraschnellen Spintransport in F|N-Bilagen zu untersuchen, regen wir diese mit Femtosekunden-Laserpulsen an. Nach Absorption des Pulses wird ein Spinstrom in F erzeugt und in einen transversalen Ladungsstrom in N und/oder F umgewandelt, was zur Emission eines elektromagnetischen THz-Pulses führt. Mit diesem Ansatz und einer Analyse auf der Grundlage von Symmetrieargumenten und Modellen werden die folgenden Erkenntnisse gewonnen:

Erstens können Spinströme, je nach der Leitfähigkeit der F-Schicht, entweder von (i) Leitungselektronen oder (ii) Magnonen getragen werden. Bemerkenswerterweise beobachten wir im halbmetallischen Ferrimagneten Fe_3O_4 die Koexistenz dieser beiden Spintransporttypen und können sie aufgrund ihrer deutlich unterschiedlichen ultraschnellen Dynamik voneinander trennen. Unsere Ergebnisse zeigen auch, dass der ultraschnelle Spin Seebeck-Spinstrom in der Nähe der F/Pt-Grenzfläche lokalisiert ist und seine ultraschnelle Dynamik durch die Relaxationsdynamik der Elektronen in der Pt-Schicht bestimmt wird.

Zweitens die Grenzfläche metallischer Heterostrukturen ist bekannt für ihren Einfluss auf den S2C-Prozess. Wir untersuchen dünne Metallfilme mit einer ferromagnetischen Schicht F und einer nichtmagnetischen Schicht N mit jeweils starker und schwacher Spin-Bahn-Kopplung. Durch Variation der Grenzfläche können wir sowohl die Amplitude drastisch verändern, als auch die Polarität des THz-Ladungsstroms umkehren. Symmetrieargumente und First-Principle Berechnungen legen nahe, dass die S2C an der Grenzfläche durch Skew-Streuung von spinpolarisierten Elektronen an Grenzflächenfehlstellen entsteht.

Drittens erweitern wir den STE um eine Funktionalität und modulieren die Polarisation breitbandiger THz-Pulse bei Dutzenden von kHz durch zeitabhängige externe Magnetfelder mit einem Modulationskontrast größer 99 %.

Zusammenfassend erweist sich THz-Emissionsspektroskopie als leistungsfähiges Instrument zur Erforschung und Anwendung von spintronischen Effekten, die den Eckpfeiler für die THz-Spintronik bilden werden.

Contents

1

Introduction

In a world, where a growing number of people get access to information technology and already extensively make use of them, the hunger for faster, smaller and more energy efficient devices in terms of computational power and communication is constantly growing. This is an excellent, interesting and rich playground for fundamental research in physics – laying the cornerstone for future applications.

Due to the very similar subject matter of this thesis and the thesis by T. S. Seifert [248], this chapter has substantial overlap in terms of the structure and the scientific content.

1.1 Spintronics

Nowadays, conventional electronics are based on encoding binary information by the electron charge as bits (0/1). After decades of meeting the requirements for faster and larger computational power as well as high-density data storage as predicted by Moore's law, the reach of fundamental limits in size and speed ("end of Moore's law") is coming closer [241, 297]. Nevertheless, the demand for faster and more energy-efficient computational devices and storage is constantly growing.

By adding another degree of freedom, the electron spin, one may have the capability to overcome the speed limit, may be increase engergy efficiency and go beyond Moore's law. This research field, called spintronics, may complement conventional electronics one day [21, 216, 238].

Three elementary operations are required to enable the same functional scope as in conventional electrons: (i) writing of magnetic information by turning spins (0/1) around, (ii) transport of spin angular momentum through space and (iii) the generation and detection of spin currents [280, 320]. Recent milestones in generation and detection of spin currents are the discovery of heat-driven spin current generation (Seebeck & Nernst) and spin-dependent Hall effects [24, 259]. The latter can be understood as spin-to-charge current conversion or vice versa and, therefore, also allows for integration of spintronic devices into conventional charge-based electronics.

Two main transport types are possible in spintronics: (a) spin angular momentum can be transmitted by moving spin-polarized electrons through space. (b) the electrons are localized and upon application of a torque to the spins a wave-like transport of spin angular momentum arises. The associated quasi-particle is called magnon [55].

The final vision of spintronics, creating devices and integrating them into existing charge-

based technology, is coming closer. Magnetic random-access memories (MRAMs) are about to enter the market. Here, spin-transfer-torque is used to switch spins and encode information in magnetic layers [164, 284]. Such MRAMs are already announced as in-memory devices or even partially launched by e.g. Samsung [134] and Everspin Technologies Inc., respectively while the next generation based on the more efficient spin-orbit-torque switching, is pushed forward to marketability [215].

Another envisioned step implementing spintronics is the usage of antiferromagnets, which are predicted to have a large potential for higher storage densities and reliability due to the zero net magnetization of these materials [136]. Recently, antiferromagnetic materials, exhibiting a specific combination of symmetry groups, drawn attention of the current research because they combine antiparallel magnetic moments and spin polarized momentum states [261].

Although first devices are about to be implemented in a large scale, there are several unsolved issues like an increase of the spin relaxation rate, which arises in high-spin-orbit-coupling materials. These are needed to be solved for efficient spin-to-charge current conversion [320]. To meet the requirements for faster clock rates, spintronic concepts need to be pushed to ultrafast timescales with speeds in the terahertz frequency range because e.g. the next generations of wireless communication will already work in the terahertz range [105] and beyond for optoelectronic fiber-based technologies [17].

1.2 Terahertz spectroscopy

The terahertz (THz) spectral window ranges from 0.3 to 30 THz [246] which corresponds to wavelengths of 10 to 1000 μm or energies of 1.2 meV to 125 meV and bridges the gap between photonics at hundreds of THz and electronics with frequencies in the gigahertz (GHz) regime [39]. The mentioned photon energies are resonant with many elementary modes: e.g. spin resonances in antiferromagnets, bound electron-hole pairs (excitons), vibrational and rotational motion of molecules [18, 123, 136, 236, 284]. Moreover, spin-orbit-coupling, which is a central aspect of spintronics often has energies at THz frequencies [284].

The THz spectral window is an interesting regime not only from a fundamental perspective, also a number of applications are being developed, such as THz imaging for security scanners at airports or for identifying biological systems like water or biological cells [68, 264]. Another field, where operational speeds are pushed to THz frequencies is wireless telecommunication beyond 5G. This is currently under research and development [74, 105, 147]. To explore the underlying physical effects for these applications, THz time-domain spectroscopy enables the possibility to simultaneously measure amplitude and phase of a THz electric field without any phase retrieval algorithms [211].

While, e.g., dynamics of molecular motion [56] and dynamics of the electronic and lattice dynamics [167, 269, 275] has been extensively studied by THz spectroscopy, the combination of the electron spin degree of freedom and THz spectroscopy is a rather new field and exhibits interesting new developments involving antiferromagnets. Here, the THz pulse

triggers antiferromagnetic dynamics to switch or apply torque to the order parameter, the Néel vector [204].

1.3 Spin currents at THz frequencies

Pushing spintronics operating speeds to the ultrafast regime likely defines the next generation of spintronics – bridging the gap between electronics and photonics. Therefore, one need to study light-matter interactions triggered by THz pulses as mentioned above or proof known spintronic effects to be still operative at THz frequencies. Therefore, THz emission spectroscopy is an excellent tool to study the latter e.g. ultrafast spin transport in spintronically interesting materials and prototypical bilayer systems [138, 280].

Important results from the last decade are, e.g., that the spin Hall effect is still operative at THz frequencies [138] and that conduction-electron mediated as well as magnon-mediated spin transport exists. Both transport channel effects turned out to be heat-driven effects due to the observation of their dynamics at their natural time scales [231, 250]. Moreover, the role of temperature [175, 197], defects [196], film thickness [79, 219], strain [157] or intermediate layers [159, 239, 252] in spin transport as well as details of spin-to-charge current conversion [49, 107, 163, 165, 177, 287, 309, 311, 317] are intensively studied.

Interestingly, combining optically induced heat-driven spin currents with ultrafast spin-to-charge current conversion in metallic heterostructures paved the route to a novel class of THz sources [246]. These spintronic terahertz emitters (STE) have several advantages compared to classical THz emitters based on semiconductors or optical rectification in crystals: they are spectrally broadband without absorbing resonances, more efficient, scalable, mechanically flexible and integrable on-chip [117, 246, 247, 298].

Although spintronic THz emitters are already working excellently and used in several labs, many fundamental questions remain open: What impact does the interface between magnet (source) and non-magnet (converter) have? Is the ultrafast spin transport mediated by magnons as universal as indicated by previous modeling [250]? What is the impact on the
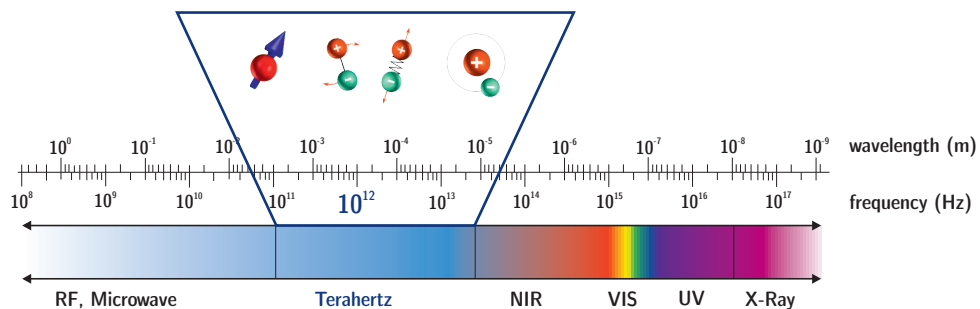
Figure 1.1. | Electromagnetic spectrum. The terahertz window sits in between the microwave and near-infrared (NIR) regime. The small pictograms show exemplary a few fundamental modes, which are accessible by the photon energies of THz electric fields: electron magnetic moments (spins), rotational and vibrational motion of molecules and bound electron-hole states (excitons) – from left to right. Figure is taken from Ref. [98] and redrawn from Ref. [245] with permission of T. S. Seifert.

spin transport in magnetically complex systems like antiferromagnets? How can we take advantage of spintronic features of these THz sources to explore new functionalities?

1.4 Thesis structure

The aim of this thesis is twofold: (i) a deeper understanding of certain fundamental aspects of spintronic effects associated with (ii) applications for spintronic THz emitters. Gaining more insights will likely allow one to optimize spintronic THz sources in terms of their amplitude and bandwidth and as well as to add functionalities to establish them as versatile THz emitters.

The following chapters 2 and 3 deal with the conceptual background and experimental methods of this thesis, respectively. In chapter 4, we focus on two possible generation mechanisms of spin currents and, thus, THz electric fields in spintronic heterostructures: (i) the ultrafast spin Seebeck effect (SSE), where we compare different magnetic insulators with varying thickness and growth methods and reveal that the dynamics of the ultrafast SSE are only governed by the thermal dynamics of the attached Pt layer and are, therefore, universal for any magnetic insulators. (ii) The other usually dominating mechanism is the pyro-spintronic effect (PSE) in electrically conductive magnets. Here, we gain fundamental insights into conduction-electron-mediated (PSE) and magnon-mediated spin transport (SSE) accessible by tuning the electrical conductivity of the magnetic layer. We find a co-existence of both types of spin currents in the half metal magnetite.

Chapters 5 and 6 deal with the second important ingredient for THz emission in metallic bilayer systems: ultrafast spin-to-charge current conversion (S2C). First, the influence of the interface is studied and we observe strong S2C contributions from the interface compared to bulk S2C in the magnetic or non-magnetic layer. We explain our findings by spin-dependent (skew) scattering on impurities in the interface region. Second, the anti-ferromagnetic material IrMn is inserted between a ferromagnetic and non-magnetic layer to gain knowledge about the ultrafast S2C and spin transport length in this spintronically interesting material at GHz and THz frequencies.

Chapter 7 shows an important application of spintronic THz emitters. By applying external time-dependent magnetic fields we are able to modulate the polarity and with assistance of a perpendicularly-oriented static magnetic field even the direction of the emitted THz polarization at tens of kilohertz.

Finally, chapter 8 gives an outlook, where spintronic terahertz emitters are irradiated by gamma-radiation and protons – the most critical types of radiation in space applications. Our findings indicate that spintronic terahertz sources are robust against such high-energy perturbations and, therefore, might be suitable sources for terahertz spectrometer in space missions, e.g. to Mars.

Conceptual background

This chapter aims at providing the necessary theoretical background to comprehend the main chapters of this thesis in a didactical manner: from a single particle picture and their interactions to collective phenomena like magnetic order and (ultrafast) spin transport. Finally, all relevant light-matter interactions will be presented.

Due to the very similar subject matter of this thesis and the thesis by T. S. Seifert [248], this chapter has substantial overlap in terms of the structure and the scientific content.

2.1 Electrons in crystalline solids

In this thesis, we study thin-film samples particularly important for spintronics, which can be considered as crystalline solids on at least a local level. Thus, the dynamics of electrons in solids can be determined by three degrees of freedom: the electron spin, the electron orbital motion and the crystal lattice, where the latter is often represented by its quasi-particle, the phonon. In the following, we briefly describe electrons in a solid.
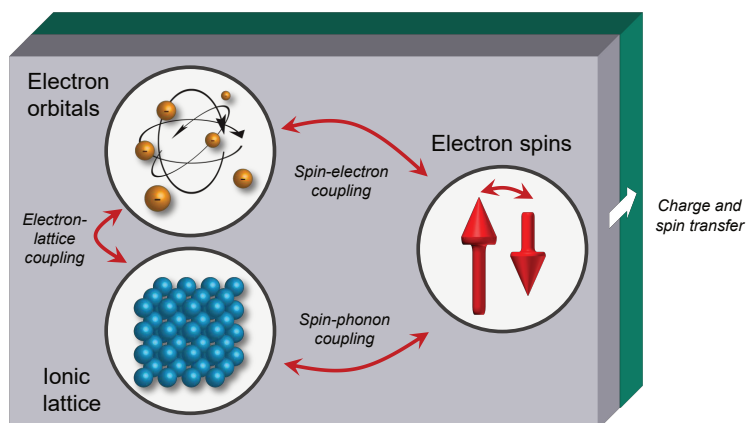

Figure 2.1. | Subsystems of condensed matter. Schematics of the three baths: ionic lattice, the electron orbitals and spins. Examples of interaction types between the subsystems are depicted by the red arrows. Figure redrawn from Ref. [168] with permission of S. F. Maehrlein.

Bloch electrons

To accurately capture the properties and interactions of electrons in solids, one requires a many-electron Hamiltonian that can already represent any complex problem in physics. For a simplified description one requires theoretical models. One important example is the model of independent electrons, where each electron moves in an effective single-electron potential. This reduces the problem to a single-electron Hamiltonian.

To describe how electrons can propagate through or be excited in a solid, we briefly introduce what a crystalline solid is. Here, the term crystal structure refers to a periodical arrangement of atoms forming different crystal classes such as cubic, hexagonal or tetragonal [146]. It can be generated by periodically repeating a spatial pattern, the so-called unit-cell. The unit cell with the smallest number of atoms is called primitive unit cell. It has a finite number of atoms at sites i and distance a to each other, where a is known as the lattice parameter [146]. This periodic pattern of atoms and the resulting discrete translational symmetry have a far-reaching consequence for the movement of electrons inside this crystal lattice. In the independent-electron model, the effective potential becomes also spatially periodic and these electrons are called Bloch electrons [146]. It follows that the wavefunction of a Bloch electron fulfills the Bloch theorem

$$\Psi_{n,k}(\boldsymbol{r}) = e^{i\boldsymbol{k}\boldsymbol{r}}u_k(\boldsymbol{r}), \tag{2.1}$$

where the electron sits at position $\boldsymbol{r}$ and $e^{i\boldsymbol{k}\boldsymbol{r}}$ is a plane wave with $\boldsymbol{k}$ denoting the crystal momentum. u_k is a periodic function reflecting the periodicity of the crystal. For metals, u_k is approximately constant, which justifies to consider plane waves while for insulators u_k is localized at ions in the ground state. The solutions $\Psi_{n,k}$ are named Bloch waves [146].

The index n, the so-called band index, indicates that multiple solutions of the Schrödinger
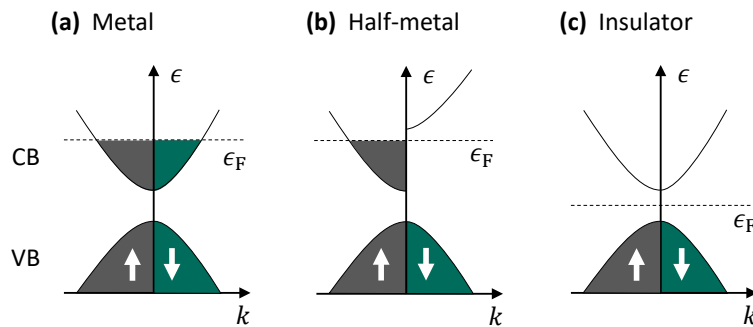
Figure 2.2. | Schematic band structure for different solids. (a) In metals, the Fermi energy ϵ_F lies in the conduction band (CB) allowing occupation of states while the valence band (VB) is fully filled. **(b)** The band structure becomes more complicated in half-metals where the position ϵ_F lies, as in metals, in the CB but the band is energetically shifted for spin up and spin down, depicted by the white arrows. **(c)** For ϵ_F lying inside the band gap, no states of the CB are occupied. This type of solids is called insulator.

equation exist, which form energy bands with energies $\varepsilon_{n,k}$ instead of discrete energy levels as in atoms. Fig. 2.2 shows schematic representations of energy bands for a metal, half-metal and insulator.

Consequently, Bloch electrons also show different properties than free electrons. For example, their group velocity can be shown to be $\boldsymbol{v} = \hbar^{-1} d\varepsilon_{n,k}/d\boldsymbol{k}$ with $\hbar$ denoting the reduced Planck constant ($\hbar = h/2\pi$) and thus depends on the band curvature [146].

Fermi-Dirac statistics

To describe the population of the energy bands, one uses Fermi-Dirac statistics since electrons are Fermions. Accordingly, the Pauli exclusion principle demands electrons to differ in at least one quantum number, which results in a maximum energy, the Fermi energy ϵ_F, for which electrons can occupy the energy bands at temperature $T = 0\,\mathrm{K}$.

Since the energy bands $\varepsilon_{n,k}$ as a function of k may not cover all energies, energetic band gaps form. The uppermost partially filled band is called the conduction band (CB) while the lower bands are called valence bands (VB). By the position of ϵ_F we can easily distinguish between metals with ϵ_F in the conduction band and insulators with ϵ_F inside the band gap [Fig. 2.2(a) and 2.2(c)]. Another, in this thesis important class of materials are half-metals, where the position of ϵ_F allows for occupation of electrons in the conduction band but just for one spin species [Fig. 2.2(b)]. Details on this schematic representation of spin-dependent density of states can be found in section 2.3.2.

The exact occupation of electrons in the states above ϵ_F for an arbitrary given electron temperature T is given by the Fermi-Dirac distribution [146]

$$f(\epsilon, \mu, T) = \frac{1}{1 + \exp[(\epsilon - \mu)/k_B T]}, \tag{2.2}$$

with μ being the chemical potential, which is the conjugate variable of the mean number of electrons constant. For $T = 0$, the chemical potential μ equals the Fermi energy ϵ_F. Further, we see that the occupied states are approximately separated by an energy interval of about $k_B T$ [146].

2.2 Spin interactions

2.2.1 Spin angular momentum

In this section, we will briefly discuss what spin angular momentum is and, more importantly, how spin angular momentum can interact with its surrounding. Basically, an electron has two types of angular momentum: an orbital momentum L and in addition an intrinsic contribution S that is called electron spin [199], resulting in total angular momentum $J = L + S$. L is due to orbital motion and classically, one can imagine S to arise from the rotation of the sphere-like classical electron about an axis through its center

of mass. Thus, the electron spin induces a magnetic moment

$$\hat{\boldsymbol{\mu}}_{\mathrm{S}} = -\frac{g_e \mu_{\mathrm{B}}}{\hbar}\hat{\boldsymbol{s}}, \tag{2.3}$$

with g_e denoting the electron g-factor which amounts to approximately 2. Further, μ_{B} is the Bohr magneton that is the magnetic moment an electron generates by its orbital and spin angular momentum [199]. A proper theoretical justification of the electron spin requires relativistic quantum mechanics, for example, the Dirac equation. This is a co-variant Schrödinger equation and involves so-called spinors instead of scalars and scalar wave functions, respectively [199, 263]. In 1929 Nevill Francis Mott published his results on spin-dependent scattering of electrons off heavy nuclei, nowadays known as Mott-scattering [184]. This marks the first experimentally direct evidence of spin angular momentum.

Comparable to the quantum mechanical operator of the orbital angular momentum $\hat{\boldsymbol{l}}$ we can define a spin operator $\hat{\boldsymbol{s}}$ that obeys to the same relations as $\hat{\boldsymbol{l}}$. Thus, we define a commutation relation of the spin angular momentum by

$$[\hat{s}_i, \hat{s}_j] = i\hbar\epsilon_{ijk}\hat{s}_k, \tag{2.4}$$

with the Levi-Civita symbol ϵ_{ijk} [199]. Usually, one uses a set of eigenstates of commuting operators $\hat{\boldsymbol{s}}^2$ and $\hat{s}_z$ as basis of the spin-subspace [248] with eigenvalues of $\hbar^2 S(S+1)$ and $\pm\hbar S$, respectively. Here, S denotes the spin quantum number, which is $S = 1/2$. For the latter eigenvalue $\pm\hbar S$, one usually calls the two possibilities "spin up" and "spin down" with respect to the z-axis [199].

2.2.2 Relativistic single-electron Hamiltonian

Since we are interested in magnetic phenomena due to ordered spins, we need to consider a Hamiltonian with relativistic corrections because the electron spin is not covered in the classical Schrödinger wave equation (see section 2.2.1) [294]. Taking the expansion of the Dirac Hamiltonian up to the first order in $1/c$, the relativistic Hamiltonian of a single electron is given by [199]:

$$\hat{H}_{\mathrm{rel}} = \hat{T} + \hat{T}_{\mathrm{rel}} + \hat{H}_{\mathrm{C}} + \hat{H}_{\mathrm{Darwin}} + \hat{H}_{\mathrm{Z}} + \hat{H}_{\mathrm{SO}}, \tag{2.5}$$

where $\hat{T}$ and $\hat{T}_{\mathrm{rel}}$ are the kinetic energy and its relativistic correction, respectively. $\hat{H}_{\mathrm{C}}$ describes the Coulomb interaction and the forth term $\hat{H}_{\mathrm{Darwin}}$ is the Darwin term characterizing an interaction between an external electric field $\hat{\boldsymbol{E}}$ and the magnetic moment $\hat{\boldsymbol{\mu}}$ of an electron that is proportional to $(\hat{\boldsymbol{E}} \times \hat{\boldsymbol{\mu}})^2$. This correction term to the Coulomb interaction is also known as Zitterbewegung and usually negligible compared to the other terms in Eq. (2.5) [294, 308]. The remaining two terms $\hat{H}_{\mathrm{Z}}$ and $\hat{H}_{\mathrm{SO}}$ are discussed in more detail in the following sections.

Zeeman interaction

The term $\hat{H}_Z$ is called Zeeman interaction. It is of great importance for light-matter interaction and, especially, for the research in magnetism as well as applications in spintronics because the Zeeman interaction describes how a classical external magnetic field $\hat{\boldsymbol{B}}$ couples to the magnetic moment $\hat{\boldsymbol{\mu}}$ of an electron [263]. Under the assumption of small magnetic fields compared to other spin-dependent interactions, the Zeeman interaction is given by [199]

$$\hat{H}_Z = -\hat{\boldsymbol{\mu}}_e \cdot \hat{\boldsymbol{B}}. \tag{2.6}$$

We note that the magnetic moment of an electron consists of two contributions $\hat{\boldsymbol{\mu}}_e = \hat{\boldsymbol{\mu}}_{\mathrm{orb}} + \hat{\boldsymbol{\mu}}_s$ where $\hat{\boldsymbol{\mu}}_{\mathrm{orb}}$ denotes the orbital magnetic moment and $\hat{\boldsymbol{\mu}}_s$ is the spin magnetic moment.

Spin-orbit interaction

In general, as the name already says, this interaction describes how spin and orbital moments are coupled and is responsible for the magnetocrystalline anisotropy whereas the exchange interaction (see section 2.3), as quantitatively largest interaction, is isotropic [263]. We consider an electron with band velocity $\hat{\boldsymbol{v}}_e$ and an electric field $\boldsymbol{E}$ at position $\hat{\boldsymbol{r}}$ of the electron. Then, it can be shown that the Hamiltonian of spin-orbit interaction is given by [248]

$$\hat{H}_{\mathrm{SO}} = \frac{\mu_{\mathrm{B}}}{c\hbar} \hat{\boldsymbol{s}} \cdot \left(\boldsymbol{E}(\hat{\boldsymbol{r}}) \times \frac{\hat{\boldsymbol{v}}_e}{c} + \frac{i\hbar}{2cm_e}(\boldsymbol{\nabla} \times \boldsymbol{E})(\hat{\boldsymbol{r}}) \right). \tag{2.7}$$

We see that the Hamiltonian consists of two terms, where the second one is contributing only in the case of time-dependent magnetic fields. Thus, we restrict this discussion to stationary magnetic fields resulting in a vanishing second term because then $\boldsymbol{\nabla} \times \boldsymbol{E} \propto \dot{\boldsymbol{B}}$ equals zero.

The first term is what one usually knows as spin-orbit interaction and describes the coupling of a spin $\hat{\boldsymbol{s}}$ to an effective magnetic field $\hat{\boldsymbol{B}}_{\mathrm{eff}}$, which is proportional to $\hat{\boldsymbol{E}} \times \hat{\boldsymbol{v}}_e$. The spin-orbit interaction Hamiltonian then finally reads

$$\hat{H}_{\mathrm{SO}} \propto \hat{\boldsymbol{s}} \cdot \hat{\boldsymbol{B}}_{\mathrm{eff}}. \tag{2.8}$$

We see that $\hat{H}_{\mathrm{SO}}$ is in full analogy to the Zeeman interaction as shown above. An intuitive picture of spin-orbit interaction can be given, if we change the frame of reference to the electron. Here, the electron "sees" the nucleus moving with velocity $\boldsymbol{v}_e$, which implies a charge current and, thus, an effective magnetic field $\boldsymbol{B}_{\mathrm{eff}}$ [Fig. 2.3].

As equation (2.7) shows, $\boldsymbol{E}$ depends on the electron position $\boldsymbol{r}$, effectively the distance to the nucleus. If we now consider a spherically electric potential, one can relate the effective magnetic field to the orbital momentum by $\boldsymbol{B}_{\mathrm{eff}} \propto \boldsymbol{r} \times \boldsymbol{v}_e \propto \boldsymbol{l}$ and we can obtain the textbook appearance of the spin orbit interaction (SOI):

$$\hat{H}_{\mathrm{SO}} = \lambda \hat{\boldsymbol{l}} \cdot \hat{\boldsymbol{s}}, \tag{2.9}$$
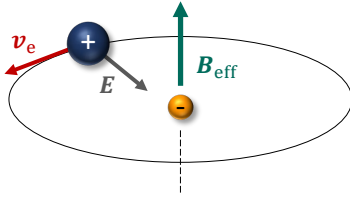
Figure 2.3 | Spin-orbit interaction. In the frame of reference of the electron (orange sphere), the nucleus (blue sphere) is moving with the band velocity $\boldsymbol{v}_e$ generating an electric potential $\boldsymbol{E}$ between the electron and itself. This creates an effective magnetic field $\boldsymbol{B}_{\mathrm{eff}}$ which is experienced by the electron and couples to its spin, known as spin-orbit coupling. Figure redrawn from Ref. [168] with the permission of S. F. Maehrlein.

where $\lambda = \mu_{\mathrm{B}} \hbar^{-1} c^{-2} m_e^{-1} r^{-1} E(r)$ denotes the spin-orbit parameter [199].

Finally, we first estimate the energy of the spin-orbit interaction under the assumption of a static vector potential to be in the order of $\approx 0.1\,\mathrm{meV} \cdot Z^4$ [11] with the atomic number Z. This is already close to the THz frequency range with energies in the order of $4.1\,\mathrm{meV}$ for $1\,\mathrm{THz}$. Second, we compare the effective magnetic field of spin-orbit interaction to usually available magnetic fields in table-top experiments. Here, the effective field lies in the order of $\approx 4\,\mathrm{Tesla} \cdot Z$, which is much higher than what people normally achieve with external magnetic fields in labs [248]. However, also the magnetic field component of electromagnetic radiation can be large. For THz electric fields it is on the order of $1\,\mathrm{T}$ for the highest achievable field strengths [138, 254].

2.3 Magnetism in solids

2.3.1 Many-electron relativistic Hamiltonian

Magnetic order is a collective many-electron phenomenon. We, thus, extend the single-electron Hamiltonian to a many-electron Hamiltonian in its relativistic form, which reads [110]

$$\hat{H}_{\mathrm{ME}} = \sum_i \left(\hat{T}_i + \hat{V}_i + \sum_{j>i} \hat{V}_{ij}^{\mathrm{ee}} \right) + \hat{H}_{\mathrm{rel}}, \tag{2.10}$$

with the kinetic energy $\hat{T}_i$, the potential energy $\hat{V}_i$ for electron i and, to account for the interaction between electrons $(i \neq j)$, a Coulomb electron-electron interaction term $\hat{V}_{ij}^{\mathrm{ee}}$. The terms of $\hat{H}_{\mathrm{ME}}$ also include all electric and magnetic fields, external and internal, caused by the nuclei. Further, this many-electron Breit-Pauli Hamiltonian explicitly contains the total electric and magnetic fields, which are felt by all electrons [110, 248].

Despite the in Eq. (2.5) introduced relativistic contributions, the last term $\hat{H}_{\mathrm{rel}}$ includes also further spin-related terms such as spin-spin magnetic dipole interaction (SSMD). This interaction is comparably small since its energy is on the order of $\approx 1\,\mathrm{meV}$ but nonetheless it causes, e.g., the magnetic shape anisotropy [43]. The corresponding Hamiltonian reads [33]

$$\hat{H}_{\mathrm{SSMD}} = \frac{\mu_0}{4\pi r^3} \left[\hat{\boldsymbol{\mu}}_{\mathrm{s}1} \cdot \hat{\boldsymbol{\mu}}_{\mathrm{s}2} - \frac{3}{r^2} (\hat{\boldsymbol{\mu}}_{\mathrm{s}1} \cdot \hat{\boldsymbol{r}})(\hat{\boldsymbol{\mu}}_{\mathrm{s}2} \cdot \hat{\boldsymbol{r}}) \right]. \tag{2.11}$$

Isotropic exchange interaction

To explain the phenomenon of magnetic ordering, we use the first part of Eq. (2.10) to briefly describe the exchange interaction for a two-electron model. As introduced in section 2.1, both electrons in this simple model need to obey the Pauli exclusion principle and, thus, differ in at least one quantum number. In a contemporary notation, we use the wave function $\Psi(\boldsymbol{r}_1, \boldsymbol{s}_1; \boldsymbol{r}_2, \boldsymbol{s}_2)$, which has to be antisymmetric when exchanging the electrons $(\Psi(\boldsymbol{r}_1, \boldsymbol{s}_1; \boldsymbol{r}_2, \boldsymbol{s}_2) = -\Psi(\boldsymbol{r}_2, \boldsymbol{s}_2; \boldsymbol{r}_1, \boldsymbol{s}_1))$. From this consequence, we can already deduce that a parallel spin alignment $(\boldsymbol{s}_1 = \boldsymbol{s}_2)$ is energetically favored since Ψ becomes zero if also $\boldsymbol{r}_1 = \boldsymbol{r}_2$.

In a model of a covalent bond by Heitler-London [199], one can show that it is sufficient to consider the wave functions as products of spin states. This results in the final exchange interaction Hamiltonian for two spins [294]

$$\hat{H}_{\text{ex}} = \text{const.} - \frac{J_{\text{ex}}}{4\hbar^2}\hat{\boldsymbol{s}}_1 \cdot \hat{\boldsymbol{s}}_2, \tag{2.12}$$

where the exchange constant is defined as $J_{\text{ex}} = E_{\text{singlet}} - E_{\text{triplet}}$ with $E_{\text{singlet}} = E_1 + E_2 + K_{12} + J_{12}$ and $E_{\text{triplet}} = E_1 + E_2 + K_{12} - J_{12}$ [294]. Here, J_{12} is the exchange integral and K_{12} denotes the overlap integral of the two spin states with energies E_i. A more detailed derivation can be found in Refs. [248, 294].

2.3.2 Magnetically ordered solids

Above, it was shown that the exchange interaction can cause a spontaneous ordering of magnetic moments. For solids, we define the magnetization $\boldsymbol{M}$ as [248]

$$\boldsymbol{M}(\boldsymbol{r}) = \frac{1}{V}\sum_i \langle \hat{\boldsymbol{\mu}}_i(\boldsymbol{r})\rangle, \tag{2.13}$$

where $\langle \hat{\boldsymbol{\mu}}_i\rangle$ are the quantum mechanical expectation values of the magnetic moment and V denotes a small averaging volume of the solid. Macroscopically, one can find different types of spin ordering resulting in a net magnetization $\boldsymbol{M}$. The simplest magnetic order is achieved in ferromagnets, where all spins are parallel aligned and point into the same direction [Fig. 2.4(a)]. The ordering type, which is known as antiferromagnetic order consists of two sublattices with antiparallel aligned spins compensating each other [Fig. 2.4(c)]. Here, no net $\boldsymbol{M}$ is present. As shown in Fig. 2.4(b), we have a third type, which is the ferrimagnetic order, in which similar to antiferromagnets two sublattices with oppositely aligned spins exists but having a different amount of spins in one of the sublattices. This results in a net magnetization $\boldsymbol{M}$.

$\boldsymbol{M}$ is largely carried by the spin magnetic moment in ferromagnets such as Fe, Co and Ni, while the orbital magnetic moment (see section 2.2.2) is only approximately $10\,\%$ contributing to the total $\hat{\boldsymbol{\mu}}$ [263]. Other types of magnetic moments are orders of magnitude smaller than the electron spin magnetic moments [248, 263]. In the following, we will look at two models, which try to describe magnetic ordering. First, the Heisenberg model in
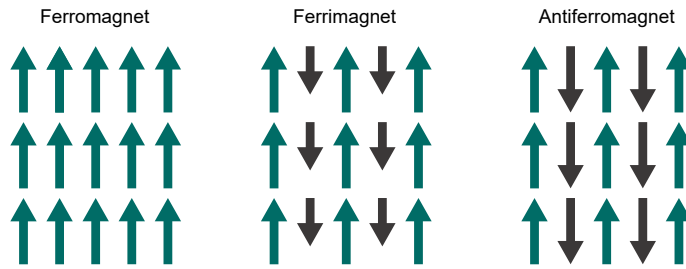
Figure 2.4. | Types of magnetic order. **(a)** In a ferromagnet, all spins are aligned parallel to each other whereas in **(b)** ferrimagnets, the spin system consists of two sublattices with antiparallel aligned spins but different number of spins per sublattice. **(c)** If the number of spins per sublattice is same, there is no net magnetization and the system is called antiferromagnet.

the limit of localized moments and second, in the case of itinerant moments the Stoner model has proven its usefulness.

Heisenberg model

The Heisenberg model has proven to be quite successful in describing magnetic phenomena such as the exchange interaction in, e.g., insulators by assuming localized electrons at a lattice site α [294]. Following the many-electron Hamiltonian, the exchange interaction in the Heisenberg model reads in a generalized version of Eq. (2.12) as [294]

$$\hat{H}_{\mathrm{ex}} = \mathrm{const.} - \frac{1}{\hbar^2} \sum_{\alpha > \alpha', n, n'} J_{\mathrm{ex}}^{nn', \alpha\alpha'} \boldsymbol{S}_\alpha \cdot \boldsymbol{S}_{\alpha'}, \tag{2.14}$$

with the total electron spin $\boldsymbol{S}$ at each α with the electron in the orbital state n [248]. Since we discuss a many-body model, in which expectation values are the physical observables, we simplify our notation here by replacing the quantum mechanical operators with their expectation values [294]. To simplify the situation even further, we (i) neglect the constant term in Eq. (2.14) since it contains only spin-independent contributions. And (ii), we limit H_{ex} to spin interactions of nearest neighbors. This restriction is justified because the overlap of the electronic wave functions decays exponentially and, thus no long-range exchange interactions will contribute significantly to H_{ex}. Then, the simplified, effective Heisenberg exchange interactions is given by [199]

$$\hat{H}_{\mathrm{ex}}^{\mathrm{eff}} = -\frac{J_{\mathrm{ex}}}{\hbar^2} \sum_{\alpha > \alpha'} \boldsymbol{S}_\alpha \cdot \boldsymbol{S}_{\alpha'}. \tag{2.15}$$

The exchange constant J_{ex} can, despite from quantifying the strength of the nearest neighbor interaction, also provide another information. Depending on its sign, different magnetic order types are assigned to it. If $J_{\mathrm{ex}} > 0$, a parallel spin orientation will occur, and according to the previous section, we call this type of magnetic order ferromagnetic [see Fig. 2.4(a)]. For $J_{\mathrm{ex}} < 0$, the spins will align antiparallel resulting in a ferri- or antiferromagnetic order [see Fig. 2.4(b)-(c)] [199].

Note that in metallic magnetic systems, where electrons are delocalized above the Fermi energy, the Heisenberg model may fails. However, one can often transfer the description of the Heisenberg Hamiltonian to an effective Hamiltonian for metals. While the Heisenberg exchange interaction is a direct coupling of spins, there are also other indirect coupling mechanisms in insulators as well in metals such as super exchange, double exchange, sd-exchange or Ruderman-Kittel-Kasuya-Yosida (RKKY) exchange [199].

Stoner model

In contrast to the Heisenberg model, the Stoner Model is the simplest model to describe magnetic order in metals, e.g., solids with itinerant electrons, which are treated as nearly free moving particles [181]. In the Stoner model, we make three basic assumptions: (i) the magnetic moments of classical ferromagnets like Fe, Co and Ni are dominated by electrons in the d-shell and form energy bands due to periodic bonds between the spins. (ii) A mean exchange field shifts the bands for spin up and spin down relative to each other by ΔE_{ex} and (iii) the electrons obey Fermi statistics with energy bands filled to the Fermi energy ϵ_{F} as depicted in Fig. 2.5 [181, 263].

These assumptions already explain well how a spontaneous magnetization in ferromagnets arises. Due to ΔE_{ex}, the bands for spin up and spin down are asymmetrically populated and give rise to a net magnetization $\boldsymbol{M}$ [248]. For metals, the band splitting ΔE_{ex} is experimentally found to lie usually in the order of $1\,\mathrm{eV}$ [181]. Lastly, charge currents can get spin-polarized when propagating through a magnetic solid when s-electrons, which dominate the conduction due to a higher mobility, interact with the delocalized d-electrons [43].
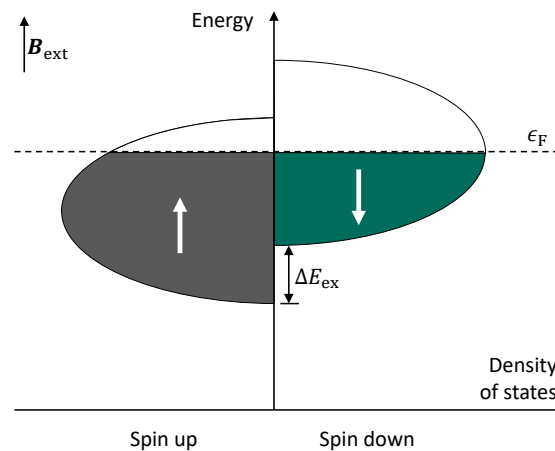
Figure 2.5. | Stoner model for a ferromagnet. The simplified schematic shows the density of states of a ferromagnet with only d-like bands under the influence of an external magnetic field $\boldsymbol{B}_{\mathrm{ext}}$. The bands for spin up and spin down are filled with electrons up to the Fermi energy ϵ_{F} and are split by the exchange energy ΔE_{ex}. This splitting leads to an imbalance of spin up and down electrons and, thus, to a net spin polarization of the ferromagnet. Figure redrawn from Ref. [248] with permission of T. S. Seifert.

Critical temperature

The critical temperature T_{crit} describes the point where a magnetically ordered material loses its magnetization and, thus, makes a transition into the paramagnetic phase [146, 263]. As seen above, magnetic order arises among others due to exchange coupling of neighboring spins. Then, often T_{crit} is introduced by spontaneous magnetization in the Heisenberg model and its consequence to have a critical temperature, where the exchange interaction competes with other energies in the solid [146, 248].

For a more hand-waving picture to describe the existence of T_{crit}, the Stoner picture with its assumed Fermi statistics description may be useful. Here, it is obvious that the net magnetization $\boldsymbol{M}$ strongly depends on the temperature T [263]. Consequently, there exists a critical point, in which the temperature is high enough to cause spin flips from the spin up to spin down bands and, thus, lose $\boldsymbol{M}$.

Note that the Stoner model is not free of assumptions and, therefore, fails in the precise explanation of the critical temperature but gives an intuitive picture of the situation [263]. The critical temperature in ferro- and ferrimagnets is called Curie temperature T_{C} while in antiferromagnets it is named Néel temperature T_{N}. The relationship between M and T_{crit} is often found to be $M \sim (T_{\mathrm{crit}} - T)^{\beta}$ with β denoting a critical exponent [263].

Magnetic anisotropy and hysteresis

The local magnetization in a magnet tends to lie in a preferred direction to minimize its total energy. The magnetic anisotropy describes how much energy is needed to rotate the magnetization from a favored (easy) reference direction to any other axis. Microscopically,
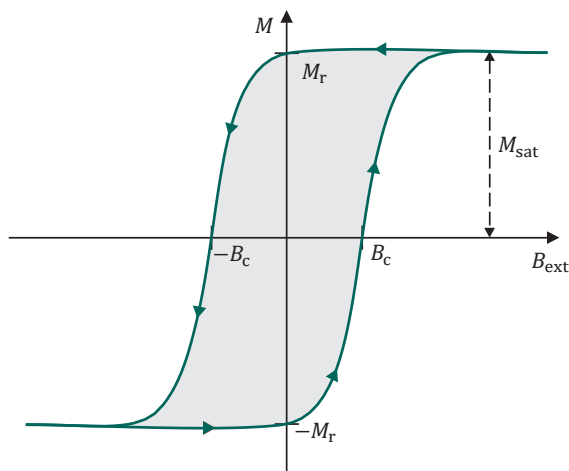

Figure 2.6. | Hysteresis loop. Hysteretic behavior of the magnetization M depending on an external magnetic field B_{ext} in a magnetically ordered material. Without any applied B_{ext} the magnetization remains at a value M_{r}, the remanence, whereas the external magnetic field required to fully demagnetize the material is called coercive field B_{c}. The maximum achievable magnetization is depicted by the dashed arrow and known as the saturation magnetization M_{sat}. Figure redrawn from Ref. [98].

it arises from SOI and SSMD in conjunction with the crystalline structure (mainly via SOI), the shape of the magnetic material (mainly via SSMD), interfaces, strain or stress [263]. As a consequence of energy minimization, magnets form magnetization domains without externally applied magnetic fields to minimize their stray fields, exchange and anisotropy energies [263]. Under the influence of an external magnetic field, the magnet uniformly aligns its spin parallel to the direction of the external field and, thus, forms a single domain.

The response of a magnetic material to an external magnetic field B_{ext} often shows a hysteretic behavior. Every externally applied magnetic field will apply torque on all non-parallelly oriented spins to align them. Once all spins are well aligned and a single domain is formed, the magnetization reaches its maximum and saturates, known as saturation magnetization M_{sat} [Fig. 2.6]. When B_{ext} is removed, a non-zero magnetization survives, the remanence M_r. To fully demagnetize the magnetic material, one needs a B_{ext} with an amplitude of B_c, the coercive field [Fig. 2.6]. As explained above, the magnetic anisotropy has a major influence on the energy, which is needed to change the net magnetization and, thus, the shape of the hysteresis loop [263].

2.4 Spin dynamics

2.4.1 Spin precession and damping

After we discussed magnetism in equilibrium, we now describe the dynamics of spins, which are required for elementary spintronic operations like switching of spins. The Ehrenfest theorem

$$\frac{\mathrm{d}}{\mathrm{d}t}\langle\hat{\boldsymbol{s}}\rangle = \frac{\mathrm{i}}{\hbar}\langle\left[\hat{H},\hat{\boldsymbol{s}}\right]\rangle \tag{2.16}$$

is the starting point for this derivation since it gives the time evolution of a specific operator, here the spin operator $\hat{\boldsymbol{s}}$. The brackets $\langle...\rangle$ denote the quantum mechanical expectation value and $\hat{H}$ is the single electron Hamiltonian. For simplicity, we first limit this discussion to a specific case where an external magnetic field interacts with an electron spin. Therefore, we consider the Zeeman interaction as dominating interaction. It can be shown that the spin dynamics are then given by [248]

$$\frac{\mathrm{d}}{\mathrm{d}t}\langle\hat{\boldsymbol{s}}\rangle = -\frac{g_e\mu_B}{\hbar}\langle\hat{\boldsymbol{s}}\rangle \times \boldsymbol{B}_{ext}(t). \tag{2.17}$$

Equation (2.17) delineates an undamped precession of the spin around the magnetic field $\boldsymbol{B}_{ext}(t)$ with frequency $\omega_L = \mu_B B_{ext}/\hbar$ that is known as Lamor frequency [248].

The general case is much more complex than introduced above and seen in the many-body Hamiltonian H_{ME}, where additional terms such as isotropic and anisotropic exchange, demagnetization and magneto-elastic contributions can occur [294]. We thus simplify matter considerably in the following by replacing all quantum mechanical operators ($\langle\hat{\boldsymbol{s}}\rangle$) with their expectation values $\boldsymbol{s}$. Further, we find that $\boldsymbol{B}_{ext}$ in Eq. (2.17) is replaced by

an effective magnetic field

$$\boldsymbol{B}_{\text{ext}} = \frac{\hbar}{g_e \mu_{\text{B}}} \frac{\partial H(\boldsymbol{s})}{\partial \boldsymbol{s}}, \tag{2.18}$$

with $H(\boldsymbol{s})$ denoting the spin-dependent energy of the system [170] for a spin at site i. This effective field allows torques to act on the spin, which will influence also neighboring spins [173].

So far, we discussed an undamped system, which is rather unphysical. At some point in time the spin will return to its equilibrium position. Therefore, we have to introduce a damping term to Eq. (2.17) by considering three different baths with which the spin can interact: other spins, the lattice and an electron orbital degree of freedom [Fig. 2.1] [75]. As seen in Fig. 2.1 a spin cannot just interact with the other baths, also the lattice or orbital degree of freedom have back interactions to the spin system. This backaction can alter the effective field $\boldsymbol{B}_{\text{eff}}$, which reads then

$$\boldsymbol{B}_{\text{eff}} \to \boldsymbol{B}_{\text{eff}} + \Delta \boldsymbol{B}_{\text{eff}}. \tag{2.19}$$

$\Delta \boldsymbol{B}_{\text{eff}}$ depends on whole history of $\boldsymbol{s}(t)$ and other observables. In the simplest phenomenological approach, $\Delta \boldsymbol{B}_{\text{eff}}$ can be written as

$$\Delta \boldsymbol{B}_{\text{eff}} = a_1 \boldsymbol{s}(t) + a_2 \dot{\boldsymbol{s}}(t), \tag{2.20}$$

where $\dot{\boldsymbol{s}}(t)$ contains information about the past of $\boldsymbol{s}(t)$, and the a_i are coefficients. We include $\Delta \boldsymbol{B}_{\text{eff}}$ into Eq. (2.17) and get

$$\frac{\text{d}}{\text{d}t} \boldsymbol{s} = \frac{g_e \mu_{\text{B}}}{\hbar} \left(\boldsymbol{s} \times \boldsymbol{B}_{\text{eff}} + a_2 \boldsymbol{s} \times \dot{\boldsymbol{s}} \right). \tag{2.21}$$

As seen above, the first term describes the precessional motion of the spin and is known as field-like torque, while the second term is the damping of the motion and, therefore, called damping-like torque [248].

2.4.2 Landau-Lifshitz-Gilbert equation

In the section above, we discussed the dynamics of a single spin. Here, we focus on a many-spin system and macroscopic quantities. Thus, we use the normalized average magnetization $m = \sum_{i=1}^{N} \boldsymbol{\mu}_i / N \mu_{\text{s}}$ with the local magnetic moment $\boldsymbol{\mu}_i$ and the electron spin magnetic moment μ_{s} [248] to describe the dynamics of so-called macro-spins [12].

For a magnetic material at temperatures below their critical temperature ($T \ll T_{\text{C}}$), it can be shown [90] that the equation describing the dynamics of $\boldsymbol{m}$ are structurally very same to the damped single-spin equation [Eq. (2.21)]. The result is the famous Landau-Lifshitz-Gilbert (LLG) equation:

$$\frac{\partial \boldsymbol{m}}{\partial t} = -\gamma_{\text{G}} \boldsymbol{m} \times \boldsymbol{B}_{\text{eff}} + \alpha |\gamma_{\text{G}}| \boldsymbol{m} \times \frac{\partial \boldsymbol{m}}{\partial t}, \tag{2.22}$$

Figure 2.7 | Magnetization dynamics. A torque $\propto \boldsymbol{B}_{\text{eff}} \times \boldsymbol{m}$ excites the magnetization $\boldsymbol{m}$ out of its equilibrium position parallel to $\boldsymbol{B}_{\text{eff}}$ and starts precessing around the effective magnetic field $\boldsymbol{B}_{\text{eff}}$ back to equilibrium due to a finite damping $\propto \boldsymbol{m} \times \dot{\boldsymbol{m}}$.
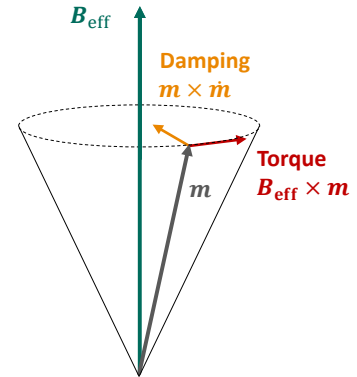
with $\gamma_{\text{G}} = \gamma/(1 + \alpha^2)$, where γ denotes the gyromagnetic ratio and α is called Gilbert damping. We note that the LLG equation [Eq. (2.22)] includes that the average magnetization is not decreasing by its dynamics [182]. Fig. 2.7 qualitatively depicts the situation of the precessing and damped magnetization. The damping can be interpreted as the loss of spin angular momentum to the other baths shown in Fig. 2.1, which is a complex problem for real magnetic systems [12].

2.4.3 Magnons

As seen in the previous section, Eq. (2.22) already includes a term, in which torque can be exerted on a spin ($\propto \boldsymbol{B}_{\text{eff}} \times \boldsymbol{m}$) and may lead to the generation of a quantized spin wave, a magnon. To get an intuitive picture what magnons are, we consider a ferromagnetic spin structure at $T = 0\,\text{K}$, where all spins favor to align parallel to each other to minimize the Heisenberg exchange interaction with their nearest neighbors and, thus, the total energy of the system [146]. If we exert torque on a single spin, it starts to precess around its equilibrium position [see Eq. (2.22)]. Due to, e.g., exchange interaction H_{ex}, the neighboring spins also start to precess and, thus, initiate a wave-like propagation of spin angular momentum through space [146] [Fig. 2.8].

Let us derive the properties of magnons in a more mathematical manner. Therefore, we assume a perfect ferromagnetic system in the following and start with the harmonic approximation of the spin Hamiltonian. Note that for complex magnetic systems such as ferri- or antiferromagnets the situation complicates. The exchange Hamiltonian for
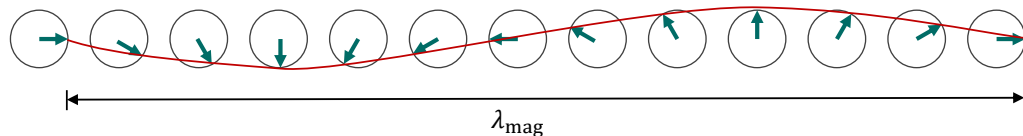

Figure 2.8. | Schematic of a spin wave. Top view of a magnon with wavelength λ_{mag}. The green arrows show the projection of precessing spins due to the exchange interaction between neighboring spins. The resulting collective wave-like motion is depicted by the red curve. Figure redrawn from Ref. [146].

neighboring spins at sites j and $j \pm 1$ is given by

$$\hat{H}_{\mathrm{ex}} = -\frac{J_{\mathrm{ex}}}{\hbar^2} \hat{\boldsymbol{s}}_j \cdot (\hat{\boldsymbol{s}}_{j-1} + \hat{\boldsymbol{s}}_{j+1}). \tag{2.23}$$

For simplicity, we consider interactions with the next-nearest neighbors as negligible and define an effective exchange field as $\hat{\boldsymbol{B}}_j^{\mathrm{ex}} = -J_{\mathrm{ex}} \cdot (\hat{\boldsymbol{s}}_{j-1} + \hat{\boldsymbol{s}}_{j+1})/\hbar^2$ that simplifies the Hamiltonian to $\hat{H}_{\mathrm{ex}} = \hat{\boldsymbol{s}} \cdot \hat{\boldsymbol{B}}_j^{\mathrm{ex}}$. Since magnons are a dynamical phenomenon, we get the spin dynamics again from an Ehrenfest equation of motion [146, 248]

$$\frac{\mathrm{d}\langle \hat{\boldsymbol{s}}_j \rangle}{\mathrm{d}t} = \frac{\mathrm{i}}{\hbar} \langle \left[\hat{H}_{\mathrm{ex}}, \hat{\boldsymbol{s}}_j \right] \rangle = \frac{g_e \mu_{\mathrm{B}}}{\hbar} \langle \hat{\boldsymbol{s}}_j \times \hat{\boldsymbol{B}}_j^{\mathrm{ex}} \rangle. \tag{2.24}$$

The solution describes a precession of the spin j around the effective exchange field $\hat{\boldsymbol{B}}_j^{\mathrm{ex}}$. Further, we can linearize the equation of motion [Eq. (2.24)] under the assumptions that the perturbation is small $(s_j^x, s_j^y \ll s_j)$, the z-component of $s^x = s_j$ as well as s^x and s^y can be neglected for $\mathrm{d}s^z/\mathrm{d}t$. Then, the linearized equations can be written as [146]

$$\frac{\mathrm{d}}{\mathrm{d}t} s_j^x = -\frac{J_{\mathrm{ex}} g_e \mu_{\mathrm{B}}}{\hbar} \left(2s_j^y - s_{j-1}^y - s_{j+1}^y \right) \tag{2.25}$$

$$\frac{\mathrm{d}}{\mathrm{d}t} s_j^y = -\frac{J_{\mathrm{ex}} g_e \mu_{\mathrm{B}}}{\hbar} \left(2s_j^x - s_{j-1}^x - s_{j+1}^x \right) \tag{2.26}$$

$$\frac{\mathrm{d}}{\mathrm{d}t} s_j^z = 0 \tag{2.27}$$

Of interest is usually the propagation of such quantized spin waves, so that a solution in the form of $s_j \propto \exp[i(jka - \omega t)]$ is wanted with a denoting the lattice constant, k the length of the wave vector and ω as the angular frequency of the magnon. Under the approximation for long wavelengths, on can obtain a solution [146]

$$\omega = -2J_{\mathrm{ex}} g_e \mu_{\mathrm{B}} [1 - \cos(ka)] \overset{ka \ll 1}{\approx} -J_{\mathrm{ex}} g_e \mu_{\mathrm{B}} a^2 k^2. \tag{2.28}$$

In summary, the frequency ω of a magnon is proportional to k^2 for long wavelengths. Finally, if we consider again the lowest possible excitation of a ferromagnet, the flip of a single spin, then the quantized energy of the resulting magnon is given by $\varepsilon_{\mathrm{mag}} = (n_{\mathrm{mag}} + 1/2)\hbar\omega$ [146]. Here, n_{mag} denotes the occupation number of the magnon with energy $\varepsilon_{\mathrm{mag}}$.

2.4.4 Spin current and torques

To close the section on spin dynamics, we turn from precessional motion of spins to the transport of spin angular momentum through space by spin currents. Hereby, we distinguish between two types: spin-polarized charge currents (see section 2.3.2) and pure spin currents. The latter describes a current, in which spin up and down are flowing in opposite direction and, thereby, cancelling the transport of a charge current [248].

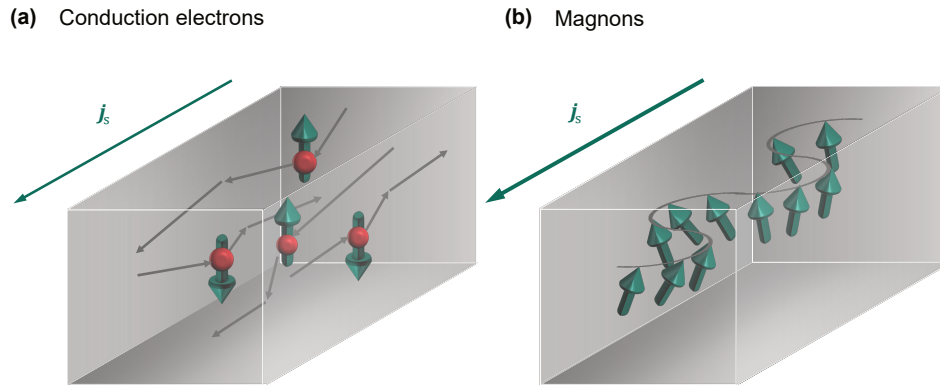More importantly, we have to differentiate the transport type of spin angular momentum.

Figure 2.9. | Spin transport types. Schematics of spin-angular-momentum-transport types, which can either be carried by **(a)** conduction electrons or **(b)** spin waves (magnons). The arrows depict the propagation direction of the respective spin currents. Figure redrawn from Ref. [248] with permission of T. S. Seifert.

It can either be mediated by conduction electrons [Fig. 2.9(a)] or torque-mediated, also known as magnonic transport [Fig. 2.9(b)]. It can be shown in the non-relativistic limit [8, 233] that a continuity-type equation for spin current densities read [266]

$$\frac{\partial \boldsymbol{M}}{\partial t} = -\boldsymbol{\nabla} \cdot \underline{\boldsymbol{j}}_{\mathrm{s}} + \boldsymbol{j}_{\omega}, \tag{2.29}$$

where $\underline{\boldsymbol{j}}_{\mathrm{s}} = \boldsymbol{v} \otimes \boldsymbol{M}$ is the linear current density and $\boldsymbol{j}_{\omega} = \boldsymbol{\omega} \times \boldsymbol{M}$ describes the angular current density with $\boldsymbol{\omega}$ denoting the angular velocity. Thus, we can identify $\boldsymbol{j}_{\omega}$ as torque-mediated and $\underline{\boldsymbol{j}}_{\mathrm{s}}$ as conduction-electron-mediated spin current.

2.5 Spin transport effects

As outlined in the introduction (see Chapter 1) the development of spintronic devices rests on three elementary operations, which are required to work efficiently to complement existing charge-based concepts [259]. This section discusses the transport of spin angular and spintronic effects for the generation and detection of spin currents in detail.

Importantly, spin-orbit interaction has two main consequences of interest for this thesis: (i) it allows torques to act on spins, which will start precessing around the total local effective magnetic field. And (ii), spin-orbit interaction has an impact on the orbital motion of electrons and may cause the transport of spin angular momentum and thus induce a spin current. To account for these consequences in a simple classical model, we need to consider spin-dependent forces that modify Newton's second law of motion which then simply reads

$$m\ddot{\boldsymbol{r}} = F(\boldsymbol{r}, t, \boldsymbol{s}). \tag{2.30}$$

One can derive the force of the spin-orbit interaction in a classical framework which turns

out to be a Lorentz-like force [54]

$$\boldsymbol{F} \propto \frac{e}{c}\boldsymbol{v} \times \boldsymbol{B}_{\mathrm{eff}} \propto \frac{e}{c}\boldsymbol{v} \times \boldsymbol{\nabla} \times (\boldsymbol{s} \times \boldsymbol{E}), \tag{2.31}$$

where the spin-orbit field $\boldsymbol{B}_{\mathrm{eff}}$ is proportional to $\boldsymbol{\nabla} \times (\boldsymbol{s} \times \boldsymbol{E})$, which can cause spin deflection phenomena such as the family of (spin) Hall effects. In section 2.2.2, we discussed the coupling of a spin to the effective magnetic field of spin-orbit coupling. It can also lead to a torque phenomenon known as spin-orbit torque and reads [173]

$$\boldsymbol{j}_{\omega} \propto \boldsymbol{s} \times \boldsymbol{B}_{\mathrm{eff}} \propto \boldsymbol{s} \times \left(\boldsymbol{E} \times \frac{\boldsymbol{v}}{c} \right). \tag{2.32}$$

In the following, we differentiate between external-field-driven and thermal effects for the generation and detection mechanisms of spin currents.

2.5.1 Electric- and magnetic-field-driven effects

This class combines four major mechanisms, which are introduced briefly below: electric fields in magnetic materials, spin pumping, magneto-resistive effects and spin-dependent Hall effects. Since the spin Hall effect is of central importance for this thesis, it will be discussed in more detail.

Electric fields in magnetic materials

First, electric fields can drive longitudinal spin-polarized currents inside a magnetic material since the conductivity of spin up and spin down is different. Considering a simple two-current model, the resulting spin current contribution from both spin species would read

$$\boldsymbol{j}_{\uparrow} - \boldsymbol{j}_{\downarrow} = (\sigma_{\uparrow} - \sigma_{\downarrow})\boldsymbol{E}. \tag{2.33}$$

Spin pumping

Second, the spin pumping technique is widely used in contemporary spintronics research. Here, the magnetic field component $\boldsymbol{B}_{\mathrm{rf}}$ of electromagnetic radiation couples to a magnetic material F via Zeeman interaction. Usually, this is done at radiofrequencies to excite ferromagnetic materials at their resonance frequency. Consequently, the spins start precessing and interacting with spins in an attached non-magnetic material N via exchange interaction at the F/N interface. Macroscopically, the magnetization dynamics can be described by [270, 304]

$$\frac{\partial \boldsymbol{M}}{\partial t} = \boldsymbol{M} \times \boldsymbol{B}_{\mathrm{rf}} + \alpha \boldsymbol{M} \times \dot{\boldsymbol{M}} + \boldsymbol{M} \times J_{\mathrm{ex}}\boldsymbol{m}_{\mathrm{N}}, \tag{2.34}$$

where α is the Gilbert damping and $\boldsymbol{m}_{\mathrm{N}}$ denotes the induced magnetization in N. Finally, this induces transfer of spin angular momentum to and polarization of spins in N [270, 304] resulting in a gradient of spin-polarization in the N layer that, then, drives a spin current

$\boldsymbol{j}_\text{s}$ [270].

Magneto-resistive effects

Third, in magnetic materials, once the electrical conductivity is dependent on the magnetization, one talks of magneto-resistive effects [268]. This class of field-driven effects includes giant [15, 80, 209], tunneling [133], anomalous [193] or spin Hall magneto-resistive effects [191], where the first two ones already have a huge impact on modern electronics since hard-disk drives employ them for their read/write heads.

Spin-dependent Hall effects

Fourth, the family of spin-dependent Hall effects, including the spin Hall and its inverse or the anomalous Hall effect, are field-driven and one of the most notable classical spintronic phenomena [259]. As shown in the last decade the spin Hall effect can also be used to provide ultrafast charge currents giving rise to the emission of THz-pulses [138, 246, 280].

The spin Hall effect (SHE) belongs to the family of spin-dependent Hall effects in which, similar to the ordinary Hall effect, charge carriers are deflected and transforming the initial charge current j_c into a transverse charge current j_c^OH. In contrast to the ordinary Hall effect where the deflection is caused by a Lorentz force due an external magnetic field [Fig. 2.10(a)], the SHE works without external magnetic fields in non-magnetic materials [259]. Here, the spin-dependent deflection is caused by the effective magnetic field arising from the spin-orbit interaction of the material [Fig. 2.10(b)]. Due to the spin-selective deflection, the resulting transverse current j_s is spin-polarized. For completeness, in magnetic material
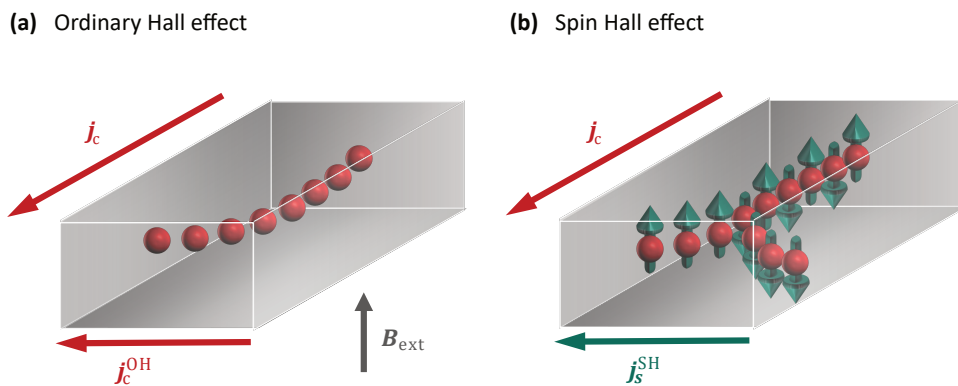

(a) Ordinary Hall effect **(b)** Spin Hall effect

Figure 2.10. | Hall effects. (a) In the ordinary Hall effect, a longitudinal charge current j_c flows inside a solid, to which an external magnetic field $\boldsymbol{B}_\text{ext}$ is applied. In the presence of $\boldsymbol{B}_\text{ext}$ electrons get deflected due to the Lorentz force and accumulate on one side perpendicular to the propagation direction of j_c. This causes a transverse charge current j_c^OH. **(b)** Due to spin-orbit interaction, the effective magnetic field $\boldsymbol{B}_\text{eff}$ generates a Lorentz-like force, deflecting electrons depending on their spin species, even without external magnetic field in a non-magnetic material. Analogue to panel (a), this so-called spin Hall effect transform j_c into a transverse spin current j_s^SH. Figure redrawn from Ref. [248] with permission of T. S. Seifert.

the spin-dependent Hall effect is known as anomalous Hall effect [259].

In spintronics, the SHE is as a field-driven interconversion effect since it is able to convert charge into spin currents or vice versa, wherein it is called inverse SHE (ISHE). For all spin-dependent Hall effects, one has to consider that the electron spin, in contrast to electron charge, is not conserved [248, 259].

To describe the mechanisms of the SHE, AHE and ISHE, the electron momentum scattering time τ is used in contemporary theoretical modeling since the deflection can be caused by disorder of a solid. The relation between the driving field $\boldsymbol{E}$ and the resulting spin current j_s is given by an Ohm's law-type equation

$$j_{\mathrm{s},ij} = \sum_k \sigma^{\mathrm{SH}}_{ijk} E_k, \tag{2.35}$$

where $\sigma^{\mathrm{SH}}_{ijk}$ is the spin Hall conductivity, which is a measure of the conversion efficiency of the spin-to-charge current conversion (S2C). Importantly, the spin Hall conductivity has three main contributions:

$$\underline{\sigma}^{\mathrm{SH}} = \underline{\sigma}^{\mathrm{int}} + \underline{\sigma}^{\mathrm{SS}} + \underline{\sigma}^{\mathrm{SJ}}. \tag{2.36}$$

Generally, one can classify these three mechanisms into, first, an τ-independent intrinsic deflection $\underline{\sigma}^{\mathrm{int}}$ [Fig. 2.11(a)], which is also disorder independent. The second contribution $\underline{\sigma}^{\mathrm{SS}}$ is linear in τ and is called skew scattering [Fig. 2.11(b)] and, third, the side jump contribution $\underline{\sigma}^{\mathrm{SJ}}$ that is disorder-induced but independent of τ [Fig. 2.11(c)]. Note that the sketches in Fig. 2.11 are not reflecting the τ-dependence as it is used in modern theories [248, 259].

Intrinsic mechanisms

The intrinsic deflection mechanism requires no scattering events, instead it originates from a perfect crystal structure [259]. Phenomenologically, it may happen that electrons, propagating through a solid, can be influenced by internal spin-orbit forces, which lead to
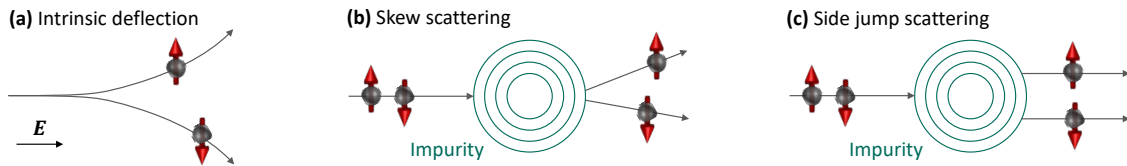

(a) Intrinsic deflection   **(b)** Skew scattering   **(c)** Side jump scattering

E Impurity   Impurity

Figure 2.11. | Spin Hall mechanisms. The underlying mechanisms of the spin Hall effect are classified into one intrinsic and two extrinsic contributions. **(a)** The intrinsic deflection assumes a perfect crystal lattice, which creates a spin-dependent drift velocity perpendicular to the driving electric field $\boldsymbol{E}$. **(b)** Skew scattering is an extrinsic deflection mechanism where electrons are spin-dependent inelastically scattered off an impurity. Spin-orbit interaction can be either included in the impurity potential analog to Mott scattering or be excluded. The latter causes the deflection by scattering of moving charge carriers in a spin-orbit coupled band structure off an impurity [248]. **(c)** The second extrinsic mechanism is side jump scattering where electrons also scatter off an impurity but in contrast to skew scattering, it is elastic conserving the electron momentum. Consequently, electrons get displaced depending on their spin orientation. Figure redrawn from Ref. [190].

transverse components of the electron velocity and, thus resulting in a deflection [142].

On a more quantitative level, we consider a Bloch electron in a crystal lattice (see section 2.1) and derive its time evolution from the Ehrenfest theorem. It can be shown that the electron velocity $\boldsymbol{v}_\mathrm{e}$ can be defined as [205]

$$\boldsymbol{v}_\mathrm{e} := \boldsymbol{\nabla}_{\hbar k}\varepsilon_{n,k} + \left(\frac{\mathrm{i}}{\hbar}\boldsymbol{E} \times \boldsymbol{\Omega}\right)(\boldsymbol{k}), \tag{2.37}$$

where k is the wave vector of the wave packet, $\boldsymbol{\nabla}_{\hbar k}\varepsilon_{n,k}$ denotes the ordinary band velocity and $\boldsymbol{\Omega}(\boldsymbol{k})$ is known as Berry curvature. The latter is a gauge-field tensor and describes a geometrical property of an energy band [296, 303]. The second term is the emergent anomalous velocity which is perpendicular to the ordinary velocity and the driving electric field $\boldsymbol{E}$. In analogy to classical Lorentz-like forces, the Berry curvature can be seen as a magnetic field in $\boldsymbol{k}$-space [205].

To calculate the intrinsic contribution to the spin Hall conductivity σ_{xy}, one can use the Kubo formula, which is an *ab-initio* method in the linear response theory [148]. Thus, σ_{xy}^int can be shown to read

$$\sigma_{xy}^\mathrm{int} = \frac{e^2}{\hbar}\int\frac{\mathrm{d}^3k}{(2\pi)^3}\mathrm{Im}\sum_{n\neq m}(f_n - f_m)\frac{v_{nm,x}(\boldsymbol{k})\,v_{nm,y}(\boldsymbol{k})}{(\omega_n - \omega_m)^2}. \tag{2.38}$$

Here, f are the Fermi functions of the electronic energy bands m and n, ω_n are the eigen frequencies of the velocity operator and the elements i of the velocity matrix are denoted as $v_{mn,i}$.

Remarkably, equation (2.38) indicates that the intrinsic deflection originates from all occupied states while the diagonal components of the conductivity tensor depend on the occupied states close to the Fermi energy. Finally, in systems with strong spin-orbit interaction, the Berry curvature is large and, thus, leads to a dominating intrinsic contribution to the spin Hall effect [259].

Skew scattering

As outlined above, the skew scattering mechanism is linear in τ, which results in a dominating contribution in the small disorder limit [259]. Qualitatively, it is an inelastic scattering process in which spin-polarized electrons get spin-dependently deflected while scattering off an impurity [Fig. 2.11(b)]. One can differentiate two fundamental eventualities: (i) an electron scatters off an impurity whose spin-orbit coupling is strong and (ii) it scatters of an impurity without any spin-orbit interaction. In the latter case, the electron is moving in a spin-orbit coupled band structure causing the spin-dependent change in momentum [259].

Side jump scattering

The third contribution to the spin Hall effect is side jump scattering and contains all contributions, which are not captured by intrinsic deflection or skew scattering. As schematically depicted in Fig. 2.11(c), it describes an elastic scattering off an impurity where the electron moves with the same momentum after scattering but being transversely displaced by

Δd depending on its spin specie [259]. Since the magnitude of Δd does not depend on the orientation of the spin, the total momentum for side jump scattering is conserved. Generally, side jump scattering is independent of τ but arises due to the presence of impurities. Therefore, it can be calculated from ideal electronic crystal structures in the limit of no disorder [291].

2.5.2 Thermal effects

In contrast to the field-driven effects above, also thermal phenomena play a major in nowadays spintronics research. Thermal effects arise from gradients of the distribution function of, e.g., the electrons or magnons. As the distribution function of electrons in equilibrium is a Fermi-Dirac function, the system is fully determined by the chemical potential μ and the temperature T. Therefore, we only need to consider gradients of μ and T for the description of thermal effects.

Thus, we distinguish between gradients of temperature driving magnon-mediated spin currents (ultrafast spin Seebeck effect, SSE) and heat-driven gradients of spin voltage driving conduction-electron-mediated spin currents (pyro-spintronic effect, PSE). Both mentioned effects are presented in more detail in the following sections as they complete the basis, along with the spin Hall effect, for the ultrafast laser-driven THz emission experiments of this thesis.

Temperature gradient: spin Seebeck effect

In analogy to the classical Seebeck effect in which a temperature gradient between to different materials drives a voltage, spin-dependent versions were discovered in the last decades [24]. While the spin-dependent Seebeck effect describes temperature-gradient-driven spin currents in metallic magnets, the spin Seebeck effect (SSE) is defined to cause a torque-mediated spin current in magnetic insulators [24].

Recently, it was found that on ultrafast time scales, the microscopic origin of the SSE appears to be different from what is known on typical spintronic clock rates at GHz frequencies [250]. In the following, we will focus this discussion to the in Ref. [250] predicted model of the ultrafast spin Seebeck effect. Here, a femtosecond pump pulse heats a bilayer thin-film stack which consists of a magnetic insulator F and a non-magnetic metallic N layer. Since F is transparent for the pump wavelength of $800\,\mathrm{nm}$ [250], the entire pulse energy gets absorbed in N. Consequently, the N electron temperature rises and induces spin fluctuations $s^{\mathrm{N}}(t)$ in N [Fig. 2.12(a)] and for electrons close to the interface, they generate an effective magnetic field that is proportional to $s^{\mathrm{N}}(t)J_{\mathrm{sd}}$, where J_{sd} denotes the exchange coefficient between F and N interfacial spins. Subsequently, an F spin senses this effective magnetic field as a force to torque out of its equilibrium position [Fig. 2.12(b)]. As the spins in F are coupled by exchange interaction, this initial torque generates a magnonic current (see section 2.4.3).

To explain the dynamics of the resulting spin current $j_{\mathrm{s}}(t)$, the model in Ref. [250] predicts that the spin-current density monitors the instantaneous state of the electronic system of
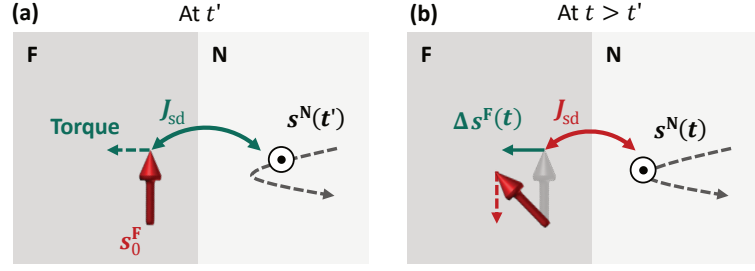
Figure 2.12. | **Microscopic ultrafast SSE model. (a)** Upon heating the heterostructure, the pump energy is absorbed only in the N layer causing a temperature difference between F and N. This increased generalized temperature of the electrons in N leads to spin fluctuations $s^N(t')$, which are sensed by spins in the F layer close to the interface by an effective magnetic field $s^N(t')J_{sd}$ with exchange constant J_{sd}. Consequently, a torque is applied on the F spins. **(b)** At times $t > t'$, the spin is out of its equilibrium position by $\Delta s^F(t)$. Due to the exchange interaction, a torque-mediated spin wave in F is induced. Figure redrawn from Ref. [250] with permission of T. S. Seifert.

N upon heating by [250]

$$\frac{\hbar}{2} j_s(t) = \mathcal{K} \Delta \tilde{T}_e^N(t), \tag{2.39}$$

with the pump-induced change $\Delta \tilde{T}_e^N(t)$ in the generalized electron temperature in N and the interfacial spin Seebeck coefficient $\mathcal{K}$. Initially after optical excitation, the number of pump-induced electrons above the Fermi level ϵ_F is small since it is proportional to $\Delta \tilde{T}_e^N(t)$. Importantly, the number of electrons gets increased by approximately two orders of magnitude due to carrier multiplication by electron-electron scattering [250]. Thus, the rise time of $j_s(t)$ shows the change from a nonthermal electron distribution to a Fermi-Dirac distribution on a time scale of $100\,\text{fs}$. Finally, the decay of $j_s(t)$ is dominated by electron-phonon energy transfer. Detailed information on the model of the ultrafast SSE and its derivation can be found in Ref. [250].

In summary, the ultrafast SSE is predicted to be (i) an interfacial effect and (ii) governed by the dynamics of the N electrons. Both predictions remain to be experimentally shown by variation of the F layer thickness and testing various insulating F materials while keeping the N layer same (see Chapter 4).

Spin-voltage gradient: pyro-spintronic effect

It was recently found that the spin-current dynamics in heterostructures of ferromagnetic metallic F and non-magnetic metallic N layers can be explained by the newly termed pyro-spintronic effect (PSE) [231]. Here, a bilayer structure gets excited by a pump pulse, which leads to an instantaneous increase of the electron temperature inside the F layer. This results then in a spin accumulation, also named spin voltage $\Delta\tilde{\mu}_s$, which quantifies the instantaneous excess of spin density in F. To adapt the magnetization in F to the higher electron temperature, spin angular momentum gets transferred in two channels: from the
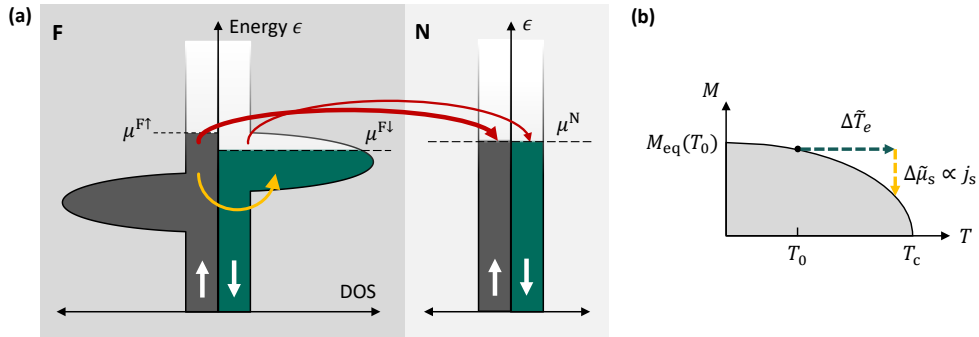
Figure 2.13. | Schematic of the pyro-spintronic effect. **(a)** Schematic of the density of states (DOS) for a bilayer sample of F and N. Upon heating the magnetic F layer, it shifts the chemical potentials $\mu^{\text{F}\uparrow}$ and $\mu^{\text{F}\downarrow}$ and demagnetizes by spin-flips from the majority into to minority band (yellow arrow). The shift of $\mu^{\text{F}\uparrow}$ and $\mu^{\text{F}\downarrow}$ causes a generalized spin voltage $\Delta\tilde{\mu}_{\text{s}}$. When attaching an N layer, the excess magnetization can also be transported as a spin current $j_{\text{s}}(t)$ from F to N (red arrows) which is proportional to $\Delta\tilde{\mu}_{\text{s}}$. **(b)** Magnetization M as a function of temperature T where upon heating the electronic temperature $\Delta\tilde{T}_{\text{e}}$ instantaneously rises from T_0 to T. To adapt to the actual magnetization, the system releases excess energy in form of $\Delta\tilde{\mu}_{\text{s}}$. Figure redrawn from Ref. [231] with permission of R. Rouzegar.

electrons to the crystal lattice of the ferromagnet and/or to the adjacent N layer as shown in Fig. 2.13(a). Thus, it was found that $\Delta\tilde{\mu}_{\text{s}}$ is proportional to the spin current density $j_{\text{s}}(t)$ [231].

Remarkably, the concept of a spin voltage is still valid for nonthermal electron distributions assuming Fermi-Dirac distributions. In this case, the spin voltage $\Delta\tilde{\mu}_{\text{s}}$ can be expressed as the difference of the chemical potentials of spin-up and spin-down electrons [231]. The decay of $\Delta\tilde{\mu}_{\text{s}}$ happens predominantly on a time scale τ_{es}, in which spin angular momentum is transferred from the electrons in F to the crystal lattice or the N layer. In addition, $j_{\text{s}}(t)$ is governed by the relaxation of the electron excess energy that is given by a generalized electron excess temperature $\Delta\tilde{T}_{\text{e}}$ [Fig. 2.13(a)-(b)].

Importantly, as the PSE is identified to be the driving force of ultrafast spin currents, it consequently follows that temperature gradients between F and N, as for the spin-dependent Seebeck effect, play only a minor role on ultrafast time scales [231]. More details and a thorough derivation of the PSE can be found in Ref. [231].

2.6 Light-matter interaction

Light-matter interaction is of major importance for this thesis because we study spintronic transport effects with optical pulses and, thus induce photocurrents, which are re-emitting THz pulses. Light is an electromagnetic wave and can be written as a superposition of plane harmonic waves

$$\boldsymbol{E}(\omega, \boldsymbol{k}) \propto \boldsymbol{E}(\omega) \exp(\mathrm{i}\boldsymbol{k} \cdot \boldsymbol{r}). \tag{2.40}$$

Each of which is characterized by its amplitude, its angular frequency ω and its wave

vector $\boldsymbol{k}$. Often the wavelength λ is used as a quantity for the description of waves and it is related to the wave vector by $\lambda = 2\pi/k$. Lastly, the energy of a wave is carried by a single photon which equals $\hbar\omega$. We note that this thesis deals with light waves carrying a large number of photons. Therefore, we discuss light-matter interaction phenomena in a classical framework [248]. In addition, we only assume plane waves with vanishing wavevector in the sample plane because the metal films under study are much thinner than the wavelengths of the optical and THz waves as well as the dimensions of the sample are much smaller than the laser spot diameter. Thus, we limit the further discussion to waves propagating along z.

Excitation of electrons

By excitation of electrons from states in the valence band to the conduction band, we create an empty Bloch state below ϵ_{F}, a so-called hole. A hole can be considered as a particle, which has the opposite charge mass, energy and crystal momentum of the corresponding Bloch electron, but the same band velocity [146, 248]. If we apply an external electric field with frequency ω, electrons can be excited through an optical transition to energetically higher states. To calculate the transition probability between the initial $|i\rangle$ and the finale state $|f\rangle$ within the framework of the linear response theory, we use Fermi's golden rule [146]

$$w_{if} = \frac{2\pi}{\hbar}|M_{if}|^2 \delta(\epsilon_i - \epsilon_f - \hbar\omega),$$ (2.41)

with the matrix elements of the electric-dipole operator M_{if}, which scales with the amplitude of the electric field. Energy conservation is guaranteed by the delta distribution [248].

2.6.1 Local light-matter interaction

On a macroscopic length scale, the interaction of electromagnetic radiation with matter can be described by the current, which get induced by the field $\boldsymbol{E}$. Importantly, the interaction is dominated by the electric field component of the light while the magnetic component is typically negligible as magnetic dipoles cannot keep up with the fast oscillations of the light [210, 248]. Therefore, one can define the induced current $\boldsymbol{j}_{\mathrm{ind}}$ by

$$\boldsymbol{j}_{\mathrm{ind}} = \underline{\sigma}(\omega)\boldsymbol{E}(\omega),$$ (2.42)

which is known as Ohm's law. The conductivity tensor $\underline{\sigma}$, which is a 3×3 matrix, can be classified in diagonal and off-diagonal components. While the diagonal entries of $\underline{\sigma}$ refer to current components longitudinal to the driving field, the off-diagonal elements are of central importance for spintronics as they cause Hall-like contributions with the current transverse to the field [259]. Furthermore, we note that the conductivity σ also includes the absorption of the incident light, which scales with $\mathrm{Re}(\sigma)$ and, thus, is proportional to $\mathrm{Im}(n^2)$ [66].

Drude model

The Drude model is the simplest conductivity model. Here, we treat electrons as independent particles in an isotropic medium. This assumption is often valid for conduction electrons in metals. The electrons are accelerated by the incident and induced light field $E(t)$ and collide with obstacles such as crystal imperfections, other electrons or phonons with a rate Γ. Thus, their velocity v gets randomized due to the collisions. It can be mathematically summarized in an equation of motion [11]

$$m_e \dot{v}(t) + m_e \Gamma v(t) = -eE(t), \tag{2.43}$$

with m_e denoting the electrons mass. For time-harmonic electric fields with frequency $\omega \neq 0$, we can solve the equation of motion and yield for the drift velocity v_{D} [11]

$$v_{\mathrm{D}}(\omega) = -\frac{e/m_e \Gamma}{1 - \mathrm{i}\omega/\Gamma} E(\omega). \tag{2.44}$$

This is a characteristic quantity for the diffusive motion of the electrons due to collisions. We obtain the famous Drude formula for nonzero frequencies by using $j = -en_e v_{\mathrm{D}}$ for the relationship between drift velocity and current with n_e denoting the electron density [11, 71, 72]

$$\sigma_{\mathrm{Drude}}(\omega) = \frac{\sigma_{\mathrm{DC}}}{1 - \mathrm{i}\omega/\Gamma}, \tag{2.45}$$

with $\sigma_{\mathrm{DC}} = \frac{e^2 n_e}{m_e \Gamma}$ for $\omega = 0$.

Nonlinear response

Despite from the linear response, we also consider nonlinear terms of the induced current [Eq. (2.42)] to be important for the comprehension of this thesis. However, the second (quadratic) and third (cubic) are sufficient. First, the quadratic response for two electric fields E_i reads [248]

$$j_i^{(2)}(\omega) = \sum_{j,k=1}^{3} \int \mathrm{d}\omega_1 \int \mathrm{d}\omega_2 \, \sigma_{ijk}^{(2)}(\omega, \omega_1, \omega_2) E_j(\omega_1) E_k(\omega_2) \tag{2.46}$$

and only gives a nonzero current if the medium has locally broken inversion symmetry. More importantly, the second-order current gives rise to frequency-mixed terms, e.g., difference $\omega_1 - \omega_2$ or $\omega_{1,2} - \omega_{1,2}$, which are crucial phenomena for THz radiation generation as difference frequency generation or optical rectification, respectively (see chapter 3.2.1) [36]. Second, terms of the form $\omega_1 \pm \omega_2$ are important for the linear electro-optic effect (see chapter 3.3) that is employed to detect THz electric fields with a pump-probe technique on ultrafast time scales [137]. Third, photocurrents typically scale linearly with the light power and thus the square of the light field [248]. Lastly, a third-order nonlinear term is important for the nonlinear Kerr effect which is used for passive mode-locking in femtosecond laser systems to generate ultrashort light pulses. It manifests in an induced change of

the refractive index Δn between the two main axes of the linearly-polarized field E and reads [36]

$$\Delta n(\omega) = n_2(\omega)c\varepsilon_0 E^2(\omega), \tag{2.47}$$

where c denotes the speed of light and n_2 is the response amplitude of the nonlinear part of the refractive index n [36].

2.6.2 Wave propagation

To describe the dynamics of the light field, we start with a wave propagating along z in the frequency domain as Maxwell equations dictate by [36]

$$\left(\partial_z^2 + \frac{\omega^2}{c^2}\right)\boldsymbol{E}(z,\omega) = -\frac{\mathrm{i}\omega}{c}Z_0\boldsymbol{j}(z,\omega). \tag{2.48}$$

Here, we can distinguish two different regimes for the current $\boldsymbol{j}$: (i) terms linear in $\boldsymbol{j}$ and (ii) nonlinear currents. First, for linear optics, we consider just the linear terms in $\boldsymbol{j}$ and simplify this discussion to homogeneous, isotropic, non-magnetic materials as well as linearly-polarized electric fields with induced currents parallel to the driving field polarization. The wave equation reads then [36]

$$\left(\partial_z^2 + \frac{\omega^2}{c^2}\right)\boldsymbol{E}(z,\omega) = 0 \tag{2.49}$$

and yields a plane wave of the form

$$E(z,t) = E_0 \exp[\mathrm{i}(k_z z - \omega t)] \tag{2.50}$$

as solution. E_0 denotes the amplitude of the wave while k_z is the z-component of the complex-valued wave vector $\boldsymbol{k}$, which is given by $\boldsymbol{k}^2 = \frac{\omega^2}{c^2}\varepsilon$ with $\varepsilon = 1 + \frac{\mathrm{i}cZ_0}{\omega}\sigma$. For isotropic magnetic materials, magneto-optic effects may alter the polarization of the incident wave as we see in the next section.

Magneto-optic Kerr effect

In modern magnetism research, the measurement of the local magnetization $\boldsymbol{M}$ state of a magnetized material is often realized by magneto-optic (MO) effects. Famous representatives of this class are the MO Faraday effect, present in transmission geometry and the MO Kerr effect (MOKE) for reflection geometries. For both, linear polarized light interacts with the magnetized material and changes the polarization state of the transmitted or reflected light for MO Faraday effect or MOKE, respectively [57].

In the case of MOKE, there are three different main geometries to distinguish: polar, longitudinal and transversal [Fig. 2.14]. They differ in the orientation of $\boldsymbol{M}$ with respect to the wave vector k_in of the incident light. Fig. 2.14 shows that the polar geometry is valid for out-of-plane magnetized materials [Fig. 2.14(a)] while for in-plane magnetized
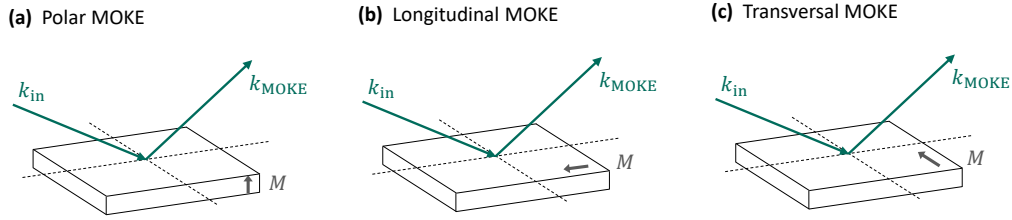
Figure 2.14. | Magneto-optical Kerr effect (MOKE). Linear polarized light with the wave vector $\boldsymbol{k}_{\text{in}}$ is reflected on a surface of a magnetic material. The reflected wave $\boldsymbol{k}_{\text{MOKE}}$ experiences a rotation of its polarization angle as well as an ellipticity, whose are proportional to the magnetization $\boldsymbol{M}$ of the material. One distinguishes between three main geometries depending on the orientation of $\boldsymbol{M}$. **(a)** Polar MOKE where $\boldsymbol{M}$ is parallel to the sample normal. **(b)** For the longitudinal MOKE geometry, $\boldsymbol{M}$ is parallel to $\boldsymbol{k}_{\text{in}}$ and **(c)** lastly, $\boldsymbol{M}$ perpendicular to $\boldsymbol{k}_{\text{in}}$ is called transversal MOKE.

materials the terms longitudinal ($\boldsymbol{M} \parallel \boldsymbol{k}_{\text{in}}$) and transversal ($\boldsymbol{M} \perp \boldsymbol{k}_{\text{in}}$) are used [Fig. 2.14(b)-(c)]. Importantly, for longitudinal and polar MOKE geometries, the polarization of the reflected light acquires an ellipticity η_{K} and rotates by an angle θ_{K}, whereas for transversal MOKE, a magnetization modulated intensity difference is measured [206].

Despite these three main configurations, there are several other terms for MOKE-based configurations used such as SMOKE or CMOKE [222, 295] but they all refer all to the same basic phenomenon. It can be shown that if $n \gg k$, the Kerr rotation θ_{K} and ellipticity η_{K} are given by [265]

$$\theta_{\text{K}} = -\frac{\varepsilon'_{xy}}{n(n^2 - 1)} \tag{2.51}$$

$$\eta_{\text{K}} = -\frac{\varepsilon''_{xy}}{n(n^2 - 1)}, \tag{2.52}$$

where n is the refractive index of the magnetized material and $\varepsilon_{ij} = \varepsilon'_{ij} + i\varepsilon''_{ij}$ are the complex-valued entries of the dielectric permeability tensor, which reads for cubic symmetry of a crystal [265]

$$\varepsilon(\boldsymbol{M}, \omega) = \begin{pmatrix} \varepsilon_{xx} & \varepsilon_{xy} & 0 \\ -\varepsilon_{xy} & \varepsilon_{xx} & 0 \\ 0 & 0 & \varepsilon_{zz} \end{pmatrix}. \tag{2.53}$$

Terahertz transmission through metallic thin-films

In this section, we show how we can describe the transmission of THz electric fields through metallic thin-films. Therefore, we consider a nonlinear induced current with the same restrictions as shown in section 2.6.2 and the resulting wave equation reads

$$\left(\partial_z^2 + \frac{\omega^2}{c^2}\right) \boldsymbol{E}(z, \omega) = -\frac{i\omega}{c} Z_0 \boldsymbol{j}^{\text{NL}}(z, \omega), \tag{2.54}$$
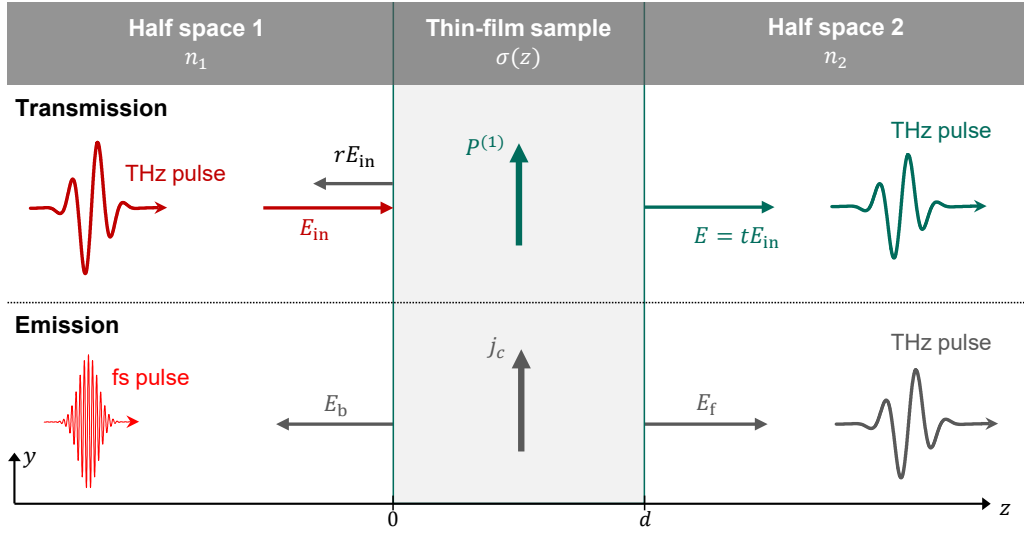
Figure 2.15. | Terahertz transmission and emission. Two schematic scenarios of THz spectroscopy in which a thin-film sample with conductivity $\sigma(z)$ between two infinite half spaces with refractive index n_i is involved. For an incident THz electric field E_{in} onto the thin-film (upper panel), it induces a linear polarization $P^{(1)}$, which causes the re-emission of a reflected rE_{in} and transmitted $E = tE_{\text{in}}$ electric field with the reflection and transmission coefficients r and t, respectively. The lower panel depicts a THz emission scheme. Here, a femtosecond laser pulse induces a transverse charge current density j_c that re-emits THz electric fields in the forward (E_f) and backward (E_b) direction along z. Figure redrawn from Ref. [248] with permission of T. S. Seifert.

where j^{NL} is defined as $j^{\text{NL}} = j - j^{(1)}$ and we abbreviate the wave equation in the following as a source term $S(z,\omega)$. It can be shown that by using a Green's function approach with $G_{z'}(z,\omega)$, we can solve Eq. (2.54) for E

$$E(z,\omega) = \int \mathrm{d}z' G_{z'}(z,\omega) S(z',\omega). \tag{2.55}$$

We can interpret the Green's function as a propagator of E for a delta-like source at position z' [248] while we observe the wave at position z. To calculate the propagation through a metallic thin-film with conductivity $\sigma(z)$, we assume two infinite half-spaces on the left-hand and right-hand side of the metal film [Fig. 2.15]. Half space 1 has a refractive index of n_1 and meets the sample at $z = 0$. The second interface to half-space 2 with n_2 is at position d which denotes the thickness of the sample [Fig. 2.15]. The transmitted Green's function is given by [137]

$$G_{z'}(z,\omega) = \frac{\exp(\mathrm{i}k_2|z - z'|)}{2\mathrm{i}k_2} \left[1 + r_{12}\exp(2\mathrm{i}k_2 z)\right]. \tag{2.56}$$

Since we are only interested in the transmitted electric field along z, we use the one-dimensional wave equation and include the thin-film sample by a wave-vector distribution $k_0^2(z,\omega)$ and $\Delta(k^2) = \mathrm{i}Z_0\sigma\omega/c$. Half-space 2 is usually air and, thus, we set $n_2 \approx 1$. Then, the wave equation yields [248]

$$[\partial_z^2 + \left(k_0^2(z,\omega) + \Delta(k^2)(z,\omega)\right)]E(z,\omega) = 0. \tag{2.57}$$

31

Using the Green's function approach introduced above, we rewrite the wave function with a source term $S(z, \omega) = -\Delta(k^2)(z, \omega)E(z, \omega)$, which then reads

$$[\partial_z^2 + k_0^2(z, \omega)]E(z, \omega) = S(z', \omega). \tag{2.58}$$

And solve the wave equation whose solution then yields

$$E(z, \omega) = t_{12}E_{\text{in}} + \int_0^d dz' G_{z'}(z, \omega)S(z', \omega). \tag{2.59}$$

We see that the solution contains two terms: first, the incident electric field E_{in} multiplied with the Fresnel transmission coefficient $t_{12} = 2n_1/(n_1 + n_2)$ [66] and second, an additional wave caused by the thin-film sample. Assuming the thin-film stack much thinner than (i) the wavelength and (ii) attenuation length of the incident wave, it can be shown that the Green's function from the reference system is given by $G_{z'}(z, \omega) \approx c/[i\omega(n_1 + n_2)]$ [248]. In addition, we consider the sample thin enough to have a constant electric field E over the entire thin-film thickness d. Finally, we get the following relation for the transmitted electric field

$$t(\omega) := \frac{E(\omega)}{E_{\text{in}}(\omega)} = \frac{2n_1}{n_1 + n_2 + Z_0 \int_0^d dz' \sigma(z', \omega)}, \tag{2.60}$$

where $Z_0 = 377\,\Omega$ denotes the vacuum impedance. This equation (2.60) is a generalized version of the famous Tinkham formula [93].

Terahertz emission of F|N heterostructures

In addition to the transmission of electric fields through a thin-film sample, we discuss the problem in which a charge current density $-ej_{\text{c}}$ is induced in the sample that re-emits an electric field [Fig. 2.15]. We restrict this problem to the forward propagating wave E_f as shown in Fig. 2.15 and include the charge current density into the wave equation in Eq. (2.54):

$$[\partial_z^2 + k^2(z, \omega)]E(z, \omega) = -eZ_0\omega j_{\text{c}}(z, \omega)/ic. \tag{2.61}$$

Analogue to the previously discussed transmission problem, we again use the Green's function approach with the source term [252]

$$S(z, \omega) = -\frac{eZ_0\omega j_{\text{c}}(z, \omega)}{ic} - \Delta(k^2)(z, \omega)E(z, \omega). \tag{2.62}$$

Assuming again the second half space [Fig. 2.15] exhibiting a refractive index of $n_2 \approx 1$, we can use $\Delta(k^2) = iZ_0\sigma\omega/c$ and assuming all involved wavelengths and their attenuation lengths larger than the thickness of the thin-film as well as again a constant electric field throughout the film, we get

$$E(z, \omega) = \frac{eZ_0 \int_0^d dz' j_{\text{c}}(z', \omega)}{n_1 + n_2 + Z_0 \int_0^d dz' \sigma(z', \omega)}, \tag{2.63}$$

with the total impedance of the film $\frac{1}{Z(z',\omega)} = \frac{n_1+n_2}{Z_0} + \int_0^d \mathrm{d}z'\sigma(z',\omega)$. A more thorough derivation can be found in Ref. [252].

Finally, we focus on further parameters of the THz emission process in F|N heterostructures. First, the induced charge current density j_c results from the generation of a spin current density j_s in F due to the PSE (see section 2.5.2) for metallic F or ultrafast SSE (see section 2.5.2) for insulating F. However, the spin current density j_s is proportional to the total absorbed pump light energy density A [246]. Depending on the material properties of F and N, the pump light may get absorbed differently by the two layers. Therefore, we use $j_\mathrm{s} \propto A/(d_\mathrm{F} + Bd_\mathrm{N})$, where d_i denote the thicknesses of the F and N layer, respectively and $B = \mathrm{Im}(n_\mathrm{N}^2)/\mathrm{Im}(n_\mathrm{F}^2)$ [194, 231]. In addition, the spatial dependence of $j_\mathrm{s}(z,\omega)$ inside the N layer is considered by [246]

$$j_\mathrm{s}(z) = \tanh\left(\frac{d_\mathrm{N}}{2\lambda_\mathrm{rel}}\right), \tag{2.64}$$

where λ_rel is the relaxation length of j_s. A detailed derivation can be found in Ref. [246]. Finally, we have to consider that the spin-to-charge current conversion from the initial j_s to j_c can be quantified by an efficiency θ and obtain ultimately [194, 231, 246]

$$E(\omega) \propto \frac{A}{d_\mathrm{F} + Bd_\mathrm{N}} Z(\omega)\theta j_\mathrm{s}^0(\omega)\lambda_\mathrm{rel} \tanh\left(\frac{d_\mathrm{N}}{2\lambda_\mathrm{rel}}\right), \tag{2.65}$$

where j_s^0 denotes the spin current density, which is injected into the N layer.

Experimental methods

THz emission spectroscopy is an excellent optical tool to study charge and spin transport dynamics. It allows to gain direct insight into the temporal evolution of ultrafast spin currents and spin-to-charge current conversion at highest frequencies. To complete the pool of possible techniques to characterize material parameters, THz transmission spectroscopy is suitable to obtain properties like the impedance in a broad frequency range. All THz electric fields are detected time-resolved by the linear electro-optic effect (EOS).

Due to the very similar subject matter of this thesis and the thesis by T. S. Seifert [248], this chapter has substantial overlap in terms of the structure and the scientific content.

3.1 Laser system

The key to time-resolved measurements of ultrafast processes are stimuli on the same timescale or faster. Laser systems provide the fastest stimuli available as light pulses with durations in the femtosecond regime ($1\,\text{fs} = 10^{-15}\,\text{s}$). Such pulsed lasers are commercially-available and based on a variety of laser active media (e.g. solid-state, fiber, dye) [78] but share the same basic lasing concept: an active medium is optically pumped until an inversion of the populated states of the active medium is reached and re-emits electromagnetic radiation of a single wavelength corresponding to the energy difference of the inversion populated state to the ground or next-lower preferred state. Subsequently, the emitted waves are coherently amplified in a simple cavity [78].

The described process produces an output with constant intensity over time, the so-called continious wavelength (cw) mode. For a pulsed operation different mechanisms are available. The laser system used in this thesis operates in the pulsed regime with self-locking of cavity modes by Kerr lensing inside the active medium [234]. To start this mode-locking process, it requires comparably high intensities in the Kerr medium. Usually intensity fluctuations, achieved by shortly detuning the cavity length, are employed to start the highly nonlinear process of mode-locking where the refractive index of the medium becomes intensity-dependent [234]

$$n(I) = n_0 + n_1(I). \tag{3.1}$$

The laser system used for all experiments in this thesis is a high-repetition rate solid-state Ti:sapphire oscillator *compact M1* from FEMTOLASERS (now: mks Spectra-Physics) with low signal-to-noise ratio exhibiting a pulse duration of 10 fs [38]. The Ti:Sa crystal
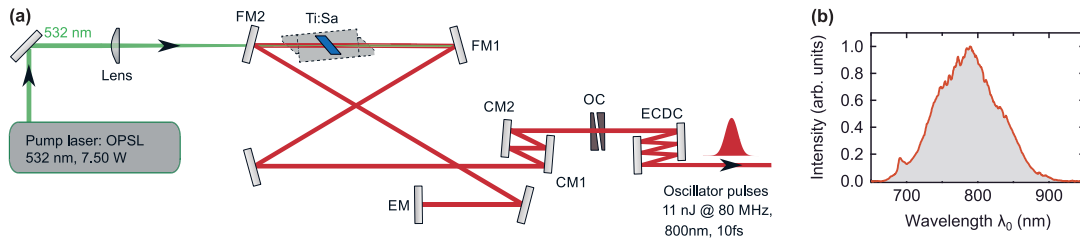
Figure 3.1. | MHz laser system. (a) A laser beam at a wavelength of 532 nm optically pumps a titanium-doped sapphire crystal (Ti:Sa) at its maximum absorption wavelength. The crystal serves as the active laser medium and is protected from thermal damages due to the high optical pump power by having a water-cooled base plate. The optical cavity of the emitted laser radiation at a center wavelength of 800 nm consists of the end mirror (EM) and a partially transmissive out-coupling mirror (OC). The focusing mirrors (FM1 and FM2) provide high intensities inside the active medium to lock the modes inside the cavity and generate ultrashort pulses. A pair of chirped mirrors (CM1 and CM2) compensate the occurring group velocity dispersion arising inside the cavity. The picture is a modified version from Ref. [38] with permission from L. Braun and S. F. Maehrlein. **(b)** Output spectrum of the *compact M1* Ti:Sa oscillator with a full-width at half maximum of about 115 nm.

(active medium) is pumped at its absorption maximum by an optically pumped semiconductor continuous wavelength laser at 532 nm (Coherent Verdi G8) with an output power of 7.5 W. A detailed scheme of the cavity is shown in Fig. 3.1(a). We achieve the following output parameters of the oscillator cavity: 80 MHz repetition rate, 11 nJ pulse energy and a central wavelength of 800 nm. An external cavity dispersion control (ECDC) unit consisting of a pair of chirped mirrors enables fine tuning of the pulse duration, e.g., the group velocity dispersion of transmissive optical elements of the setup is pre-compensated with additional bounces on the chirped mirrors of the ECDC. Fig. 3.1(b) shows a typical spectrum of the output beam with a full-width-at-half-maximum of 115 nm, indicating a pulse duration in the order of 10 fs. Behind the cavity output, the beam is splitted into two beams with a ratio of 80:20 to enable a time-resolved spectroscopic measurement scheme by having a pump (80%) and probe (20%) beam from the same laser system.

3.2 THz radiation generation

3.2.1 Optical rectification

One important effect of light-matter interaction for THz radiation generation is optical rectification. Here, light from a broadband visible or near-infrared laser pulse with frequencies ν_i induces a second-order nonlinear polarization with difference frequencies $\nu_{\text{THz}} = \nu_2 - \nu_1$ [see Fig. 3.2] which lie in the far and mid-infrared (THz window) [22, 230].

Two conditions need to be fulfilled for the rectification process. First, the optical medium needs to have a broken inversion symmetry with susceptibility $\chi^{(2)}$ which is a material specific tensor and, here, among other properties, describes the efficiency of the rectification process [36, 316]. Second, a phase matching is required, which describes the relation of the phase velocity of the THz pulse and the group velocity of the optical pulse that have to
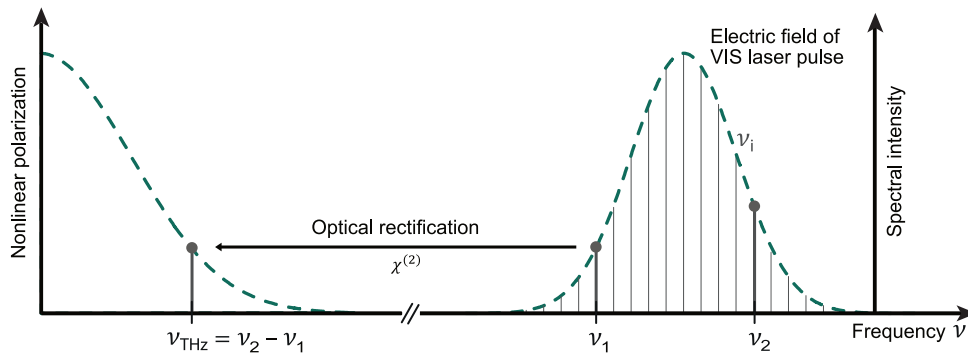
Figure 3.2. | Optical rectification. Frequencies ν_i of the electric field from a broadband visible laser pulse gets mixed in a nonlinear optical medium with susceptibility $\chi^{(2)}$, which also describes the conversion efficiency of the mixing process. The resulting nonlinear polarization exhibits frequencies $\nu_{\mathrm{THz}} = \nu_2 - \nu_1$, which lie in the mid- to far-infrared spectral range. The picture is reproduced from Ref. [168] with permission of S. F. Maehrlein.

be in phase with each other throughout the thickness of the nonlinear medium [316]. This results in a constructive sum of all ν_{THz} and, therefore, a broadband nonlinear polarization [see Fig. 3.2].

An advantage of optical rectification is that the emitted THz electric field exhibits a fixed carrier-envelope phase, so that coherent detection schemes become possible. One can categorize optical rectification into two different types: (i) non-resonant excitation like for crystalline emitters (ZnTe, GaP, GaSe) and (ii) resonant excitation as in photoconductive switches or spintronic terahertz emitters. The latter resonant process will be elaborated in more detail in the following section.

All these different types of THz emitters exhibit characteristic properties in terms of their emitted spectral width, polarization and handleability. Photoconductive switches usually emit rather narrowband THz electric fields from 1 to 3 THz while other emitters exhibit the potential for the efficient generation of much more broadband spectra, e.g., ZnTe 1-5 THz, GaP 1-8 THz and GaSe 10-40 THz [155] for relatively thick crystals. By changing their thickness, different phase-matching conditions can be achieved and, therefore, change the spectral weight to higher or lower frequencies [36]. Moreover, phonon resonances in the crystal-based emitter give rise to spectral gaps [39]. In photoconductive switches, which are biased semiconductors, the incident electric field excites charge carriers above the semiconductor band gap. The bias accelerates the charges and generates a charge current, which re-emits a THz electric field [41].

3.2.2 Heat-driven spintronic THz emission

A recently emerging class of THz sources are spintronic terahertz emitters (STEs) based on metallic heterostructures [249, 280]. The underlying mechanisms are twofold: (i) The incident femtosecond laser pulse heats the heterostructure, quenches the magnetization $\boldsymbol{M}$ of the magnetic layer F [see Fig. 3.3] and generates a spin voltage $\Delta\tilde{\mu}_{\mathrm{s}}$ which gives rise to a spin current density j_{s} [231]. As shown in Fig. 3.3 this spin-polarized current
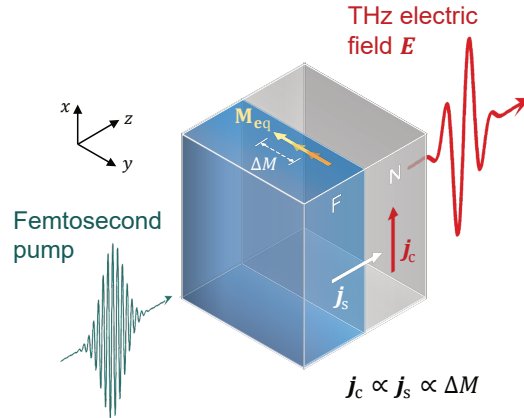
Figure 3.3. | Heat-driven THz generation. A femtosecond laser pulse is incident on a spintronic heterostructure consisting of a magnetic layer F and a non-magnetic layer N. The induced heat from the laser pulse quenches the magnetization $\boldsymbol{M}_{\mathrm{eq}}$ by ΔM and give rise to a transient spin voltage, which drives the spin current with density j_{s}. When propagating into the N layer, j_{s} experiences the spin-orbit coupling of the N material and gets deflected. Thereby, a transverse charge current j_{c} is generated that acts like an electric dipole emitting a THz electric field $\boldsymbol{E}$.

j_{s} propagates into the adjacent non-magnetic layer N, where (ii) j_{s} gets converted into a transverse charge current density j_{c} by a spin-to-charge current conversion process, e.g., the inverse spin Hall effect. Due to the pulsed excitation, also j_{c} is time-dependent and acts like a Hertzian dipole re-emitting an electric field with frequencies extending to the THz frequency range [138, 246]. Further details on the microscopic explanations of these mechanisms can be found in Chapter 2, sections 2.5.1 and 2.5.2.

Spintronic THz emitters feature many properties, which make them superior to the other classes of emitters. They are able to generate a broadband and gapless spectrum from 1 up to 40 THz. No phase matching or complicated crystal-cutting is needed. STEs are robust and in principle effort scalable in terms of the used materials [246]. As it will be shown in Chapter 7 the linearly-polarized emission from STEs can be controlled and modulated by an external magnetic field which make these emitters excellent candidates for modulation-based spectroscopic techniques [100]. In terms of the efficiency, STEs are already comparable with other tabletop THz sources and exhibit the potential to outperform even high-field sources like $\mathrm{LiNbO_3}$ in the near future [247].

3.3 THz electric field detection

Electro-optic sampling

To detect the THz electric fields from any kind of sample or THz source all studies within this thesis use electro-optic (EO) sampling. This detection method has a major advantage for THz time-domain spectroscopy: a simultaneous detection of amplitude and phase [139, 155]. Compared to other detection schemes there is no complicated phase retrieval
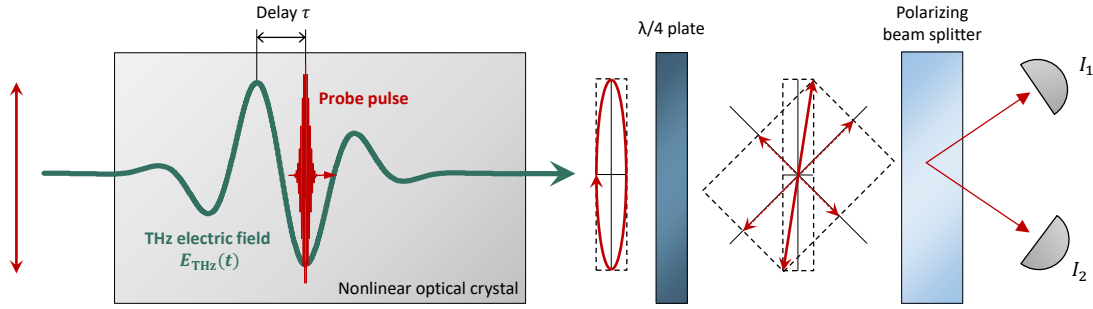
Figure 3.4. | Electro-optic sampling. The THz electric field $E_{\mathrm{THz}}(t)$ linearly changes the refractive index of a nonlinear medium which is probed by a linearly-polarized probe pulse. By delaying both pulses with respect to each other with time τ the THz electric field gets sampled by the probe pulse and encoded in its polarization state. The induced elliptical polarization behind the nonlinear crystal gets transformed to a polarization rotation by a quarter-wave plate and a polarizing beam splitter subsequently projects the linear polarization onto two orthogonal axis, which are then measured by a pair of photodiodes. The picture is a modified version taken from Ref. [98].

algorithms by, e.g., the Kramers-Kronig relations, required [36].

Linear electro-optic effect

The linear electro-optic effect, also known as Pockels effect, describes a process where an electric field E_{THz} changes transiently the refractive index by Δn inside an optical nonlinear medium, where Δn is linearly proportional to amplitude and phase of E_{THz} [Fig. 3.4]. Thus, the nonlinear medium becomes transiently birefringent. The co-propagating probe pulse experiences this transient birefringence and changes its polarization state from initially linear to elliptical. In summary, the transient amplitude and phase information of E_{THz} is transferred to the polarization state of the probe pulse at a given time t. By delaying the probe pulse with respect to the THz electric field by τ, the waveform of $E_{\mathrm{THz}}(\tau)$ can be sampled [Fig. 3.4]. Typical materials for EOS are ZnTe(110) and GaP(110) [139, 155].

Balanced detection

The final step in detecting E_{THz} is the read-out of the induced probe pulse ellipticity. Therefore, after acquiring an ellipticity from the nonlinear crystal the probe pulse propagates through a quarter-wave plate, which transforms it into a polarization rotation [Fig. 3.4]. A polarizing beam splitter projects the linear polariation onto two orthogonal axis, spatially separates them and finally, a pair of photodiodes measures the intensities of both beams. Since the acquired ellipticity is usually small (10^{-5}-10^{-8}), one needs a suitable method to supress the rather large background. Thus, by taking the difference of the induced photodiode currents, one gets access to the background-free component $S(\tau)$ proportional to the amplitude and phase of E_{det} incident in the electro-optic detection crystal

[315]

$$S(\tau) = \frac{I_1 - I_2}{I_1 + I_2} = \frac{2\pi d n_0^3 r_{\mathrm{eff}}}{\lambda_{\mathrm{pr}}} E_{\mathrm{det}}(\tau), \tag{3.2}$$

where d is the thickness of the detection crystal, n_0 its unperturbed refractive index and r_{eff} is the effective electro-optic constant. Further, λ_{pr} denotes the central wavelength of the probe pulse and τ the delay time between E_{THz} and the probe pulse. One need to note that the measured signal $S(\tau)$ does not equal E_{det} due to phase mismatched waves, dispersion and a finite probe bandwidth. Therefore, we introduce a transfer function H_{det}

$$S(t) = H_{\mathrm{det}} * E_{\mathrm{det}}. \tag{3.3}$$

A procedure on how to get access to the emitted THz electric field behind the THz source will be detailed in section 3.5.

3.4 THz spectrometer: emission and transmission

3.4.1 THz emission scheme

We use a double-modulated pump pulse to increase the overall signal-to-noise ratio. First, a mechanical chopper modulates the light intensity at $30\,\mathrm{kHz}$ to measure signals in the frequency domain far above the $1/f$ noise. Second, a harmonically back and forth shaking retroreflector with a maximal delay of $50\,\mathrm{ps}$ modulates of the pump-probe delay τ at $25\,\mathrm{Hz}$ (APE scanDelay 50). This second modulation allows for a fast scanning of an entire THz waveform. In total, both modulators in combination with an optimized detection layout pushes the setup to the shot-noise limit.

The principle optical layout of the THz spectrometer is depicted in Fig. 3.5. It enables two basic measurement modes with its two foci: (i) linear THz spectroscopy by generating THz radiation in the first focus and let the THz electric field transmit through a sample of interest in the second focus to determine, e.g., the impedance of the sample. Further details on this method are given in the following section 3.4.2. The second mode (ii) accessible with such THz spectrometers is THz emission spectroscopy, which is the main method used in this thesis. Here, the sample is placed in either the first or second focus and the optically excited sample generates a THz electric field (see section 3.2). In both modes, the electric field gets detected by electro-optic sampling in the third focus.

3.4.2 THz impedance

To quantify the electrical transport at THz frequencies we employ a referenced transmission method of THz pulses through the metallic thin-film of interest [Fig. 3.5]. To consider the influence of the mechanically supporting substrate of the thin-film, the transmission is measured through the bare substrate and the thin-film on top of the substrate. The spectral ratio $T(\omega)$ of these two transmitted fields $S_i(\omega)$ yields almost directly the frequency-
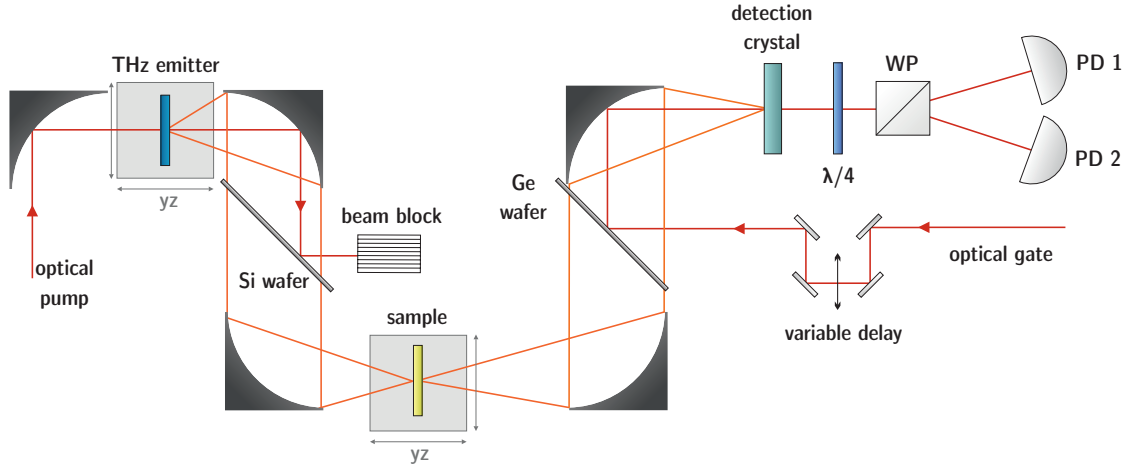
Figure 3.5. | Schematic of the THz setup. This THz spectrometer can be operated in two modes: (i) THz transmission and (ii) THz emission. In mode (i), the optical pump pulse is incident on a THz source generating a THz electric field, which gets focused onto the sample under study. A silicon wafer separates THz electric field and optical pump. In mode (ii), either the first or second focus is empty and just the sample of interest, emitting a THz electric field, is placed in one of the foci. In both modes, the THz pulse and the probe pulse get focused into a nonlinear crystal, where the probe pulse samples the THz electric field by the linear electro-optic effect. All information of the sampled THz pulse is encoded in the polarization state of the co-propagating probe pulse and is read out by a balanced detection consisting of a quarter-wave plate, a Wollaston prism and a pair of photodiodes. The picture is taken from Ref. [98].

dependent impedance $Z(\omega)$ of the entire stack (metal plus substrate) [99, 246].

$$T(\omega) = \frac{S_{\text{sample}}(\omega)}{S_{\text{substrate}}(\omega)} = 2n_1(\omega)\frac{Z(\omega)}{Z_0} = 2n_1(\omega)\frac{1}{n_1(\omega) + n_2(\omega) + Z_0 G(\omega)}. \tag{3.4}$$

As further indicated in equation (3.4) also the sheet conductance $G(\omega)$ of the metal film can be extracted. $n_1(\omega)$ and $n_2(\omega)$ denote the refractive index of the substrate material and air, respectively, while $Z_0 = 377\,\Omega$ is the vacuum impedance. More details on how to infer the frequency-dependent electrical conductivity from THz transmission measurements can be found in Chapter 2, sections 2.6.1 and 2.6.2.

3.5 Extraction of spin currents

As outlined in section 3.3 (EOS), the detected electric field does not equal the emitted field directly behind the THz source. The measured signal $S(t)$ equals the electric field $E_{\text{em}}(t)$ behind the sample surface convoluted with a setup-specific transfer function $H(t)$ [131]

$$S(t) = (H * E_{\text{em}})(t). \tag{3.5}$$

H contains the response of the electro-optic detector H_{det} as well as the propagation of the THz electric field from the sample to the detection crystal H_{prop}. To get E_{em}, we employ a two-step referencing method. First, we measure $H(t)$ by deconvoluting the

measured signal from a reference emitter (e.g. 50-µm-thick GaP(110)) based on optical rectification, whose emission is well understood [281] and, therefore, can be simulated with setup- and measurement specific parameters. Second, we deconvolute the measured signal with the previously found $H(t)$ up to a cut-off-frequency of $\omega_c/2\pi = 40\,\mathrm{THz}$ to get $E_{\mathrm{em}}(t)$. Frequencies $|\omega| > \omega_c$ are omitted because the small amplitudes of $S(\omega)$ and $H(\omega)$ may lead to significant uncertainties of the retrieved $E(\omega)$ [45].

This method relies on deconvolution of time-domain data, which is not straightforward. By transforming this inversion problem into a matrix-based problem, the deconvolution in the time domain gets possible. Another option is solving the inversion problem in the frequency domain by Fourier transforming all signals to $S(\omega)$. Here, the convolution becomes a multiplication $S(\omega) = H(\omega) \cdot E_{\mathrm{em}}(\omega)$ and with knowledge of the emitted field of the reference emitter $E_{\mathrm{em,ref}}(\omega)$ we obtain

$$E_{\mathrm{em}}(\omega) = E_{\mathrm{em,ref}}(\omega) \cdot \frac{S_{\mathrm{sample}}(\omega)}{S_{\mathrm{ref}}(\omega)}. \tag{3.6}$$

Finally, assuming transport of the spin current $j_{\mathrm{s}}(\omega)$ from F to N with conversion to a pure charge current $j_{\mathrm{c}}(\omega)$ via the ISHE, we can extract $j_{\mathrm{s}}(\omega)$ by a generalized Ohm's law [131, 246, 250]

$$E_{\mathrm{em}}(\omega) = eZ(\omega)\theta_{\mathrm{SH}}\lambda_{\mathrm{N}}j_{\mathrm{s}}(\omega). \tag{3.7}$$

Here, e is the elementary charge, θ_{SH} denotes the spin Hall angle and λ_{N} describes the spin propagation length in the non-magnetic layer N. In Eq. (3.7), the electron charge $-e$ shows up because j_{s} and j_{c} are given in units of half of Planck's constant $\hbar/2$ and of $-e$, respectively. The sample impedance can be calculated by using Eq. (2.63).

<div style="text-align: right; font-size: xx-large;">

4

</div>

Transition of laser-induced terahertz spin currents from torque- to conduction-electron-mediated transport

Spin transport is crucial for future spintronic devices operating at bandwidths up to the terahertz range. In F|N thin-film stacks made of a ferromagnetic/ferrimagnetic layer F and a normal-metal layer N, spin transport is mediated by (1) spin-polarized conduction electrons and/or (2) torque between electron spins. To identify a crossover from (1) to (2), we study laser-driven spin currents in F|Pt stacks where F consists of model materials with different degrees of electrical conductivity. For the magnetic insulators yttrium iron garnet, gadolinium iron garnet (GIG) and γ-Fe$_2$O$_3$, identical dynamics is observed. It arises from the terahertz interfacial spin Seebeck effect (SSE), is fully determined by the relaxation of the electrons in the metal layer, and provides a rough estimate of the spin-mixing conductance of the GIG/Pt and γ-Fe$_2$O$_3$/Pt interfaces. Remarkably, in the half-metallic ferrimagnet Fe$_3$O$_4$ (magnetite), our measurements reveal two spin-current components with opposite direction. The slower, positive component exhibits SSE dynamics and is assigned to torque-type magnon excitation of the A- and B-spin sublattices of Fe$_3$O$_4$. The faster, negative component arises from the pyrospintronic effect and can consistently be assigned to ultrafast demagnetization of minority-spin hopping electrons. In general, our results provide a route to the contact-free separation of torque- and conduction-electron-mediated spin currents.

Publication information

Author contributions

TK, PJC and OG conceived the experiments. OG and PJC performed the experiments and analyzed the data with support of RR, TSS and LN. PJC, IL, LM, CG, CW, XH, ZJ, HZ, SB, GJ and MK fabricated the samples. The manuscript was written by OG, PJC and TK with help and discussion contributions of all authors.

4.1 Motivation

A. Spin currents

Control over spin currents is a cornerstone of spintronic technologies [280]. Functionalities in such diverse fields as energy conversion and information technologies are envisaged to benefit from the generation, processing, and detection of spin currents [37, 258, 278, 297]. An important goal is to push the bandwidth of spintronic operations to the terahertz frequency range, corresponding to ultrafast time scales [280, 284].

A model system for the investigation of the transport of spin angular momentum is the F|N thin-film stack of Fig. 4.1(a), where spin can be transmitted from a ferromagnetic or ferrimagnetic layer F to an adjacent nonferromagnetic/nonferrimagnetic metal layer N. The spin current in F is mediated not only by (1) spin-polarized conduction electrons [195], which typically dominate spin transfer in metals, but also by (2) magnons, i.e., torque between coupled spins [5, 35], which is the main transport channel in insulators. Accordingly, spin transfer across an F/N interface can be mediated by (1) spin-polarized conduction electrons traversing the interface [see (1) in Fig. 4.1(a)] and by (2) spin torque between adjacent F and N regions [(2) in Fig. 4.1(a)]. As mechanism (2) results in the excitation of magnons in F [250], it can be considered as magnonic spin transfer.

In general, to drive an incoherent spin current of density j_s from F to N, a difference in temperature or spin chemical potential (also known as spin accumulation or spin voltage) between the two layers is required [24, 231]. For example, for a temperature gradient between F and N, the resulting spin current arises from the interfacial spin-dependent Seebeck effect (SDSE) [260] for channel (1) or the interfacial spin Seebeck effect (SSE) [3, 145, 226, 273, 274, 303] for channel (2).

In any case, the spin flow from F to N can be detected by conversion of the longitudinal j_s into a transverse charge current with density j_c [Fig. 4.1(a)] and measurement of the resulting voltage. For this purpose, N materials with sufficiently large inverse spin Hall effect (ISHE), for instance, Pt, are well suited.

B. THz spin transport

A powerful and ultrafast approach to deposit excess energy in F|N stacks is optical excitation by femtosecond laser pulses [Fig. 4.1(a)]. Measurement of the ultrafast transverse charge current j_c as a function of time t allows one to resolve elementary relaxation processes such as electron thermalization [250] and electron-spin and electron-phonon equilibration [231]. It also delivers insights into the role of temperature [175, 197], strain [163], defects [196], film thickness [79, 219], intermediate layers [159, 239, 252], and spin sublattices [82, 120] in spin transport and into details of spin-to-charge-current conversion [49, 99, 107, 165, 177, 287, 309, 311, 317].

For an insulating and pump-transparent F, temperature gradients between F and N (i.e., the SSE) were found to be the dominant driving force of the ultrafast j_s [143, 250]. For metallic F, in contrast, such temperature differences (i.e., the SDSE) were concluded to
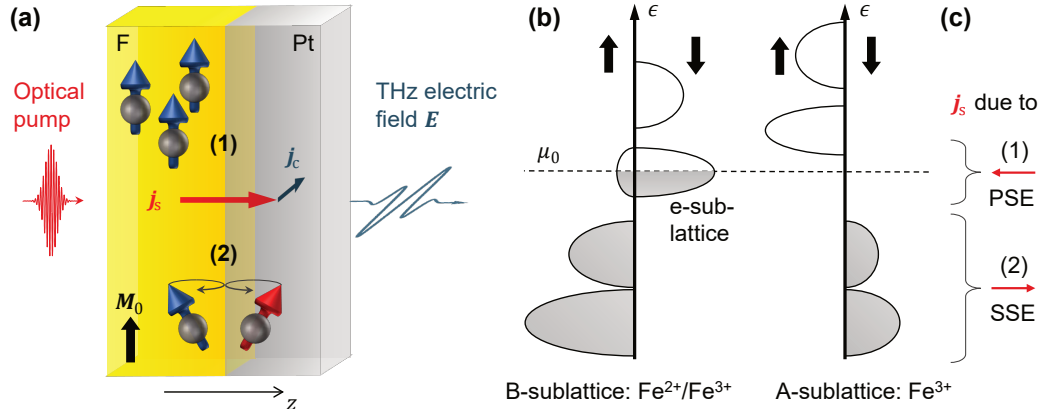
Figure 4.1. | (a) Schematic of photoinduced spin transport in an F|Pt stack, where Pt is platinum, and F is a magnetic layer with equilibrium magnetization $\boldsymbol{M}_0$. An ultrashort laser pulse excites the sample and induces an ultrafast spin current with density j_s from F to Pt along the z axis. In the Pt layer, j_s is converted into a transverse charge current with density j_c that gives rise to the emission of a terahertz electromagnetic pulse. Schematics (1) and (2) indicate spin transfer across the F/Pt interface that is mediated by (1) spin-polarized conduction electrons and (2) spin torque, the latter coupling to magnons in F. Both flavors (1) and (2) can be driven by gradients of temperature and spin accumulation. **(b)** Simplified schematic of the single-electron density of states vs electron energy ϵ of the tetrahedral A and octahedral B sites of the ferrimagnetic half-metal Fe_3O_4. The DC conductivity predominantly arises from the B-site minority-type hopping electrons of the e-sublattice. **(c)** In our interpretation, optical excitation of the Fe_3O_4|Pt stack triggers spin transfer through both the spin Seebeck effect (SSE) and pyrospintronic effect (PSE). While the SSE current is mediated by torque between Pt electrons and Fe_3O_4 electron spins far below the Fermi level μ_0 [(2) in panel (a)], the PSE transiently increases the chemical potential of the B-site minority-spin electrons around μ_0 and, thus, induces a conduction-electron spin current [(1) in panel (a)].

make a minor contribution. Instead, spin-voltage gradients were suggested and identified as the relevant driving force of spin transport on subpicosecond time scales in metals [27, 53, 85, 161, 185, 231]. More precisely, dynamic heating of F leads to a transient spin accumulation or spin voltage, which quantifies the excess of spin angular momentum in F. This phenomenon, which may be termed pyrospintronic effect (PSE), induces a spin current across the F/N interface [85, 231]. While the pump polarization has no impact on these incoherent effects, pump-polarization-sensitive spin transport was reported in several cases and ascribed to coherent torque [121, 218].

There are important open questions regarding the role of terahertz SSE and PSE. First, the SSE was so far only observed in F|Pt stacks with F made of yttrium iron garnet (YIG) [143, 250]. According to the microscopic model of Ref. [250], the spin-current dynamics should be fully determined by the relaxation dynamics of the Pt electrons, independent of the insulating F-layer material. This quite universal implication remains to be shown.

Second, with increasing electrical conductivity of the F material, a transition from ultrafast SSE to PSE should occur, which was not yet observed. At the crossover point, both spin transport channels (1) and (2) may be operative [Fig. 4.1(a)], and disentangling them

is crucial to maximize the overall generation efficiency of spin currents. The experimental separation of conduction-electron- and magnon-carried incoherent spin transport is challenging under quasistatic conditions [126, 235, 250]. However, on femtosecond time scales, SSE and PSE dominate and exhibit different temporal dynamics, as indicated by previous works [231, 250]. Thus, a separation of the two phenomena might be possible.

C. This chapter

In this chapter, we study ultrafast photogenerated spin currents in F|Pt bilayers as a function of various magnetic model F materials with different degrees of electric conductivity: the ferrimagnetic insulators maghemite (γ-Fe$_2$O$_3$), gadolinium iron garnet (Gd$_3$Fe$_5$O$_{12}$, GIG) and YIG (with a thickness ranging over three orders of magnitude), the ferrimagnetic half-metal magnetite (Fe$_3$O$_4$), and for referencing purposes, the ferromagnetic metal iron (Fe).

We reveal that the ultrafast dynamics of the SSE is independentof the choice of the magnetic insulator (YIG, GIG, or γ-Fe$_2$O$_3$), its thickness (3.4 nm to 3 µm) and growth method. Remarkably, in the half-metallic ferrimagnet Fe$_3$O$_4$, we observe simultaneous signatures of both SSE and PSE, whose ultrafast spin currents counteract each other. The PSE current is much smaller and of opposite sign than with Fe. We assign the PSE current in Fe$_3$O$_4$ to the minority hopping electrons [Fig. 4.1(b)].

4.2 Experimental details

A. THz emission setup

We use the laser system and THz emission setup presented in sections 3.1 and 3.4.1, respectively, for studying THz spin currents in F|N bilayers with varying F layer conductivity. The sample under study gets pumped by femtosecond laser pulses, which launch a spin current density j_s. By the ISHE [see section 2.5.1], j_s gets converted into a transverse charge current density j_c [Fig. 4.1(a)] that finally emits THz radiation [see section 3.2.2] [83, 99, 107, 138, 244, 246, 250, 301, 311, 317]. We detect the transient terahertz electric field by electro-optic sampling in a 1-mm-thick ZnTe(110) crystal, resulting in the electro-optic signal $S(t, \boldsymbol{M}_0)$ [139, 155, 300]. During the experiments, the in-plane equilibrium magnetization $\boldsymbol{M}_0$ of the sample is saturated by an external magnetic field (magnitude $\approx 100\,\mathrm{mT}$). We measure signals for two opposite orientations $\pm\boldsymbol{M}_0$. Because we are only interested in odd effects in the magnetization $\boldsymbol{M}_0$, we focus on the antisymmetric signal

$$S(t) = \frac{S(t, +\boldsymbol{M}_0) - S(t, -\boldsymbol{M}_0)}{2}, \tag{4.1}$$

All data are acquired at room temperature in air if not mentioned otherwise. To extract the spin current dynamics $j_s(t)$ from the measured signals $S(t)$, we use the referenced extraction method - in the time- and frequency-domain - presented in section 3.5.

B. Material choice

For the F material in our F|Pt stacks, we choose common and spintronically relevant two-lattice ferrimagnets with increasing degree of electric conductivity: (i) insulating YIG (thickness 3.4 nm to 3 μm), (ii) insulating GIG (58 nm), (iii) insulating γ-Fe_2O_3 (10 nm), and (iv) the half-metal Fe_3O_4 (10 nm) [57]. For referencing, (v) the ferromagnetic metal Fe (2.5 nm) is used. As the N material, we choose Pt for all samples due to its large spin Hall angle [259]. The approximate F-material conductivities [198, 253, 262, 267] are summarized in Fig. 4.2(a).

The insulating F materials transfer spin angular momentum by torque [Fig. 4.1(a), (2)], whereas for the metal Fe, the spin current is expected to be carried predominantly by conduction electrons [Fig. 4.1(a), (1)] [231].

In this respect, Fe_3O_4 is special because it exhibits both localized and mobile electrons with magnetically ordered spins. More precisely, the ferrimagnet Fe_3O_4 is a half-metal [see Fig. 2.2] since its conductivity is dominated by hopping-type transport of minority electrons. Fe_3O_4 possesses two sublattices A and B of, respectively, localized Fe^{2+}/Fe^{3+} and Fe^{3+} spins, which couple antiferromagnetically [57]. In the so-called magnetoelectric model, the spins of the hopping electrons are aligned predominantly antiparallel to $\boldsymbol{M}_0$ due to exchange interaction with A and B and, thus, form the so-called e-sublattice [28–30, 188].

A highly simplified schematic of the electronic structure of Fe_3O_4 is displayed by the spin- and site-resolved single-electron density of states in Fig. 4.1(b) [10, 154]. The majority (spin-up) electrons exhibit an electronic bandgap with a calculated magnitude of 1.7 eV [127], while the presence of minority (spin-down) hopping electrons at the Fermi level μ_0 [188] makes magnetite a half-metal. The measured spin polarization at μ_0 amounts to -72 % in Fe_3O_4(001), indicating a nonvanishing number of majority hopping electrons [Fig. 4.1(b)] [286].

C. Sample details and excitation

Details on the sample fabrication can be found in the Appendix of Ref. [131]. In brief, the YIG films are fabricated by three different techniques [pulsed laser deposition (PLD), sputtering, and liquid-phase epitaxy (LPE)]. The Fe|Pt reference sample is obtained by growing an Fe layer on top of half the F|Pt region for most of the samples. The terahertz emission signal from the resulting F|Pt|Fe regions is dominated by Pt|Fe and equals the reversed signal from an Fe|Pt layer [250]. By means of the Fe|Pt reference signals, the time axes of the terahertz signals from all samples can be synchronized with an accuracy better than 10 fs.

The pump electric field is approximately constant along z [Fig. 4.1(a)] throughout the thin-film stack of our samples. Therefore, the locally absorbed pump-pulse energy is only proportional to $Im(n^2)$, where n is the complex-valued refractive index of the material at the pump wavelength (800 nm). While the Pt and Fe layers are strongly absorbing [see section 2.6.1] [$Im(n^2) = 28$ and 30] [207], Fe_3O_4 is weakly absorbing (2.3) [243], and YIG,
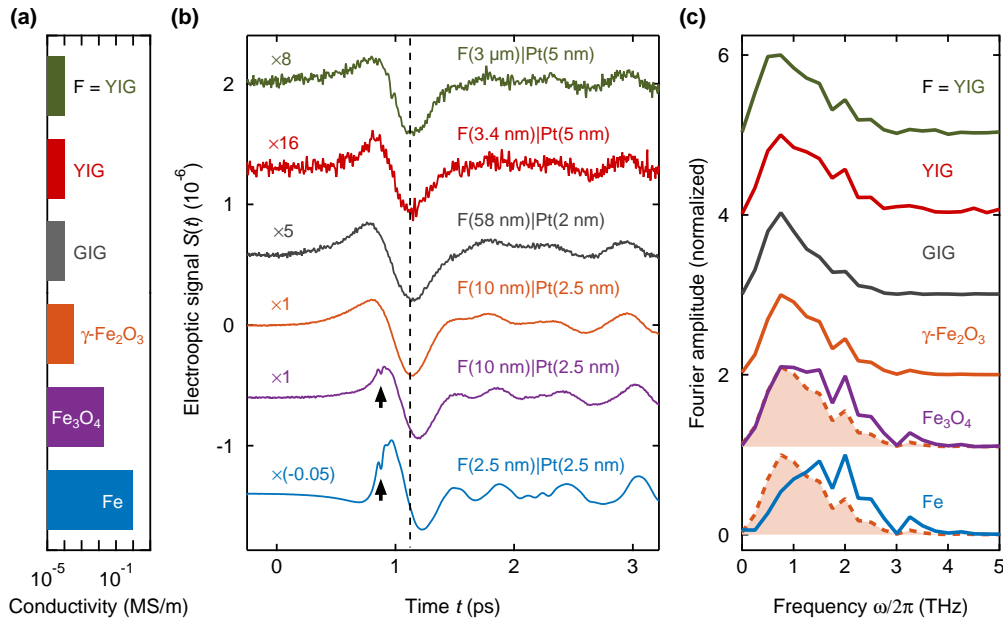
Figure 4.2. | Terahertz emission from F|Pt bilayers as a function of F conductivity. (a) Electrical conductivities of the studied F materials on a logarithmic scale. **(b)** Electro-optic signals of terahertz pulses emitted from various F|Pt bilayers with F = YIG (thick and thin), GIG, γ-Fe$_2$O$_3$, Fe$_3$O$_4$, and Fe. Note the different amplitude scalings. The time-axis origin is the same for all signals and was determined by the signal from Fe|Pt reference stacks (Fig. S1 in [cite paper]). The dashed vertical line marks the minimum signal for the insulating F materials YIG, GIG, and γ-Fe$_2$O$_3$, and the two black arrows label a sharp feature in the traces for F = Fe$_3$O$_4$ and Fe. **(c)** Fourier amplitude spectra of the signals of panel (b), normalized to peak height 1. Dashed lines show two duplicates of the spectrum of γ-Fe$_2$O$_3$|Pt. Curves in (b) and (c) are vertically offset for clarity.

GIG, and γ-Fe$_2$O$_3$ are largely transparent to the pump beam [Im(n^2) $\lesssim$ 1.5] [223, 293].

4.3 Results and discussion

A. Terahertz emission signals

Figure 4.2(b) shows electro-optic signals $S(t)$ [Eq. (4.1)] of terahertz pulses emitted by the Fe|Pt, γ-Fe$_2$O$_3$|Pt, Fe$_3$O$_4$|Pt, GIG|Pt, and the thinnest as well as the thickest YIG|Pt samples. Terahertz signals from all other YIG samples can be found in Fig. 4.3(a). Measurements of YIG(3 µm)|Pt(5 nm) [250] and Fe$_3$O$_4$|Pt confirm that the terahertz signal increases linearly with the pump power (Fig. S7 in Ref. [131]). We make two observations in terms of (i) signal shape and (ii) magnitude.

(i) The waveforms from all samples with YIG, GIG, and γ-Fe$_2$O$_3$ exhibit very similar dynamics (Figs. 4.2(b) and S3 in [131]). In contrast, the signal for Fe$_3$O$_4$ features a steeper initial rise, a sharp notch right before the first maximum (see black arrow), and a subsequent smaller peak. The global minimum is shifted to later times, as indicated by the dashed vertical line. This trend is even more enhanced for Fe|Pt and indicates
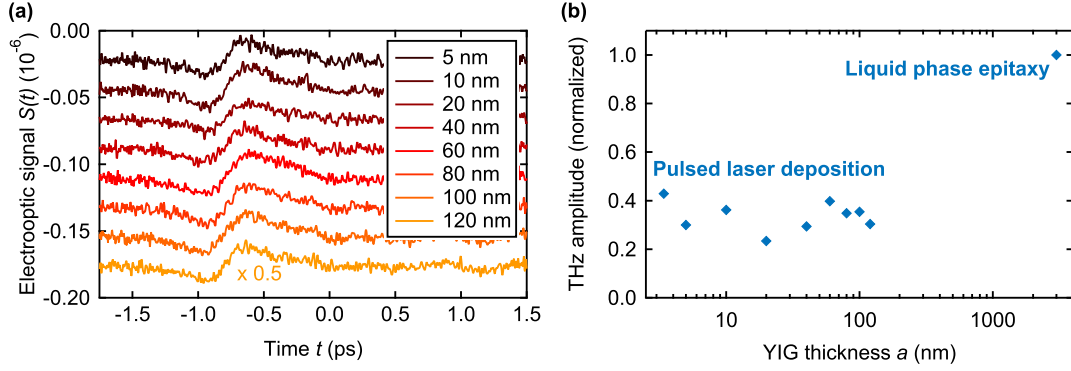
Figure 4.3. | Impact of film thicknesses of the YIG|Pt stacks on THz emission. (a) THz emission signals vs pump probe delay from YIG(a)|Pt(b) with varying YIG thickness ($a = 3.4\,\text{nm}$ and $b = 5\,\text{nm}$, $a = 5 - 120\,\text{nm}$ and $b = 3\,\text{nm}$, $a = 3\,\mu\text{m}$ and $b = 5\,\text{nm}$). The YIG thin films were grown by pulsed laser deposition, sputtering and liquid-phase epitaxy. **(b)** Amplitude (root mean square) of the THz signals of YIG(a)|Pt(b) vs YIG thickness a normalized to the largest peak signal.

that different processes occur in the samples as the F-material conductivity increases [Fig. 4.2(a)] [57, 58, 86, 262, 267].

(ii) While the signals from all YIG-based samples have similar strengths [Fig. 4.3], the signals from the γ-Fe$_2$O$_3$ and Fe$_3$O$_4$ samples are nearly one order of magnitude larger. The signal from Fe|Pt is even more than two orders of magnitude larger than from YIG|Pt.

By Fourier transformation of the time-domain waveforms $S(t)$ [Fig. 4.2(b)], the normalized amplitude $|S(\omega)|$ as a function of frequency $\omega/2\pi$ is obtained [Fig. 4.2(c)]. As expected from the time-domain data [Fig. 4.2(b)], the terahertz signal of the YIG, GIG, and γ-Fe$_2$O$_3$ samples have approximately the same amplitude spectrum. For Fe$_3$O$_4$, however, a slightly blueshifted spectrum with an increased bandwidth is found. This trend is more pronounced for the Fe|Pt spectrum.

B. Spin current for insulating F materials

As detailed above, we retrieve the spin-current dynamics from the measured terahertz signal waveforms. Figure 4.4(a) displays the resulting spin-current density $j_\text{s}(t)$ vs time t in γ-Fe$_2$O$_3$(10 nm)|Pt(2.5 nm), GIG(58 nm)|Pt(2 nm), and the YIG(3 μm)|Pt(5 nm) samples, normalized by the pump excitation density. We observe that (i) $j_\text{s}(t)$ in GIG|Pt, γ-Fe$_2$O$_3$|Pt, and all YIG|Pt samples exhibits very similar temporal dynamics. (ii) The overall amplitude of the spin current in γ-Fe$_2$O$_3$|Pt is about up to one order of magnitude larger than for the thinnest YIG|Pt samples. Observations (i) and (ii) are fully consistent with the temporal shape and global amplitude of the underlying raw data [see Fig. 4.2(b)]. They have four important implications.

1. SSE dynamics

First, it is remarkable that the optically induced spin currents in F|Pt bilayers proceed with the same dynamics, even though the magnetic layer is made of very different insula-

tors (F = YIG, GIG, and γ-Fe$_2$O$_3$) and covers, in the case of YIG, three different growth techniques. Note that, in these samples, the pump pulse is to the largest extent absorbed by the Pt layer. Therefore, observation (i) confirms the previous notion [250] that the ultrafast dynamics of the optically induced SSE current are solely determined by the relaxation dynamics of the electrons in the Pt layer as described in more detail in section 2.5.2.

2. Impact of YIG thickness

Second, finding (i) also implies that the dynamics of the spin current are independent of the YIG thickness, which covers a wide range from $3.4\,\mathrm{nm}$ to $3\,\mathrm{\mu m}$ (Fig. S2(b) in Ref. [131]). This result supports the notion [250] that the spin current traversing the YIG/Pt interface stems from YIG regions less than a few nanometers away from the YIG/Pt interface. It is easily understood given that magnons in YIG have a maximum group velocity of typically $<10\,\mathrm{nm/ps}$ [59] and that most of the ultrafast spin-current dynamics proceed within $<1\,\mathrm{ps}$ [Fig. 4.4(a)].

3. SSE amplitude and $g_r^{\uparrow\downarrow}$

Third, we observe that the spin current in the γ-Fe$_2$O$_3$|Pt sample is ~ 3 times higher than for the thickest YIG|Pt or GIG|Pt sample. To understand how this observation is related to the F/Pt interface, we consider Eq. (??) and note that the terahertz SSE coefficient equals [250]

$$\mathcal{K} = \frac{k_\mathrm{B}}{\pi} \frac{g_r^{\uparrow\downarrow}}{M_\mathrm{IF} V_\mathrm{int}}. \tag{4.2}$$

Here, k_B is the Boltzmann constant, and M_IF is the interfacial saturation magnetization. The real part $g_r^{\uparrow\downarrow}$ of the spin-mixing conductance describes the spin conductance of the F/Pt interface in terms of spin torque [Fig. 4.1(a)]. The volume V_int denotes the F volume with which a Pt conduction electron effectively interacts when it scatters off the F/Pt interface. At the ultrafast time scales of our experiment, V_int is given by the range of the exchange interaction between Pt and F, which approximately equals the lattice constant a of F according to ab initio calculations [129]. We, therefore, assume $V_\mathrm{int} = a^3$ [250]. On longer time scales, magnon propagation increases the effective interaction volume [303]. Consequently, in the DC SSE theory, V_int equals a magnon coherence volume [290, 303].

To determine the order of magnitude of $g_r^{\uparrow\downarrow}$ from the terahertz peak signal $\|S\|_\mathrm{max} = \max|S(t)|$, we note that the peak electron-temperature increase $\Delta \tilde{T}_e^\mathrm{N}(t)$ of Pt scales with A/d. Here, A denotes the total pump-pulse absorptance of the F|Pt sample, and d is the Pt-layer thickness. By combining Eqs. (??), (??), and (4.2), we obtain the scaling relation

$$g_r^{\uparrow\downarrow} \propto \frac{\|S\|_\mathrm{max} M_\mathrm{IF} a^3 d}{AZ}, \tag{4.3}$$

which allows us to provide a rough estimate of the magnitude of $g_r^{\uparrow\downarrow}$ relative to the YIG|Pt reference sample. While $\|S\|_\mathrm{max}$ [Fig. 4.2(b)] and A are measured [99], M_IF and a are taken from the literature [1, 52, 57, 61, 64, 70, 89, 95, 116, 132, 187, 198], where bulk saturation magnetization values are assumed for M_IF [1, 52, 57, 61, 116, 132, 187]. The impedance
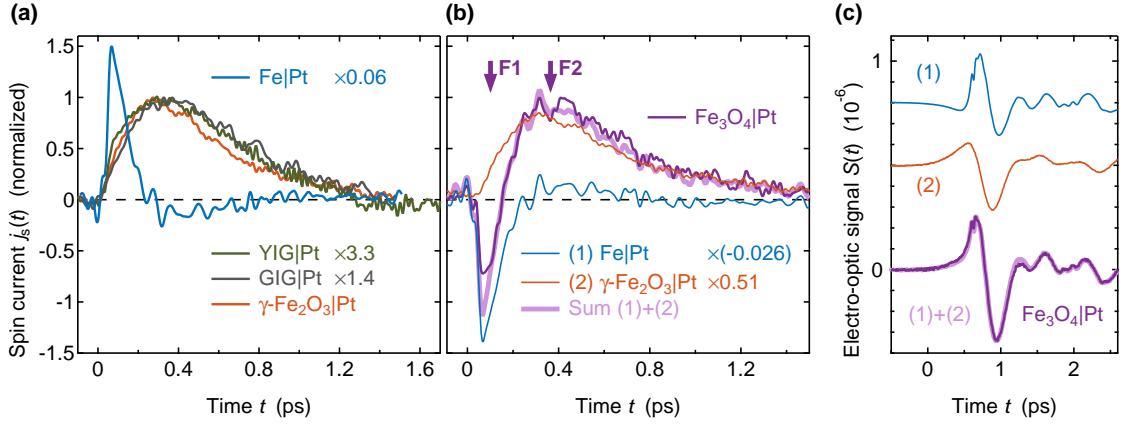
Figure 4.4. **Ultrafast photoinduced spin transport in F|Pt stacks.** **(a)** Curves show the spin-current density $j_s(t)$ in magnetic-insulator|Pt and Fe|Pt stacks, i.e., YIG$(3\,\mu m)$|Pt$(5\,nm)$, GIG$(58\,nm)$|Pt$(2\,nm)$, γ-Fe$_2$O$_3$$(10\,nm)$|Pt$(2.5\,nm)$, and Fe$(2.5\,nm)$|Pt$(2.5\,nm)$, as extracted from the terahertz emission signals of Fig. 4.2(b). Each signal is normalized by the pump-excitation density inside the Pt layer and by the indicated factor. **(b)** Spin current $j_s(t)$ in Fe$_3$O$_4$$(10\,nm)$|Pt$(2.5\,nm)$ along with scaled spin currents in γ-Fe$_2$O$_3$|Pt and Fe|Pt. The violet arrows F1 and F2 mark characteristic features of the curves. Note that $j_s(t)$ in Fe$_3$O$_4$|Pt can be well described as a linear combination of the other two spin currents (light violet curve). **(c)** Same as in panel (b), but for the terahertz-emission raw signals.

Z is calculated using Eq. (**??**) and the measured conductance [99] and literature values of the substrate refractive index [115, 151]. All values and references are summarized in Table 4.1 along with the inferred $g_r^{\uparrow\downarrow}$.

Table 4.1 indicates that $g_r^{\uparrow\downarrow}$ of the γ-Fe$_2$O$_3$/Pt interface is ~ 6 times larger than for the YIG/Pt reference. This value is consistent with previous measurements [60, 221, 290], which exhibit significant variations. For GIG/Pt, $g_r^{\uparrow\downarrow}$ is a factor of ~ 0.1 smaller than the YIG/Pt reference interface because the magnetizations of the two spin sublattices of GIG nearly compensate each other at room temperature. We are not aware of any previous $g_r^{\uparrow\downarrow}$ measurement of GIG/Pt.

4. Induced charge backflow

The SSE spin current [Eq. (**??**) and Fig. 4.4(a)] and, thus, charge current are nonnegative because $\Delta\tilde{T}_e^N \geqslant 0$ at all times. This observation suggests that the primary photocurrent $j_c = \theta_{SH}j_s$ [Eq. (**??**)] separates opposite charges in the Pt-film plane whose electric field induces a backflow j_{ind} of charge and the emission of a secondary terahertz wave. We note that this screening effect is already included in Eq. (**??**), which connects the terahertz field behind the sample with the primary photocurrent j_c, not the total current $j_c + j_{ind}$.

As shown in Ref. [252], Eq. (**??**) is an excellent approximation for all spatial Fourier components of the in-plane current distribution that contribute to the electro-optic signal S. For spatial Fourier components with larger in-plane wave vectors $\mathbf{k}_\parallel$, the impedance Z becomes $\mathbf{k}_\parallel$ dependent, indicating a more complex pattern of the induced current distribution. These spatial Fourier components, however, result in evanescent waves or are blocked by the effective apertures of our setup and, thus, do not propagate to the electro-

Table 4.1. | Material parameters of Fe, YIG, GIG, γ-Fe$_2$O$_3$, and Fe$_3$O$_4$. They are measured (d, A, σ_{Fe}, $\|S(\text{F}|\text{Pt})\|_{\text{max}}$), calculated ($Z(\text{F}/\text{Pt})$, $g_r^{\uparrow\downarrow}(\text{F}/\text{Pt})$), or taken from literature for the determination of the relative spin-mixing conductance $g_r^{\uparrow\downarrow}$ according to Eq. (4.3). Note that most of the experimentally acquired parameters are relative values and, therefore, normalized to the respective values of YIG. The bulk saturation magnetization of GIG is close to zero at room temperature. To account for the continuous heating of the sample by the pump beam, we took the GIG magnetization at 400 K. The other materials do not show such a drastic dependence of the saturation magnetization with temperature at our operating temperatures as GIG and are, therefore, given at room temperature (300 K).

Parameter	F = Fe	YIG	GIG	γ-Fe$_2$O$_3$	Fe$_3$O$_4$
Lattice constant a (nm)	0.286 [64]	1.252 [70]	1.247 [89]	0.834 [95]	0.8396 [198]
Bulk saturation magnetization μ_{B}/a^3	4.3 [57, 61]	29.6 [52, 57]	10.5 [1, 116]	25.0 [57, 132]	30.06 [57, 132]
Pt thickness d (nm)	2-5	5	2	2.5	2.5
F|Pt absorptance A	0.55	0.50	0.50	0.50	0.50
Conductivity σ (kS/m)	$\sim$1000	$\sim$0.1 [262]	$\sim$0.1 [267]	$\sim$0.35 [198]	$\sim$20 [253]
Infrared refractive index of substrate	-	3.5 [151]	3.5 [151]	3.07 [115]	3.07 [115]
Rel. impedance $Z(\text{F}|\text{Pt})/Z(\text{YIG}|\text{Pt})$	-	1.0	2.5	0.6	0.1
Rel. peak signal $\|S(\text{F}|\text{Pt})\|_{\text{max}}/\|S(\text{YIG}|\text{Pt})\|_{\text{max}}$	-	1.0	1.6	8.0	8.8
Rel. $g_r^{\uparrow\downarrow}(\text{F}/\text{Pt})/g_r^{\uparrow\downarrow}(\text{YIG}/\text{Pt})$	-	1.0	$\sim$0.1	$\sim$6	$\sim$45
$g_r^{\uparrow\downarrow}$ (10^{18} m^{-2}): previous work	-	$\sim$1-15 [221, 290]	-	$\sim$1-10 [60]	$\sim$4-20 [69, 214]

optic detection [252].

C. Spin current in Fe|Pt

The ultrafast pump-induced spin current in the Fe|Pt reference sample is shown in Fig. 4.4(a) (blue curve). It rises and decays much faster than the SSE-type spin currents in the F|Pt samples with a magnetic insulator [Fig. 4.4(a)].

As described in section 2.5.2, a previous work by Rouzegar *et al.* [231] showed that the spin-current dynamics in F|Pt stacks with ferromagnetic metallic F can be explained by the PSE, which we shortly repeat here for convenience and extend the description to the needs of this chapter: excitation by the pump pulse leads to a sudden increase of the electron temperature of F as well as of the spin voltage $\Delta\tilde{\mu}_{\text{s}}$, also called spin accumulation, which quantifies the instantaneous excess of spin density in F. As the system aims to adapt the F magnetization to the excited electronic state, spin angular momentum is transferred from the electrons to the crystal lattice of F and/or to the adjacent Pt layer. Remarkably, temperature gradients between F and Pt (i.e., the SDSE) were concluded to make a minor contribution on subpicosecond time scales [231], resulting in the simple relationship:

$$j_{\text{s}}(t) \propto \Delta\tilde{\mu}_{\text{s}}(t). \tag{4.4}$$

In the case of Fermi-Dirac distributions, $\Delta\tilde{\mu}_{\text{s}}$ equals the difference of the chemical potentials of spin-up and spin-down electrons, but the concepts of generalized spin voltage and temperature still apply for nonthermal electron distributions [231].

The transfer of spin angular momentum out of the F electrons into the crystal lattice or the Pt layer leads to a decay of the spin voltage on time scale τ_{es}. The dynamics of $j_{\text{s}}(t)$ is, thus, governed by τ_{es} and the relaxation of the electron excess energy of F, as

parameterized by the generalized electron excess temperature $\Delta \tilde{T}_e^{\mathrm{F}}$. Quantitatively, the dynamics of $\Delta \tilde{\mu}_{\mathrm{s}}(t)$ and, thus, $j_{\mathrm{s}}(t)$ can be described by [231]

$$\Delta \tilde{\mu}_{\mathrm{s}}(t) \propto \Delta \tilde{T}_e^{\mathrm{F}}(t) - \int_0^\infty \frac{d\tau}{\tau_{\mathrm{es}}} \exp\left(-\frac{\tau}{\tau_{\mathrm{es}}}\right) \Delta \tilde{T}_e^{\mathrm{F}}(t - \tau). \tag{4.5}$$

Following excitation by the pump [231], $\Delta \tilde{T}_e^{\mathrm{F}}$ immediately jumps to a nonzero value. The spin voltage $\Delta \tilde{\mu}_{\mathrm{s}}(t)$ and $j_{\mathrm{s}}(t)$ follow without delay, according to the first term of Eq. (4.5). Due to the subsequent transfer of spin angular momentum out of the F electrons, the spin voltage relaxes with time constant τ_{es}, as forced by the second term of Eq. (4.5).

Consequently, the spin current in Fe|Pt rises instantaneously within the time resolution of our experiment ($\sim 40\,\mathrm{fs}$) [231], much faster than in, for instance, YIG|Pt [Fig. 4.4(a)]. Its decay is predominantly determined by electron-spin equilibration on the time scale τ_{es}, with a minor correction due to the significantly slower electron-phonon equilibration [231]. To summarize, the very different dynamics of SSE (magnetic-insulator|Pt) and PSE (Fe|Pt) seen in Fig. 4.4(a) suggest that both effects and, thus, torque- and conduction-electron-mediated spin transport can be separated.

D. Spin current in Fe_3O_4|Pt

Figure 4.4(b) displays the spin current $j_{\mathrm{s}}(t)$ flowing from Fe_3O_4 to the Pt layer. We observe two features with different dynamics: (F1) a fast and sharp negative dip (see violet arrow F1), followed by (F2) a slower positive feature (arrow F2) that decays with a time constant of $0.3\,\mathrm{ps}$. As Fe_3O_4 is a halfmetal, it is interesting to compare the dynamics in Fe_3O_4|Pt to those in the two F|Pt stacks with the insulator $F = \gamma\text{-}Fe_2O_3$ and the metal $F = Fe$ [see Fig. 4.4(b)]. For $F = \gamma\text{-}Fe_2O_3$, the spin current across the F/Pt interface is mediated by spin torque, whereas for $F = Fe$, it is predominantly carried by spin-polarized electrons.

Note that the fast feature (F1) is comparable with $j_{\mathrm{s}}(t)$ of Fe|Pt (blue curve), whereas the slower feature (F2) resembles the $j_{\mathrm{s}}(t)$ of $\gamma\text{-}Fe_2O_3$|Pt (orange curve). As shown in Fig. 4.4(b), we are even able to reproduce the $j_{\mathrm{s}}(t)$ of Fe_3O_4|Pt by a sum of -0.026 $j_{\mathrm{s}}(t)$ of Fe|Pt and 0.51 $j_{\mathrm{s}}(t)$ of $\gamma\text{-}Fe_2O_3$|Pt. We emphasize that such very good agreement is also observed for the corresponding terahertz electro-optic signals of Fig. 4.2(b), as demonstrated in Fig. 4.4(c).

We confirm explicitly that other signal contributions are negligible: magnetic-dipole radiation due to ultrafast demagnetization of Fe_3O_4 (Fig. S4 in [131]) [13, 25, 122, 165, 231, 313] and signals due to Fe contamination of Fe_3O_4 by the nearby Fe reference layer, which would yield a signal like that from Fe|Pt [Fig. 4.5(a)].

To summarize, the spin current in Fe_3O_4|Pt can be very well represented by a superposition of spin currents in two very different samples comprising insulating and conducting magnetic materials, respectively. This remarkable observation strongly suggests that the spin current in Fe_3O_4|Pt has contributions from both the PSE, i.e., through spin-polarized electrons, [see (1) in Fig. 4.1(a)] and the SSE, i.e., through spin torque and magnons [see (2) in Fig. 4.1(a)].

E. Physical interpretation for Fe$_3$O$_4$|Pt

We suggest the following scenario to explain the coexistence of SSE and PSE in Fe$_3$O$_4$.

1. SSE

The pump excites mainly Pt and, thus, establishes a temperature difference between Pt electrons and Fe$_3$O$_4$ magnons, leading to the SSE spin current across the Fe$_3$O$_4$/Pt interface [Fig. 4.1(a), (2)]. From the measured spin-current amplitudes [Fig. 4.4(b)], we infer that the spin-mixing conductance of the Fe$_3$O$_4$/Pt interface is a factor of $\sim$ 45 larger than that of YIG/Pt [see Table (4.1)], consistent with the literature [69, 214]. The sign of the current agrees with that of YIG|Pt, suggesting the SSE in Fe$_3$O$_4$ is dominated by the A and B spin sublattices, whose total magnetization is parallel to the external magnetic field, whereas the e-sublattice is oppositely magnetized.

2. PSE

The pump also excites the hopping electrons of Fe$_3$O$_4$, either directly by optical absorption in Fe$_3$O$_4$ or by ultrafast heat transport from Pt to the interfacial Fe$_3$O$_4$ regions. Because magnetic order of the e-sublattice is understood to decrease with increasing temperature [28–30, 188], the spin voltage of the e-sublattice electrons changes upon arrival of the pump [Figs. 4.1(b) and 4.1(c)] and, thus, triggers spin transfer to the crystal lattice and/or the adjacent Pt layer [Fig. 4.1(a), (1)] [231]. Remarkably, as the e-sublattice spins are on average aligned antiparallel to the equilibrium magnetization $\boldsymbol{M}_0$ [Figs. 4.1(b) and 4.1(c)], the PSE tends to increase the magnitude of the total magnetization in Fe$_3$O$_4$, whereas in Fe, it is decreased. We, thus, interpret the observed opposite sign of the PSE currents in Fe$_3$O$_4$|Pt and Fe|Pt [Fig. 4.2(b)] as a hallmark of the ultrafast quenching of the residual magnetization of the e-sublattice minority hopping electrons in Fe$_3$O$_4$.

The much smaller amplitude of the PSE current in Fe$_3$O$_4$|Pt than Fe|Pt can have several reasons. First, the transport of spin-polarized electrons requires charge conservation [114, 169] and, thus, an equal backflow of charges. However, because the Fe$_3$O$_4$ spin polarization at the Fermi level is high (-72 %) [286], there are fewer majority states permitting the backflow electrons from Pt to Fe$_3$O$_4$ [231]. Second, the mobility of the Fe$_3$O$_4$ hopping electrons is likely lower than that of the Fe conduction electrons [28, 188]. Third, at room temperature, the magnetization of the e-sublattice is significantly smaller than the total Fe$_3$O$_4$ magnetization [188]. The nonvanishing e-sublattice magnetization inferred here suggests that its ferromagnetic-to-paramagnetic transition covers a wide temperature range, possibly because of sample imperfections such as impurities [188].

The relaxation time of the PSE is approximately given by the electron-spin equilibration time τ_{es}. Figure 4.4(b) suggests that the τ_{es} values of Fe$_3$O$_4$ and Fe are comparable and of the order of 100 fs. This conclusion is consistent with previous measurements of ultrafast demagnetization of Fe$_3$O$_4$, in which an instantaneous drop of the signal was observed directly after optical excitation [186].

It appears that the PSE dynamics does not significantly perturb the slower SSE dynamics, thereby suggesting that the e-sublattice does not excite magnons of the A and B spins to

a sizable extent on time scales $< 1\,$ps. Indeed, in laser-induced magnetization dynamics of Fe_3O_4 [186], the instantaneous signal drop was followed by a much larger component with a time constant $> 1\,$ns. To summarize, we can consistently assign the PSE current in Fe_3O_4 to the demagnetization of the e-sublattice-type minority hopping electrons at the Fermi energy.

F. Interface sensitivity

The relative values of the spin-mixing conductance $g_r^{\uparrow\downarrow}$ as inferred above are order-of-magnitude estimates. They need to be taken with caution in particular because $g_r^{\uparrow\downarrow}$, M_{IF}, and, thus, the SSE are very sensitive to the F/Pt interface properties and, therefore, to the growth conditions of the F|Pt stack [99, 101, 214]. For instance, as observed for YIG|Pt previously [250], the spin current amplitude may vary by up to a factor of 3 from sample to sample. Different interface properties may also explain the amplitude variations of the terahertz signals between the various YIG|Pt samples studied here [Fig. 4.3(b)].

For Fe_3O_4|Pt, the SSE contribution is robustly observed for samples with Pt grown at room temperature. However, when the Pt deposition temperature is increased to $720\,$K, the SSE component disappears [Fig. 4.5(b)]. We assign this effect to Pt-Fe interdiffusion at the interface, which magnetizes Pt in the vicinity of Fe, as reported previously [225, 279].
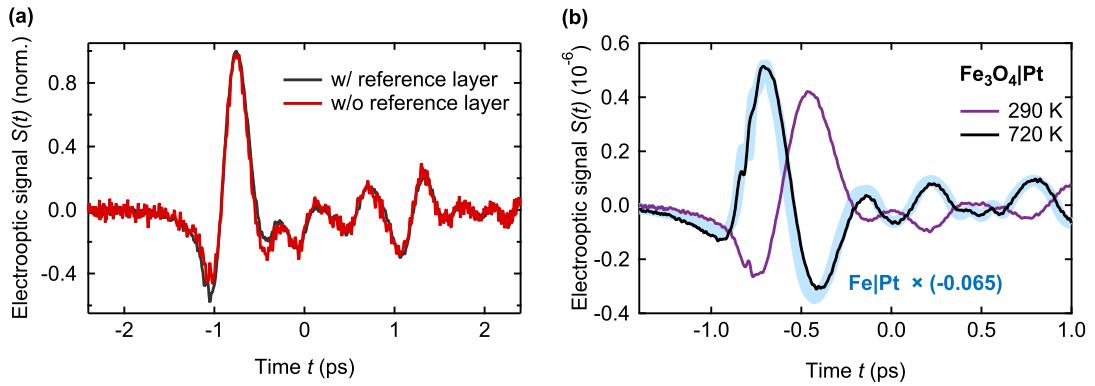
Figure 4.5. | Impact of the Fe reference layer and growth conditions on the THz emission signal from Fe_3O_4|Pt. (a) THz signal waveforms from Fe_3O_4|Pt with and without an additional Fe layer in adjacent lateral sample regions [see Fig. S1]. As the two signals exhibit almost identical temporal dynamics, we exclude that a sizeable number of Fe atoms is present on top of the nominally Fe-uncovered Fe_3O_4|Pt regions. **(b)** THz emission signals from Fe_3O_4|Pt stacks for different growth temperatures of the Pt layer: 290 K (violet line) and 720 K (black line). For the latter, the SSE contribution [maximum of the THz electric field at -0.4 ps (violet curve) due to slower spin current dynamics] is not observable any more, while the PSE contribution is still present. For comparison, the thick blue line shows the reversed THz signal from Fe|Pt.

4.4 Conclusion

We study ultrafast spin transport in archetypal F|Pt stacks following femtosecond optical excitation. For the ferrimagnetic/ferromagnetic layer F, model materials with different degrees of electrical conductivity are chosen. For the magnetic insulators YIG, GIG, and γ-Fe_2O_3, our results indicate a universal behavior of the interfacial SSE on ultrafast time scales: The spin current is solely determined by the relaxation dynamics of the electrons in the Pt layer, and it is localized close to the F/Pt interface.

Remarkably, in the half-metallic ferrimagnet Fe_3O_4 (magnetite), our measurements reveal two dynamical spin-current components, which exhibit opposite sign and PSE- and SSE-type dynamics. The SSE component is assigned to magnon excitation of the A and B spin sublattices [see (2) in Fig. 4.1(a)], whereas the PSE component can consistently be assigned to ultrafast demagnetization of e-sublattice minority-spin hopping electrons [(1) in Fig. 4.1(a)].

Our results show that measuring heat-driven spin currents faster than their natural sub-picosecond formation time allows one to unambiguously separate SSE and PSE contributions by their distinct ultrafast dynamics. Finally, insights into the physics of ultrafast spin transport are also potentially interesting for tailoring terahertz spin currents and for related applications such as spin torque [4, 152, 227] and spintronic emitters of terahertz radiation [40, 48, 77, 102, 108, 149, 249, 301].

5

THz spin-to-charge current conversion by interfacial skew scattering

The efficient conversion of spin to charge transport and vice versa is of major relevance for the detection and generation of spin currents in spin-based electronics. Interfaces of heterostructures are known to have a marked impact on this process. Here, terahertz (THz) emission spectroscopy is used to study ultrafast spin-to-charge-current conversion (S2C) in about 50 prototypical F|N bilayers consisting of a ferromagnetic layer F (e.g., $Ni_{81}Fe_{19}$, Co, or Fe) and a nonmagnetic layer N with strong (Pt) or weak (Cu and Al) spin-orbit coupling. Varying the structure of the F/N interface leads to a drastic change in the amplitude and even inversion of the polarity of the THz charge current. Remarkably, when N is a material with small spin Hall angle, a dominant interface contribution to the ultrafast charge current is found. Its magnitude amounts to as much as about 20 % of that found in the F|Pt reference sample. Symmetry arguments and first-principles calculations strongly suggest that the interfacial S2C arises from skew scattering of spin-polarized electrons at interface imperfections. The results highlight the potential of skew scattering for interfacial S2C and propose a promising route to enhanced S2C by tailored interfaces at all frequencies from DC to terahertz.

Publication information

Author contributions

TK, OG, TSS and LN conceived the experiments. OG performed the experiments and analyzed the data with support of LN, TSS, RR and GB. The theoretical calculations were done by MG. MV, JC, MAS, GJ and MK fabricated the samples. The manuscript was written by OG and TK with help and discussion contributions of all authors.

5.1 Motivation

The spin of the electron bears large potential as information carrier in future electronics [280]. An essential operation in spintronic devices is the transformation of spin into charge currents and vice versa [259]. A generic structure for studying such spin-to-charge-current conversion (S2C) is the prototypical bilayer of Fig. 5.1(a): A spin current with electron-number density j_s flowing along the z direction is converted into a transverse charge current with density j_c. S2C and its inverse process facilitate the efficient detection and generation of spin currents, the central element of spintronic operations [259]. A highly relevant application of the resulting spin current is to exert torque on nearby spins to switch their magnetic order [172], even with terahertz (THz) fields [204].

In a local picture, S2C may be described by the relationship

$$j_c(z) = \theta(z)j_s(z), \tag{5.1}$$

where the spin Hall angle (SHA) $\theta(z)$ quantifies the strength of S2C at position z. Note that a nonvanishing $\theta(z)$ can occur at any plane z in a metal bilayer [Fig. 5.1(b)]: In the bulk of the ferromagnet (F), the bulk of the nonmagnet (N), and at the two interfaces of the F layer. Major S2C effects are the inverse spin Hall effect (ISHE) [259] in nonmagnetic materials and ferro- or ferrimagnets and the inverse Rashba–Edelstein effect (IREE) [135, 317], the latter only occurring in regions with broken inversion symmetry like interfaces.

Recently, the operational speed of S2C was extended to ultrafast time scales using bilayer structures as that of Fig. 5.1(a). First, a femtosecond laser pulse was used to generate spin currents perpendicular to the plane through the ultrafast spin Seebeck effect [250] and ultrafast superdiffusive spin currents [50, 82, 85, 120, 171, 196, 240, 246, 302, 306, 310]. By means of S2C, the spin current was converted into an inplane ultrashort charge current burst giving rise to the emission of THz electromagnetic waves. This scheme has enabled new applications such as spintronic emitters of ultrashort THz electromagnetic pulses [82, 120, 196, 240, 246, 302, 306, 310].

In view of these applied aspects, a fundamental understanding and, eventually, control of S2C are highly desirable. Extensive research indicates that the most efficient materials for bulk S2C conversion are still Pt and W [259], which mainly rely on the ISHE due to their strong spin–orbit coupling. To boost S2C, researchers have, therefore, started studying the role of interfaces. Recent works have shown that tailored interfaces of nonmagnetic materials such as the interface between Bi and Ag exhibit sizeable S2C due to the IREE at sub-GHz frequencies [104, 237] and in the THz regime [121, 135, 158, 317]. Recently, THz emission even from single ferromagnetic layers was observed and ascribed to interfacial effects [309]. It is, thus, highly interesting to further explore interfacial S2C in terms of signatures beyond the IREE.

In this work, we study ultrafast laser-driven S2C in the F|N bilayer model system. To identify possible contributions of the F/N interface, we: i) consider all combinations out of six F and three N materials with bulk S2C of different strength and sign and ii) modify the interface while leaving F and N bulk as unaffected as possible. In bilayers with N = Cu

and Al, a surprisingly strong S2C is found, even though Cu and Al are known to have a negligible bulk ISHE. We show that S2C in these samples is drastically affected by modification of the interface. For example, in $Ni_{81}Fe_{19}|Cu$, the interface contribution is dominant and estimated to be as large as 20% of S2C in $Ni_{81}Fe_{19}|Pt$. Based on symmetry arguments and first-principles calculations, we consistently assign the interfacial S2C observed here to skew scattering of spin-polarized electrons at interface imperfections. Our results highlight a promising route to enhancing S2C by exploiting interface-related conversion mechanisms.

5.2 Experimental details

1. Experiment design

A number of methods to measure the strength of S2C of a given F|N bilayer sample are available [177]. Here, we make use of THz emission spectroscopy for the following reasons: First, it features a large sample throughput per time, which is essential for the large number (≈ 50) of samples of our study. Second, THz emission spectroscopy can be applied to as-grown bilayers without micro-structuring. Finally, the high signal-to-noise ratio permits the investigation of samples with relatively small S2C strength [246]. We emphasize that THz emission spectroscopy was shown to deliver values of the relative S2C conversion strength which are fully consistent with values extracted from established electrical techniques based on broadband ferromagnetic resonance [177], harmonic Hall measurements [177] and the DC spin Seebeck effect [59].

Our THz emission spectrometer is schematically shown in Fig. 5.1(a) and described in sections 3.1 and 3.4.1 in chapter 3. The transient electric field $E(t)$ of the emitted THz pulse is detected by electro-optic sampling [see section 3.3] in the far-zone, resulting in an electro-optic signal waveform $S(t)$ that is related to $E(t)$ through a linear transfer function [37, 250].

2. Sample details and characterization

Our samples are metallic F|N bilayers with an MgO protective coating. They are deposited on glass substrates by sputtering, resulting in the sample structure glass $(500\,\mu m)||F(3\,nm)|$ $N(6\,nm)|MgO(3\,nm)$. To identify possible interface contributions to S2C, we first consider all combinations of six common ferromagnetic materials (such as Fe, Permalloy Py $(Ni_{81}Fe_{19})$, and Co) and three common nonmagnetic materials (Pt, Cu, and Al) with different magnitude and sign of their bulk S2C. In this way, we vary the S2C strength θ (Eq. (5.1)) of the N layer from strong (Pt) to very weak (Al or Cu) and of the F layer from positive (Py, like Pt) to negative (Fe or Co) [180, 190, 285]. The direction of the F-layer magnetization $\pm\boldsymbol{M}$ is set by an external magnetic field that is sufficiently strong to saturate the sample magnetization. In a second step, we modify the F/N interface while leaving F and N bulk as unaffected as possible.

To further characterize our F|N bilayers, we measure their optical absorptance A and THz impedance Z. Both A and Z are important to normalize the measured THz emission signals, thereby enabling a direct comparison of the S2C strength between different samples
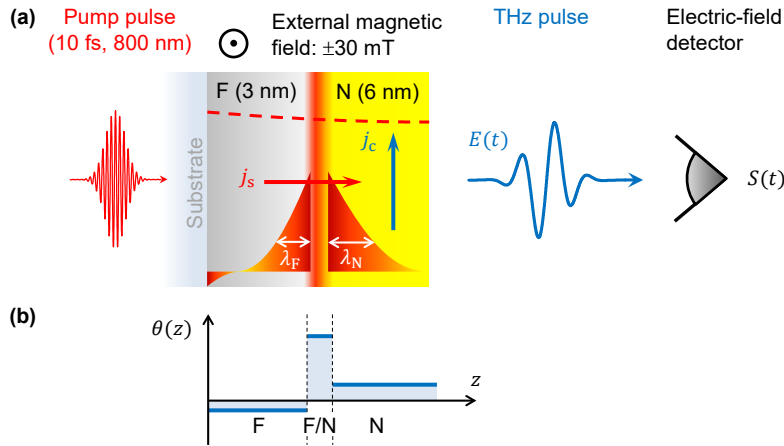
Figure 5.1. | **Photoinduced spin transport and spin-to-charge current conversion (S2C) in F|N bilayers.** **(a)** Side view of a F|N bilayer consisting of a ferromagnetic metal layer (F) and an adjacent nonmagnetic metal layer (N). A femtosecond laser pulse excites the metal stack from the substrate side. The calculated pump-field profile inside the bilayer is indicated by the red dashed line. The optical excitation drives a spin current from F to N whose density $j_s(z,t)$ decays on the length scales λ_F and λ_N as the distance from the F/N interface increases. Spin current also flows in the vicinity of the F/substrate interface. At any position z, j_s is converted into a charge current with density j_c, leading to the emission of a THz electromagnetic pulse. **(b)** Example of a possible z-dependence of the local S2C strength $\theta(z)$ in the F|N bilayer [Eq. (5.1)]. F/N denotes the interface region.

[252].

5.3 Results and discussion

A. Raw data

The THz waveforms seen in Fig. 5.2, which displays typical THz emission signal waveforms, were obtained from Py|N bilayers for N being Pt, Cu, and Al. We focus on the signal component odd in the sample magnetization,

$$S(t) = S(t, \boldsymbol{M}) - S(t, -\boldsymbol{M}), \tag{5.2}$$

which strongly suppresses all non-magnetic contributions to the signal. It is typically at least one order of magnitude larger than the even signal $S(t, \boldsymbol{M}) + S(t, -\boldsymbol{M})$ (see Fig. S1a in Ref. [99]). The signal strengths observed for Py|Cu and Py|Al are quite sizeable relative to that of Py|Pt, which is known to exhibit strong S2C.

We note that the signal waveforms $S(t)$ have approximately the same shape for all samples, apart from a global scaling factor [Fig. 5.2 and Fig. S1b in Ref. [99]]. To compare signals from different samples, it is therefore sufficient to consider amplitudes, which are obtained by taking the root mean square (RMS) of the waveform multiplied with the waveform's
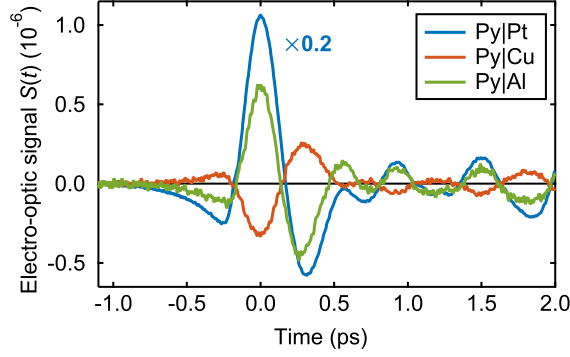
Figure 5.2. | THz emission from Py|N. The curves show time-domain electro-optic signals $S(t)$ of THz pulses emitted from photoexcited Py|N bilayers, where N is Pt, Cu, or Al. All shown signals are odd with respect to the sample magnetization $\boldsymbol{M}$ [see Eq. (5.2)]. Note the rescaling factor for Pt.

polarity (± 1). We checked that the signal grows linearly with pump power (Fig. S2 in Ref. [99]).

B. Evaluating the S2C strength

To evaluate the strength of S2C, one needs to extract the amplitude of the charge current [250, 252]. We, therefore, consider the relationship between the THz field and the charge-current density j_c flowing in the sample plane. In electric-dipole approximation, the Fourier amplitude of the THz electric field directly behind the sample [see Eq. (2.63)] is given by [250]

$$E(\omega) = eZ(\omega)I_c(\omega) = eZ(\omega) \int \mathrm{d}z \, j_c(z, \omega).$$ (5.3)

Here, Z is the measured sample impedance, which quantifies the charge-current-to-field conversion efficiency. It is found to be approximately constant over the range from 0 to 5 THz (see Fig. S3 in Ref. [99]). Because the THz signal is found to grow linearly with the absorbed pump fluence (see Fig. S2 in Ref. [99]), the current density j_c and, thus, the sheet charge current $I_c = \int \mathrm{d}z \, j_c$ do also.

With these insights, the following procedure is applied to each THz-signal waveform [180]: We i) take the RMS of $S(t)$ and normalize it by ii) the absorbed pump fluence and iii) the THz impedance Z. We, thus, obtain the RMS amplitude of the total sheet charge current I_c per deposited pump fluence, as shown in Figs. 5.3–5.6 and Figs. S4 and S5 in Ref. [99] for various sample parameters and divided by the amplitude of a F|Pt reference sample. Whereas Fig. 5.2 displays typical THz emission signal waveforms, Figs. 5.3, 5.5, and 5.6 show normalized THz pulse amplitudes as a function of 3×3 different F/N material combinations [Fig. 5.3] and for several interface variations [Figs. 5.5 and 5.6]. The amplitude of the Py|Pt sample in Figs. 5.3–5.6 is set to unity. The corresponding values for Z and the absorbed pump power can be found in Table S1 in Ref. [99].

Figure 5.3 displays the THz-current amplitude for all combinations of the F-layer materials Py, Fe, Co and the N-layer materials Pt, Cu, and Al. In particular, Fig. 5.3(a) (F = Py)
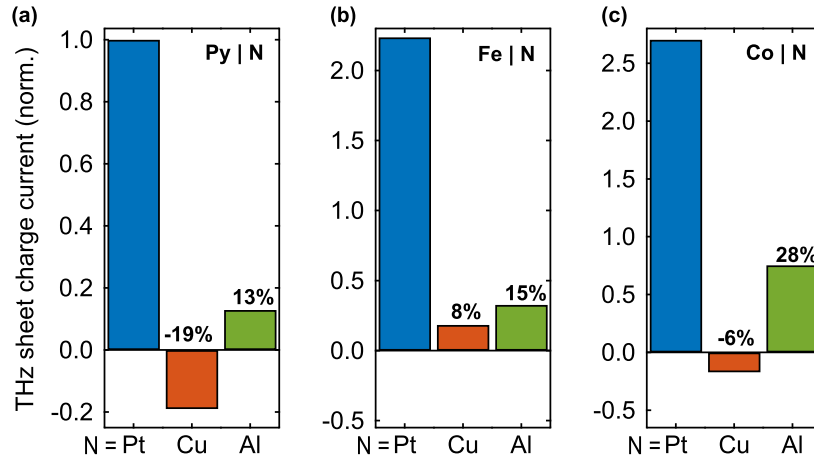
Figure 5.3. | THz charge-current amplitude from 3 × 3 different F|N samples. Bars show the root-mean-square amplitude of the THz sheet charge current, normalized by the absorbed pump power from **(a)** Py|N, **(b)** Fe|N and **(c)** Co|N bilayers where N is Pt, Cu, or Al. All amplitudes are normalized to the THz emission of Py|Pt. In each panel, the percentage above the F|Cu and F|Al bar quantifies the THz amplitude from these samples relative to that of the respective F|Pt reference bilayer.

demonstrates that the charge current amplitude of Py|Cu and Py|Al, respectively, amounts to -19 % and 13 % of that found for Py|Pt. To summarize, for all ferromagnets F, we find sizeable S2C efficiencies on the order of 10 % relative to the F|Pt reference sample.

C. Impact of F and N materials

To discuss the charge-current amplitudes of Fig. 5.3 in more detail, we make two assumptions. i) Immediately after optical excitation, there is a net spin current from F to N, resulting in a transient decrease of the F magnetization. Therefore, an F/N interface with modified spin transmittance coefficients will only change the magnitude of j_s at this interface, but not its sign. We consider a violation of this assumption very unlikely.

First, if j_s flowed from N to F, it would increase the magnetic moment of F. Such behavior appears unphysical because the magnetization of the ferromagnets considered here is known to decrease upon heating. Second, previous works on a number of F|N stacks reported a THz peak field whose sign and order of magnitude were consistent with the SHA θ_N of the N-layer material [246, 252]. This observation indicates that the spin current was always flowing in the same direction, that is, from F to N, directly after optical excitation. ii) The total charge current can be written as a sum of S2C in the F-bulk, N-bulk, at the F/N interface and at the metal/insulator (I) interfaces [Fig. 5.1(b)]. Using Eqs. (5.2) and (5.3), we, thus, obtain the sheet charge current $I_c = \int dz\, \theta(z) j_s(z)$, that is,

$$I_c = \left[(\lambda\theta)_F + (\lambda\theta)_N + (\lambda\theta)_{F/N} \right] j_{s0} + I_{c,F/I}, \qquad (5.4)$$

where j_{s0} is the total spin current density traversing the F/N interface. The λ_j are effective

electron propagation lengths over which S2C takes place [Fig. 5.1(a)]. In the F and N bulk, S2C is due to the ISHE. Prior work suggests that on ultrafast time scales, λ_F and λ_N can be considered as mean free-path lengths of electrons [318] in F and N, with $\lambda_N \approx 1\,\mathrm{nm}$ and $1.9\,\mathrm{nm}$ for $N = Pt$ [252] and Cu [Fig. 5.4], respectively, and $\lambda_F < 1\,\mathrm{nm}$ for $F = Fe$ [246, 306]. For the F/N interface, the length $\lambda_{F/N}$ has a less straightforward interpretation. For an ideal interface, $\lambda_{F/N}$ could be considered as the extension of interface states along z or as the mean free path of an electron after it has traversed the interface. For a nonideal interface, one could interpret $\lambda_{F/N}$ as the thickness of the sheet in which F and N materials are intermixed. Finally, the term $I_{c,F/I}$ in Eq. (5.4) accounts for S2C at the F/I interface [309], while S2C at the N/I interface was neglected because the decay length λ_N [Fig. 5.4] is significantly smaller than the N-layer thickness of 6 nm [see Fig. 5.1(a)].

We start by considering the ISHE in the N layer. From previous works [82, 120, 196, 246, 252], we know that in F|Pt samples, S2C is dominated by the ISHE of Pt. We, therefore, consider the signal from these samples as a reference. For $N = Cu$ and Al, in contrast, the bulk ISHE angle is known to be only a fraction ($\approx 10^{-4}...10^{-3}$) of that of Pt [259]. However, in our experiment [Fig. 5.3], we observe one to two orders of magnitude larger signals for $N = Cu$ and Al than what is expected from the strength of the ISHE in the N bulk. We conclude that the signal from F|Cu and F|Al predominantly arises from the ISHE in F and/or from S2C at the F/N and F/I interfaces.

Let us tentatively assume that S2C in F|Cu and F|Al is dominated by the ISHE in F. Due to a possibly different spin transparency of the F/N interface, the magnitude of j_{s0} can be different for F|Cu and F|Al. However, the sign of j_{s0} remains the same (see assumption (i)), and so does the sign of the charge current j_c in F. This expectation contradicts the sign change seen for Py|Al versus Py|Cu [Fig. 5.3(a)] and Co|Al versus Co|Cu [Fig. 5.3(c)]. Furthermore, as both the anomalous Hall and spin Hall angles of Fe and Co are negative [190, 285, 288], we should obtain the same sign of the THz current in Fe|N and Co|N. This expectation is, again, in contrast to the sign change observed for Fe|Cu and Co|Cu [Fig. 5.3(c)]. Therefore, the data of Fig. 5.3 strongly suggest that the F/N and F/I interfaces make a significant contribution to the S2C in our F|Cu and F|Al bilayer samples.
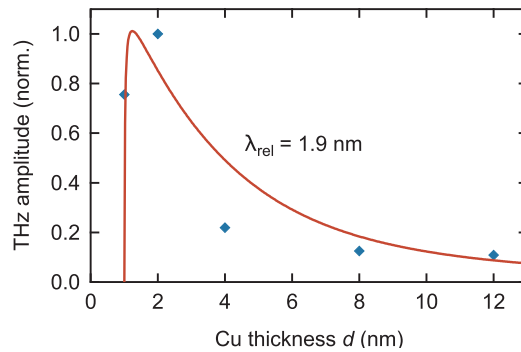
Figure 5.4. | Spin relaxation length in Cu. THz emission amplitude(root mean square) from Py|Cu samples as function of the Cu-layer thickness. The red solid line depicts a fit based on the model in Ref. [252]. We obtain a relaxation length of $\lambda_{rel} = 1.9\,\mathrm{nm}$.
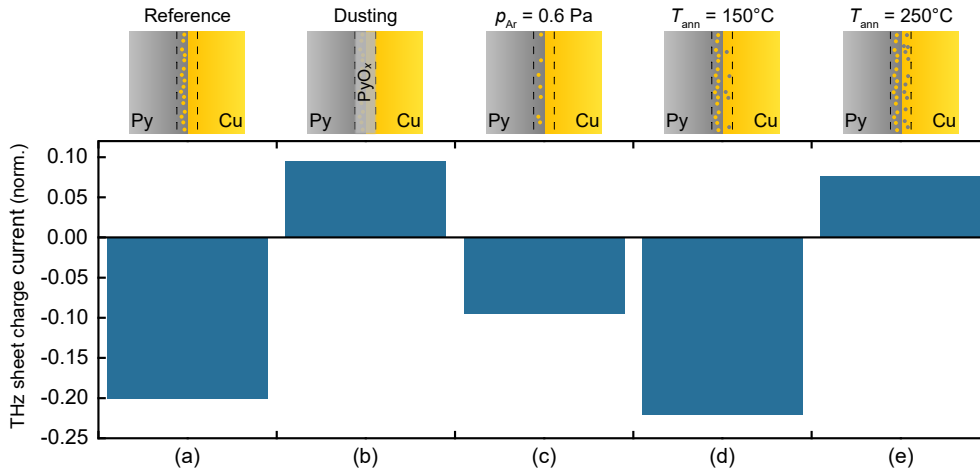
Figure 5.5. | Impact of Py/Cu interface structure on THz emission. Bars show the root-mean-square amplitude of the THz sheet charge current, normalized by the absorbed pump power, for Py|Cu bilayers grown under various conditions: **(a)** the Py|Cu reference [see Fig. 5.2], **(b)** Py|PyOx|Cu with a PyOx dusting layer (thickness of 0.1 nm), **(c)** Py|Cu deposited under a sputter gas pressure of $p_{Ar} = 0.6$ Pa, and **(d)** Py|Cu ex situ annealed at $T_{ann} = 150°$C and **(e)** 250°C. In all configurations, the sample is optically excited from the left-hand side. The schematics (top row) show the expected qualitative interface structure.

D. Modification of the Py/Cu Interface

To dedicatedly address the significance of the F/N interface, we varied the interface between Py and Cu by modifying the growth conditions of the Py|Cu stacks as qualitatively indicated by the schematics of Fig. 5.5. First, we dusted the Py/Cu interface by 0.1 nm of Py oxide (PyOx). When we compare the charge-current amplitude from the standard Py|Cu bilayer [Fig. 5.5(a)] to the Py|PyOx|Cu sample [Fig. 5.5(b)], we observe a drastic impact: The THz charge current reverses sign, and its magnitude reduces by about 50 %. We note that a modified spin transparency of the interface alone would only change the charge-current magnitude, but not its sign (see assumption (i) in section 5.3). This result clearly shows that the Py/Cu interface can contribute significantly to S2C in Py|Cu bilayers and can result even in reversal of the sign of the resulting total charge current.

Second, we increased the sputter-gas pressure from the standard value $p_{Ar} = 0.3$ to 0.6 Pa. The expected effect on the Py|Cu bilayer structure is as follows: In the sputter deposition process, the atoms are emitted from a target due to the impact of argon ions with energies of typically 300 eV [305]. On their way to the sample substrate, the energy of the emitted atoms is reduced due to collision cascades, but it remains still far higher than the energy (≈ 0.2 eV) of thermally evaporated atoms. Upon arrival at the substrate, some of the more energetic atoms are implanted below the surface [see schematic in Fig. 5.5(a)]. This effect is most evident when metals are sputtered on semiconductors or insulators and considered as sputter damage [125, 144, 162, 220]. Therefore, when Cu is deposited on top of Py, some of the more energetic Cu atoms are implanted into the Py layer, leading to the asymmetric atomic distribution indicated in Fig. 5.5(a). By increasing p_{Ar}, the Cu atoms are slowed down more strongly by collisions on average before they arrive at the substrate. They

are, thus, expected to less likely penetrate into the existing Py layer, resulting in less Cu impurities in the Py interface region [Fig. 5.5(c)]. We find that for the Py|Cu sample grown at 0.6 Pa, the THz signal decreases by about 50 % [Fig. 5.5(c) and Fig. S7 in Ref. [99]], but it maintains its polarity relative to the Py|Cu reference sample [Fig. 5.5(a)]. This result suggests that implantation of less Cu atoms in the Py layer decreases the S2C strength.

Third, following growth, we annealed the Py|Cu reference sample to trigger thermally activated diffusion in the Py/Cu interfacial region [42, 88, 166]. The resulting interface is expected to become more symmetric in terms of the number of Cu defects in the Py layer and Py defects in the Cu layer [see schematics in Fig. 5.5(d)-(e)]. While an annealing temperature of $T_{\mathrm{ann}} = 150°\mathrm{C}$ [Fig. 5.5(d)] results in an increase of the THz emission amplitude of approximately just 10 %, annealing at $250°\mathrm{C}$ has a drastic impact again [Fig. 5.5(e) and Fig. S8 in Ref. [99]]: The THz signal amplitude of the Py|Cu sample changes sign and now agrees with the sign of the Py|Cu sample with oxygen-dusted interface.

Note that for all the samples considered in Fig. 5.5, the substrate/Py interface is not expected to be modified significantly. We conclude that the massive changes in magnitude and sign of the THz emission amplitude from these samples predominantly arise from S2C at the Py/Cu interface.

E. Impact of growth direction

The schematic of Fig. 5.5(a) suggests that the Py/Cu interface and, potentially, its S2C strength depend on the growth direction of the stack. We, thus, grew Py and Cu in reverse order, and the expected interface structures are qualitatively indicated by the schematics of Fig. 5.6. While for the Py|Cu bilayer, we expect implantation of Cu atoms in Py close to the Py/Cu interface [see Fig. 5.6(a)], the reverse behavior should occur for Cu|Py [see Fig. 5.6(b)]. This notion is supported by our X-ray reflectometry measurements which indicate that the interface of the Cu|Py bilayer is substantially smoother than that of the Py|Cu stack (see Section S3 and Fig. S6 in Ref. [99]). The asymmetry of sputtered Py/Cu and Cu/Py interfaces was already observed previously [166]. Interface asymmetry is also evident in Pt|Co|Pt and Pd|Co|Pd structures in which the total interface-induced Dzyaloshinksi–Moriya interaction does not vanish [65, 292]. Similarly, the exchange anisotropy at the top and bottom interfaces of Py|MnFe|Py has strongly different magnitude [150].

Here, we find that the THz emission amplitude from our reversely grown bilayer Cu|Py [Fig. 5.6(b)] exhibits the same sign and almost the same magnitude as that of the standard Py|Cu sample [Fig. 5.6(a)]. This remarkable behavior is in stark contrast to physically turning the Py|Cu sample by 180° around an axis parallel to the sample magnetization $\boldsymbol{M}$ [Fig. 5.6(c)]: The THz signal from the turned sample is a fully reversed version of that from the initial sample [Fig. 5.6(a)], in agreement with basic symmetry considerations (see Appendix A.1). We conclude that the Py|Cu bilayer and its counterpart Cu|Py with inverted layer structure are not mirror versions of each other, in agreement with the schematics of the expected qualitative interface structure of the two samples [see Figs.
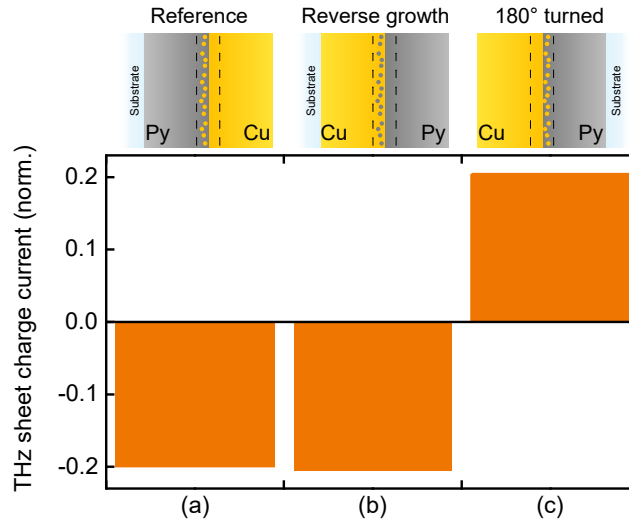
Figure 5.6. | Impact of bilayer growth direction on THz emission. Bars show the root-mean-square amplitude of the THz sheet charge current of Py|Cu and Cu|Py bilayers, normalized by the absorbed pump power: **(a)** the Py|Cu reference [see Fig. 5.2], **(b)** Cu|Py grown in reverse order, and **(c)** the physically turned reference sample of panel [(a),(c)]. All samples are optically excited from the left-hand side. The schematics (top row) show the expected qualitative interface structure.

5.6(a),(b)].

F. Suggested Scenario of Interfacial S2C

We ascribe the observations of Figs. 5.5 and 5.6 to skew scattering [112, 259] of laser-excited spin-polarized electrons off structural imperfections at the F/N interface [Fig. 5.7(a)]. These scattering centers exhibit a considerably different spin-orbit coupling relative to their environment. In our samples, they can, for instance, arise from oxygen interface dusting [Fig. 5.5(b)], from Cu impurities in Py (abbreviated Py(Cu)) and from Py impurities in Cu (short Py(Cu)) [Fig. 5.6(a),(c)]. Note that the difference of the number of valence electrons and, thus, of the spin-orbit coupling of host and impurity material in Py(Cu) versus Cu(Py) have opposite sign [97]. We, therefore, expect that skew scattering angles and the strength θ of S2C have opposite sign as well [Fig. 5.7(b)].

Our model along with the expected distribution of Py(Cu) and Cu(Py) impurities in the various samples can consistently explain all our observations of Figs. 5.5 and 5.6: When the number of Py(Cu) impurities decreases due to a higher sputter-gas pressure, the strength of S2C does also [Fig. 5.5(c)]. Likewise, when Cu(Py) impurities are added by annealing, they compensate and eventually exceed the S2C due to the Py(Cu) impurities, ultimately thereby resulting in a polarity change of the THz emission signal [Fig. 5.5(d),(e)]. Finally, in the Py|Cu and Cu|Py samples grown in reverse order, Py(Cu) and Cu(Py) impurities are expected to prevail, respectively [Fig. 5.7(a),(b)]. Therefore, values of θ with opposite sign result. Because the spin current has opposite direction, Py|Cu and Cu|Py samples deliver THz emission amplitudes of the same polarity [Fig. 5.6(a),(b)].
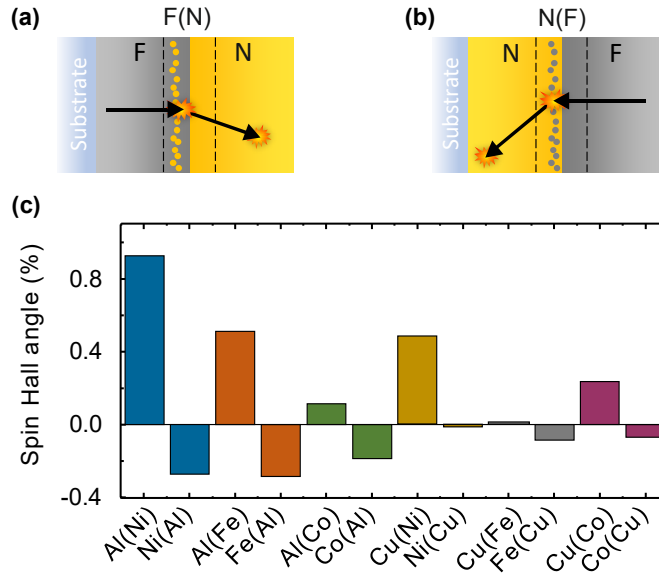
Figure 5.7. | Possible S2C by skew scattering at interfacial imperfections. **(a)** Growth of N = Cu on F = Py leads to an interfacial layer Py(Cu) of Cu atoms in a Py matrix. This layer gives rise to skew scattering of the laserexcited spin-polarized electrons originating from the Py layer. The black arrows indicate the mean velocity of an electron before and after traversal of the interface. The orange symbols represent scattering events. Note that the transverse charge current is enhanced by a long electron mean free path in N. **(b)** Same as (a) but with roles of Cu and Py exchanged. Note that the bilayers of panels (a) and (b) are not mirror versions of each other, and the Py(Cu) and Cu(Py) interface layers are expected to exhibit spin Hall angles of opposite sign. **(c)** Calculated spin-Hall angle for 1 atom% of A impurities in a host material B, denoted as B(A). In the convention used here, the spin-Hall angle of Pt is positive and of the order of 10 %.

G. Model Calculations

To put the scenario of Fig. 5.7(a),(b) on a more quantitative basis, we calculated the SHA of F(N) and N(F) alloys considering skew scattering as the only S2C process. We assumed a plausible impurity-atom fraction of 1 %, which coincides with the dilute limit for which scattering from different impurities can be considered independent. All transport calculations are based on the solution of a linearized Boltzmann equation including vertex corrections and assuming the limit of diluted impurity concentrations [97]. The input parameters were calculated from a fully relativistic Korringa–Kohn–Rostoker Green's-function method within density-functional theory and exploiting the local density approximation [96]. The impurity problem was solved on a real space cluster with a central substitutional impurity embedded in the infinite and perfect host crystal [319]. The results of the calculations are displayed in Figure 5.7(c).

First, the sign of the calculated SHA of F(N) and N(F) is always opposite, in agreement with the qualitative arguments in section F and with our experimental observations for reversely grown samples [see Fig. 5.6 and Figs. S7 and S8 in Ref. [99]].

Second, Cu(Py) defects cause significantly stronger and opposite deflection than Py(Cu) defects [Fig. 5.7(c)]. This behavior can well explain the sign change of the overall S2C of

the as-grown Py|Cu sample upon annealing [see Fig. 5.6(a),(d),(e)].

Third, to compare the order of magnitude of measured and calculated S2C, we estimate the SHA from our measurements. We assume S2C in Py|Pt is dominated by the Pt bulk ($I_c(\text{PyPt}) = j_{s0}\lambda_{\text{Pt}}\theta_{\text{Pt}}$), whereas in Py|Cu, it is dominated by the Py bulk and the Py/Cu interface ($I_c(\text{PyCu}) = j_{s0}\lambda_{\text{Py}}\theta_{\text{Py}} + j_{s0}\lambda_{\text{Py/Cu}}\theta_{\text{Py/Cu}}$, see Section D). We obtain

$$\theta_{\text{Py/Cu}} \approx \frac{I_c(\text{PyCu}) - I_c(\text{CuPy})}{I_c(\text{PyPt})} \cdot \theta_{\text{Pt}} \cdot \frac{\lambda_{\text{Pt}}}{\lambda_{\text{Py/Cu}}}. \tag{5.5}$$

The difference $I_c(\text{PyCu}) - I_c(\text{CuPy})$ cancels the contribution of S2C in the Py layer ($j_{s0}\lambda_{\text{Py}}\theta_{\text{Py}}$), which is expected to be the same for the two samples. In Equation (5.5), the first factor is ≈ 0.2 [Fig. 5.3(a)], $\theta_{\text{Pt}} \approx 0.1$ [200, 259, 314] and $\lambda_{\text{Pt}} = 1\,\text{nm}$ [246, 252], and the effective extension $\lambda_{\text{Py/Cu}}$ of the interface region is taken to be on the order of $1\,\text{nm}$ [213, 288]. We obtain $\theta_{\text{Py/Cu}} = 2\,\%$, which is in good agreement with the order of magnitude of the calculated SHA of Ni(Al), Al(Ni), Fe(Al), and Al(Fe). A similar conclusion can be drawn for the other systems shown in Fig. 5.3.

Note that Equation (5.1) implies a local S2C scenario, that is, j_c is determined by j_s at the very same position z. While this approach is appropriate for the intrinsic ISHE mechanism, the skew-scattering scenario of Fig. 5.7(a) is actually nonlocal: The charge current j_c behind the interface is determined by the wavevector change due to skew scattering right at the imperfect Py/Cu interface. Therefore, the transverse motion of the electron persists until the next scattering event in the "cleaner" bulk of the Cu layer occurs. In this picture, the characteristic length $\lambda_{\text{Py/Cu}}$ is rather given by the mean free path of the electron in Cu, which equals $1.9\,\text{nm}$ [see Fig. 5.4]. With this refined consideration, Equation (5.5) yields $\theta_{\text{Py/Cu}} = 1\,\%$, which agrees even better with the calculated values of the SHA. This value may still be overestimated because our analysis neglects a possible spin memory loss at the Py/Cu interface [229] [Eq. (5.4)] and the contribution $I_{c,\text{Py/I}}$ [Eq. (5.5)]. We conclude that the order of magnitude of the measured S2C strength $\theta_{\text{F/N}}$ of the F/N interfaces [Fig. 5.3] is in good agreement with the calculated values of the SHA of N(F) and F(N) materials [Fig. 5.7(d)].

H. Discussion

Our model calculations are consistent with the observations of Figs. 5.5 and 5.6 and the order of magnitude of the F-N interfacial S2C contribution. We did, however, not attempt to compare the signs of measured THz charge currents and calculated SHAs for all samples for two reasons. First, the actual interface structure (F(N) vs N(F)) is not known and may vary when the F or N material is changed. Second, the ISHE of the F layer may make another contribution to S2C and so add an offset to the measured THz charge current. The same argument applies to a contribution to the THz charge current from ultrafast demagnetization [313].

Regarding other S2C mechanisms, we cannot fully exclude contributions from the side-jump scenario [81] or the IREE [135, 317]. However, a sizeable IREE appears to be rather unlikely. First, the IREE requires strongly Rashba-split interface states that are

not trivially available in our samples since the N-layer materials Cu and Al lack strong spin-orbit interaction [212]. Second, from the Rashba perspective, the two Cu|Py samples of Fig. 5.6(b),(c) are approximately identical. Thus, a sign change of the IREE in these two samples is rather unexpected, in contrast to the experimental observation. Third, the good agreement of our experimental data with the calculated skew-scattering contribution strongly suggests that the other sources of S2C play a minor role in our samples.

5.4 Conclusion

In conclusion, we observed sizeable S2C induced by interfaces of F|N bilayers with weak bulk spin-orbit coupling, as large as 20% of S2C in F|Pt reference layers. Our results have important implications. First, they show that interfacial contributions to S2C need to be considered before the measured magnetization-dependent transverse charge current is assigned exclusively to bulk effects in the F or N layer. Second, interfacial S2C can arise from effects beyond the usually considered IREE mechanism. Sign and order of magnitude of the interfacial S2C observed here are consistent with a dominant role of skew scattering of spin-polarized electrons at F(N) and/or N(F) interface layers [Fig. 5.7(a)]. Third, the skew scattering off Cu(Py) interfacial imperfections [Fig. 5.7(b)] is enhanced by the relatively long relaxation length ($\lambda_{\mathrm{Py/Cu}} \approx 1.9\,\mathrm{nm}$) of the ballistically propagating electrons in the Cu layer [Fig. 5.4]. This remarkable nonlocal mechanism opens up a promising route to enhancing S2C by controlling the structure of the spintronic interface.

Ultrafast spin propagation and conversion in the antiferromagnet IrMn

Publication information

Author contributions

TK, VB, TSS and OG conceived the experiments. OG and RLS performed the experiments and analyzed the data in the THz and GHz frequency range with support of LN and VB, respectively with support of JNK and SG. The samples were fabricated by SA. The manuscript was written by LN, OG, VB, RLS and TK with help and discussion contributions of all authors.

7

Modulating the polarization of broadband THz pulses at kHz rates

Publication information

Author contributions

TK, TSS, LN and OG conceived the experiments. OG performed the experiments with support of LN and MB. GJ and MK fabricated the sample. OG and TK wrote the manuscript with help and discussion contributions of all authors.

8

Radiation hardness of spintronic terahertz emitters

Exploring space or other planets relies on appropriate tools. Remarkably, THz time-domain spectrometers are envisioned to be suitable optical tools for the identification of various gases or solids. While femtosecond laser systems are meanwhile successfully tested to meet the harsh conditions in space, suitable THz sources, ideally very broadband, still need to be found. Spintronic THz emitters (STEs) may be a good choice due to their unique and versatile properties. However, it remains open whether STEs can meet the requirements for space applications. Here, we test the radiation hardness of STEs with γ and high-energetic proton radiation and find STEs to be robust against these types of cosmic radiation. These results highlight even more the versatility of spintronic THz sources.

Publication information

Author contributions

8.1 Motivation

Spectroscopic methods in IR and THz have been proven to be very powerful in space research [256] due to the presence of many fundamental absorption modes of gases and solids in this frequency range, which are relevant for planetary research. The two established methods for planetary research, THz heterodyne [118] and Fourier-Transform Infrared spectroscopy (FTIR) [9], lack the required compactness due to their high complexity. This disadvantage makes them less favorable for robotic exploration missions.

THz time-domain spectroscopy, on the other hand, is an emerging technique which already successfully competes with FTIR. It has the potential to overcome the limitations of FTIR with respect to compactness, robustness while providing similar range of potential insights. To make existing THz TDS systems compatible with the harsh conditions of space missions,
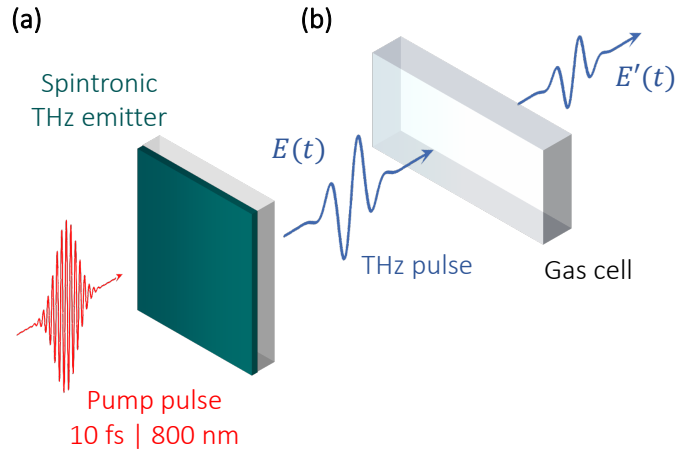
Figure 8.1. | THz transmission and emission spectroscopy. **(a)** A femtosecond laser pulse excites a spintronic THz emitter generating broadband THz pulses $E(t)$ with frequencies ranging from 1-30 THz. The emitted pulse $E(t)$ is either directly measured in an electro-optic detection (EOS) or **(b)** transmitted through a gas cell $E'(t)$. Subsequently, $E'(t)$ is measured by EOS.

one needs to test all components such as the femtosecond laser system, the THz source and detection unit for space-readiness. Recently, fiber lasers were demonstrated to be an excellent option for space applications, and they will become space-ready within the next few years [156]. Further, spintronic THz emitters (STEs) [246] may be a suitable THz source. They have been shown to be, e.g., cost-efficient, compact, scalable, on-chip-integrable and offer amplitude modulation at kHz rates [100, 117, 246, 247]. It remains to be tested whether STEs can withstand the harsh conditions emerging in space missions.

In this chapter, we (i) show how powerful THz time-domain spectroscopy can be for the identification of spectral fingerprints of gases and (ii) test the radiation hardness of spintronic THz emitters by irradiating them with γ-radiation and high-energetic protons. First, by measuring the transmission of ambient air, we identify water-vapor absorption lines between 1-13 THz and observe a bending mode of CO_2 at 20 THz. Second, we show that the spintronic THz emitter is robust against radiation levels of γ and proton radiation as required for missions to Mars or its moons.

8.2 Experimental details

To study the suitability of spintronic THz emitters for space applications, we perform linear and non-linear THz spectroscopic experiments. We use a femtosecond laser oscillator (see Chapter 3 for details) [Fig. 8.1(a)] to heat a metallic spintronic heterostructure N|F|N consisting of a ferromagnetic (F) and two non-magnetic (N) layers [246]. Upon excitation by the laser pulse a spin voltage [see section 2.5.2] and, thus, a longitudinal spin current j_s is generated [231] in the vicinity of the F/N and N/F interfaces and gets converted by the inverse spin Hall effect into two constructively superimposed charge currents j_c. Due to the pulsed excitation, j_c acts like an antenna and, thus, ejects an electromagnetic pulse

with frequencies in the THz regime [138, 246] [see Fig. 8.1(a) and section 3.2.2].

Using this source, we perform two types of THz spectroscopic methods: (I) THz emission to study the radiation hardness of the STE and (II) linear THz spectroscopy, where the STE serves as source of broadband THz pulses to demonstrate the sensitivity of THz transmission probes for the identification of various gases in a gas cell [Fig. 8.1(b)]. The emitted or transmitted broadband THz electric fields are measured by electro-optic sampling [139, 155] in a 10-μm-thick ZnTe(110) crystal. All experiments are performed in a dry atmosphere if not mentioned otherwise.

8.3 Preliminary results and discussion

A. Identification of gases

THz time-domain spectrometers are envisioned to be advantageous tools for space applications. Linear THz spectroscopy [Fig. 8.1] was already used to identify spectral fingerprints of water or NH_3 in a spectral range of 2.5-2.7 THz [73]. To expand the scope of elements to tag by spectroscopic methods, it is desirable to use broadband THz sources such as the spintronic THz emitter. In this regard, Fig. 8.2 shows two examples of how to utilize THz transmission spectroscopy: (1) for identification of water vapor absorption lines in
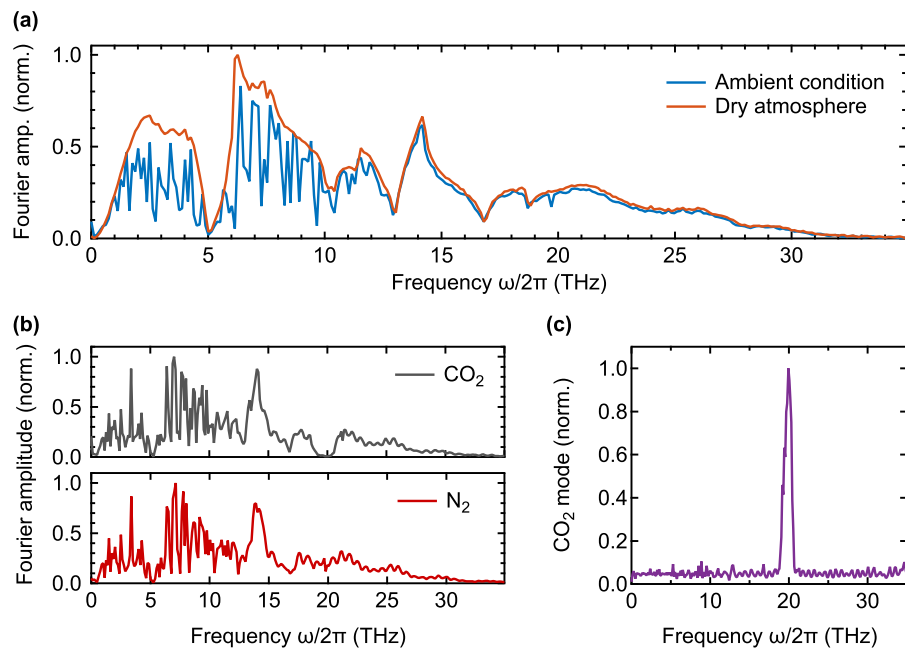
Figure 8.2. | THz spectroscopy for identification of water vapor and CO_2. **(a)** Broadband THz emission spectra from a spintronic THz emitter under ambient conditions (blue) and in a dry atmosphere (orange). The spectra are normalized. **(b)** THz transmission spectra from an STE transmitting through a gas cell which is filled with carbon dioxide CO_2 (top panel) or molecular nitrogen N_2 (bottom panel). Note the dip around 20 THz in the CO_2 transmission spectrum. **(c)** Extracted CO_2 extinction line from panel (b).

the spectral range from 1-13 THz [Fig. 8.2(a)] and (2) determination of an extinction line from carbon dioxide (CO_2) [Fig. 8.2(b)-(c)].

For (1), the measured amplitude spectrum in a dry atmosphere [Fig. 8.2(a), orange line] clearly lacks the extinction lines that are visible in the measurement under ambient conditions [Fig. 8.2(a), blue line]. Other features, which are arising in both spectra, are related to phonon absorption of the electro-optic detection crystal, a two-photon-absorption in Ge and the impedance of the sapphire substrate. Details can be found in Chapter 7.

For (2), in addition to the identification of water vapor also gases like CO_2 are detectable by THz time-domain spectroscopy [Fig. 8.2(b)-(c)]. Here, we compare the transmitted amplitude spectra of broadband THz pulses from an STE through a gas cell filled with either CO_2 [Fig. 8.2(b), upper panel] or molecular nitrogen (N_2) [Fig. 8.2(b), lower panel]. We make two observations: (i) water vapor absorption can be seen in both cases [Fig. 8.2(b)] because, in contrast to the data shown in Fig. 8.2(a), the THz pulses still travel through humidified air from the gas cell to the detection crystal. More importantly, (ii) the CO_2 spectra show a strong extinction around 20 THz. By division of the two spectra in Fig. 8.2(b), we can isolate this CO_2 extinction line as shown in Fig. 8.2(c) which is in good agreement with literature [174] reporting a CO_2 bending mode at 20 THz by resonant absorption. Interestingly, we also observe the CO_2 bending mode in the data shown in Fig. 8.2(a) which indicates how strong the absorption is considering the amount of CO_2 under ambient conditions to be in the order of hundreds of parts per million [153].

In summary, linear THz time-domain spectroscopy with broadband spintronic THz emitters is a sensitive and versatile tool for identifying spectral fingerprints of various gases, shown here for CO_2 and water vapor.

B. Irradiation of spintronic THz emitters

Before employing spintronic THz emitters for space applications, one needs to test how they would perform under the conditions in space. Here, we test one aspect, the radiation hardness of STEs, by intentionally irradiating them with different doses of high-energy γ and proton radiation. Both are the most severe types of radiation usually occurring for space applications [189]. We choose a radiation level up to 15 kRad that corresponds to the qualification tests required for components on space missions to Mars.

Figure 8.3(a) shows raw data THz signals $S(t)$ emitted from STEs irradiated with γ-radiation with an absorption dose from 1 to 15 kRad. An unirradiated STE serves a reference [Fig. 8.3(a), red line]. The corresponding amplitude spectra are shown in panel (b) of Fig. 8.3. We normalize each spectrum to the peak amplitude and offset them vertically for clarity.

Remarkably, we observe (i) only a very small impact on the amplitude and (ii) almost no change in the temporal dynamics upon irradiation. In detail, the amplitude spectra in Fig. 8.3(b) exhibit almost no change of the spectral content as a function of absorbed irradiation dose. Analogous conclusions as for the γ-irradiated STEs also apply to the proton-irradiated STEs (data not shown).
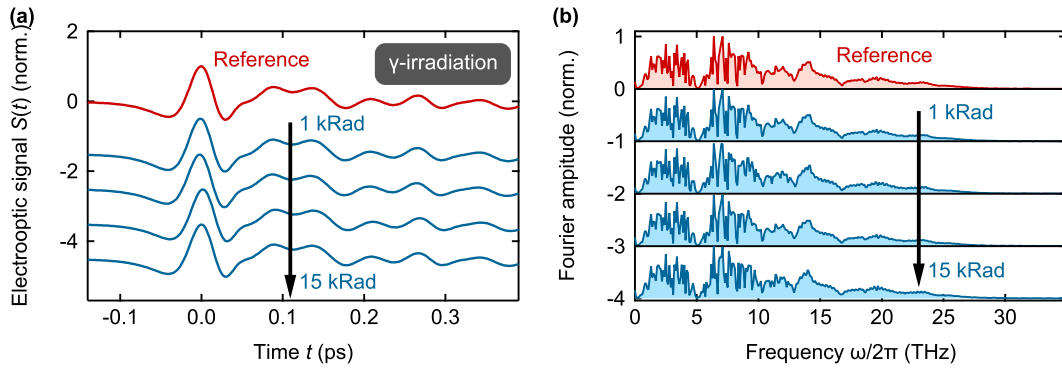
Figure 8.3. | THz emission raw data of γ-irradiated STEs. (a) Electrooptic signals $S(t)$ from an STE for various absorbed doses of γ-radiation. The non-contaminated STE reference is shown in red. **(b)** Fourier amplitude spectra of the THz waveforms from panel (a). The spectral content of the STEs remains constant under exposure of γ-radiation with an absorption dose up to $15\,\text{kRad}$.

Next, to judge the impact on the THz amplitude quantitatively, we contract the waveforms of Fig. 8.3(a) to a single value by taking the root-mean square of each waveform and plot them as a function of the absorbed irradiation dose in Fig. 8.4(a)-(b) for γ- and proton-irradiation, respectively. All data is normalized to the respective reference, which is shown as a red triangle. All STEs used for these irradiation tests are taken from the same growth batch and are characterized by THz emission spectroscopy before irradiation. Within a batch, we observe a deviation of the global amplitude up to $4\,\%$ (see light orange area in Fig. 8.4(a)-(b)), which includes systematic uncertainties.

On the one hand, we observe that the THz amplitude of γ-irradiated STEs lies within our confidential range and, thus, does not change under the influence of γ-radiation exposure. On the other hand, the proton-irradiated STEs show a decrease of their amplitude by $8\,\%$ compared to the reference STE, independent of the absorbed irradiation dose. Likely, the high-energetic protons, whose penetration depth into metals lies in the micrometer
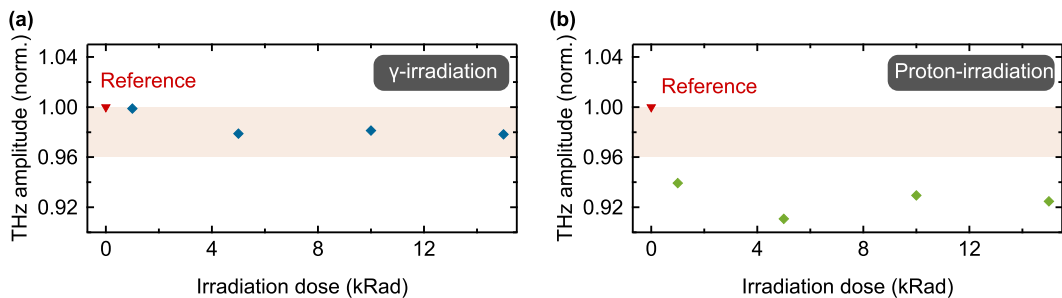
Figure 8.4. | Impact of γ and proton irradiation. (a) Root-mean-square values of the THz waveforms [Fig. 8.3(a)] as a function of the absorbed γ-irradiation dose. The non-irradiated STE serves as reference and is shown with a red triangle. All values are normalized to the reference. The light orange bar in the background shows the variation of $4\,\%$ of the emitted THz pulse amplitude from STEs from the same growth batch and systematic uncertainties. **(b)** Same as in panel (a) but for proton-irradiation.

range [255], modify the interface properties of the N/F/N heterostructure of the STEs. As reported in Chapter 5 and 6, the interface can drastically alter the THz emission amplitude upon interface modifications [99, 101].

8.4 Conclusion and future directions

In summary, we first exemplary show how THz time-domain spectroscopy driven by spintronic THz emitters could be employed for broadband identification of spectral fingerprints of gases such as water vapor or CO_2. Second, the STE is tested with regard to its radiation hardness for two major radiation sources, γ-radiation and high-energetic protons. We observe that they robustly withstand radiation levels as required for missions to Mars and, thus, highlights one aspect for space suitability of STEs.

In the future, we will test other parameters that are required for space readiness tests to meet the harsh conditions in space, e.g. the impact of the temperature on the emitted THz electric field from STEs.

9

Summary

In this thesis, fundamental aspects of spintronic heterostructures at highest frequencies are studied by THz emission spectroscopy. On an applied note, the suitability of spintronic THz emitters for fast polarization modulation spectroscopy and space applications is explored.

According to this twofold nature, the thesis begins with fundamental insights into the simultaneous spin transport by conduction electrons and magnons in a single material. We also validate crucial aspects of the microscopic model of the ultrafast spin Seebeck effect proposed in Ref. [250]. Subsequently, the ultrafast spin-to-charge current conversion at interfaces of metallic bilayers and in complex magnetic materials like antiferromagnets is explored. The second area deals with potential applications of spintronic THz emission and reveals, on the one hand, the unique property of spintronic THz emitters to allow for a fast modulation of its polarization polarity and direction at tens of kilohertz. On the other hand, spintronic THz emitters are found to be robust against the two most severe radiation sources impacting space applications. In detail:

A. THz spin currents from torque- and conduction-electron-mediated transport

We study ultrafast spin transport in prototypical ferrimagnetic/ferromagnetic|Pt bilayers where model materials with different degrees of electrical conductivity are employed for the F layer [see Chapter 4]. First, our results indicate that the interfacial spin Seebeck effect (SSE) spin current in all magnetic insulators is localized close to the F/Pt interface and its dynamics on ultrafast time scales is determined by the relaxation dynamics of the electrons in the Pt layer. Second, in the half-metallic ferrimagnet magnetite, our measurements reveal two dynamical spin-current components – one with slow SSE and the other with fast pyro-spintronic-type dynamics.

Our results point out that measuring heat-driven spin currents on their natural sub-picosecond time scale allows one to unambiguously separate SSE and PSE contributions by their distinct ultrafast dynamics. This insight may be interesting for tailoring terahertz spin currents and for related applications such as spin torque [4, 152, 227] and spintronic THz emitters [40, 48, 77, 102, 108, 149, 249, 301].

B. THz spin-to-charge current conversion by interfacial skew scattering

Another important operation for spintronics is spin-to-charge current conversion (S2C), which is the subject of Chapter 5. Here, we study the impact of the interface on ultrafast S2C in metallic bilayers systems of F|N. We observe a sizeable S2C induced by the F/N

interface with N layers with weak bulk spin-orbit coupling, which is as large as 20 % of the S2C in F|Pt reference samples.

Our results, including sign and order of magnitude of the interfacial S2C, are consistent with a dominant skew scattering process of spin-polarized electrons at F(N) and/or N(F) interfaces. This remarkable nonlocal mechanism opens up a promising route to enhancing S2C by controlling interface properties. This work also implies that interfacial contributions to S2C need to be considered before magnetization-dependent transverse charge currents are exclusively assigned to bulk S2C effects in the F or N layer.

C. Ultrafast spin propagation and conversion in the antiferromagnet IrMn

In Chapter 6, it is shown that ultrafast spin injection and S2C in the antiferromagnet IrMn are operative up to 30 THz. We estimate the upper bound of the spin-to-charge conversion efficiency in IrMn to roughly 10 % of the conversion in Pt. By comparing the results obtained by THz emission spectroscopy to ferromagnetic resonance measurements (FMR) in the GHz regime, it is revealed that the characteristic length of the spin transport is four times larger at GHz frequencies. We suggest that this feature arises from the dominance of ballistic electron transport in the THz regime, whereas in the GHz regime electronic diffusive transport dominates that is potentially superimposed by a magnonic contribution.

Finally, in the THz regime we find that again significant contributions of the interfaces can contribute to or even dominate the spin-to-charge current conversion processes. Thus, interfacial S2C may be useful for optimization of ultrafast spintronic functionalities in antiferromagnetic materials.

D. Modulating the polarization of broadband THz pulses at kHz rates

In Chapter 7, we turn to applications by adding a functionality to spintronic THz emitters. By modulating the magnetization of an STE by external magnetic AC fields, we show that the polarity of THz electromagnetic pulses from an STE can be controlled with a modulation contrast better than 99 % at modulation frequencies of up to 50 kHz. Two modes of polarization control are tested: in the polarity mode, the external AC magnetic field switches the magnetization and, thus, the polarity of the emitted THz electric field. By adding a perpendicularly oriented DC magnetic field, modulation of the direction of the THz peak field becomes possible. In both modes, the modulation is broadband and uniformly affects all spectral components of the THz pulse from 1 to 30 THz.

This work enables interesting applications in all kinds of modulation spectroscopy like low-noise probing of small magnetic effects in materials by THz emission spectroscopy [121, 231, 250] and THz transmission spectroscopy [193] or for THz time-domain ellipsometry [232]. Future work will aim at increasing the modulation frequencies in both modes to frequencies above 50 kHz and at extending our approach to a periodic full-circle rotation of the THz polarization plane.

E. Radiation hardness of spintronic terahertz emitter

Finally, the suitability of STEs for space applications is investigated [see Chapter 8]. First, it is demonstrated that broadband THz transmission spectroscopy is of added value for gas identification in space. Second, two radiation sources, γ and proton irradiation, which usually cause problems in the area of space flights, are analyzed. It is shown that STEs lose a few percent of their field amplitude under the maximum irradiation dose of the two types of radiation but their broadband spectrum remains unaffected.

This study lays the foundation for the potential use of STEs as broadband and versatile THz sources in the first integrated THz time-domain spectrometer for space applications.

Appendix

A.1 Basic symmetry considerations

The following symmetry analysis was published in the supporting information of Ref. [99] by Gueckstock *et al.* (2021).

We analyze what happens to the THz emission signal when the F|N sample is turned by $180°$ about an axis parallel to the F-layer magnetization $\boldsymbol{M}$. According to our experimental geometry [Fig. 5.1(a)], the THz emission originates from an in-plane charge current $\boldsymbol{I}_{c} = \int \mathrm{d}z\, \boldsymbol{j}_{c}(z)$ that is quadratic in the pump electric field $\boldsymbol{E}_{p}$ (see Fig. S2(b) in Ref [99]). Because $\boldsymbol{E}_{p}$ is approximately constant over the thickness of the F|N stack [Fig. 5.1(a)], we can write

$$I_{ci} = \sum_{j,k=1}^{3} d_{ijk}(\boldsymbol{M}) E_{pj} E_{pk}, \tag{A.1}$$

where the response function $d_{ijk}(\boldsymbol{M})$ is a 3rd-rank tensor depending on $\boldsymbol{M}$. The indices i, j and k can take the values 1,2,3, which refer to the x, y and z Cartesian components, respectively. In Eq. (A.1), the time dependence of I_{ci}, d_{ijk}, E_{pj} and E_{pk} and the integration over the time arguments of E_{pj} and E_{pk} is suppressed because they are not relevant for what follows.

We choose the z-axis parallel to the surface normal of the sample, and the magnetization is chosen to point along the x-axis. Therefore, a rotation by $180°$ about an axis parallel to $\boldsymbol{M}$ is described by the diagonal matrix $\underline{R}^{x} = \mathrm{diag}(1, -1, -1)$. Upon rotation of the sample, the response function of the sample transforms like a polar tensor according to Ref. [32]

$$d'_{i'j'k'}(\boldsymbol{M'}) = \sum_{i,j,k=1}^{3} R^{x}_{i'i} R^{x}_{j'j} R^{x}_{k'k} d_{ijk}(\boldsymbol{M}). \tag{A.2}$$

Because of $\boldsymbol{M'} = \underline{R}^{x}\boldsymbol{M} = \boldsymbol{M}$ and because $\underline{R}^{x}$ is diagonal, the summation in Eq. (A.2) is restricted to $i' = i$, $j' = j$ and $k' = k$, resulting in the simple product

$$d'_{ijk}(\boldsymbol{M}) = R^{x}_{ii} R^{x}_{jj} R^{x}_{kk} d_{ijk}(\boldsymbol{M}). \tag{A.3}$$

In our experiment, $\boldsymbol{I}_{c}$ is observed to be directed along the y-axis (perpendicular to $\boldsymbol{M}$), and $\boldsymbol{E}_{p}$ is oriented along either the x- or y-axis. We are, thus, only interested in d'_{ykk} with

$k = 1$ or 2, for which Eq. (A.3) becomes

$$d'_{ykk}(\boldsymbol{M}) = -d_{ykk}(\boldsymbol{M}). \tag{A.4}$$

We conclude that under the conditions of our experiment, the thickness-integrated charge current reverses sign when the sample is turned by 180° about an axis parallel to the sample magnetization.

Bibliography

[1] AAKANSHA AND S. RAVI, *Investigation of negative magnetization and impedance spectroscopy of sm-substituted gadolinium iron garnets*, Materials Research Express, 6 (2020).

[2] R. ACHARYYA, H. Y. T. NGUYEN, W. P. PRATT, AND J. BASS, *A study of spin–flipping in sputtered irmn using py-based exchange-biased spin-valves*, Journal of Applied Physics, 109 (2011).

[3] H. ADACHI, K. I. UCHIDA, E. SAITOH, AND S. MAEKAWA, *Theory of the spin seebeck effect*, Reports on Progress in Physics, 76 (2013), p. 036501.

[4] A. ALEKHIN, I. RAZDOLSKI, N. ILIN, J. P. MEYBURG, D. DIESING, V. RODDATIS, I. RUNGGER, M. STAMENOVA, S. SANVITO, U. BOVENSIEPEN, AND A. MELNIKOV, *Femtosecond spin current pulses generated by the nonthermal spin-dependent seebeck effect and interacting with ferromagnets in spin valves*, Physical Review Letters, 119 (2017), pp. 17202–17202.

[5] M. ALTHAMMER, *Pure spin currents in magnetically ordered insulator/normal metal heterostructures*, Journal of Physics D: Applied Physics, 51 (2018), pp. 313001–313001.

[6] N. AMER, W. C. HURLBUT, B. J. NORTON, Y.-S. LEE, AND T. B. NORRIS, *Generation of terahertz pulses with arbitrary elliptical polarization*, Applied Physics Letters, 87 (2005).

[7] V. P. AMIN AND M. D. STILES, *Spin transport at interfaces with spin-orbit coupling: Formalism*, Physical Review B, 94 (2016).

[8] Z. AN, F. Q. LIU, Y. LIN, AND C. LIU, *The universal definition of spin current*, Sci Rep, 2 (2012), p. 388.

[9] M. S. ANDERSON, J. M. ANDRINGA, R. W. CARLSON, P. CONRAD, W. HARTFORD, M. SHAFER, A. SOTO, A. I. TSAPIN, J. P. DYBWAD, W. WADSWORTH, AND K. HAND, *Fourier transform infrared spectroscopy for mars science*, Review of Scientific Instruments, 76 (2005), p. 034101.

[10] R. ARRAS, L. CALMELS, AND B. WAROT-FONROSE, *Electronic structure near an antiphase boundary in magnetite*, Physical Review B, 81 (2010), p. 104422.

[11] N. W. ASHCROFT AND N. D. MERMIN, *Solid State Physics*, Harcourt College Publishers, 1976.

[12] U. Atxitia, D. Hinzke, and U. Nowak, *Fundamentals and applications of the landau–lifshitz–bloch equation*, Journal of Physics D: Applied Physics, 50 (2016), p. 033003.

[13] N. Awari, S. Kovalev, C. Fowley, K. Rode, R. A. Gallardo, Y. C. Lau, D. Betto, N. Thiyagarajah, B. Green, O. Yildirim, J. Lindner, J. Fassbender, J. M. D. Coey, A. M. Deac, and M. Gensch, *Narrow-band tunable terahertz emission from ferrimagnetic mn3-xga thin films*, Applied Physics Letters, 109 (2016).

[14] S. Azzawi, A. T. Hindmarch, and D. Atkinson, *Magnetic damping phenomena in ferromagnetic thin-films and multilayers*, Journal of Physics D: Applied Physics, 50 (2017).

[15] M. N. Baibich, J. M. Broto, A. Fert, F. N. Van Dau, F. Petroff, P. Etienne, G. Creuzet, A. Friederich, and J. Chazelas, *Giant magnetoresistance of (001)fe//(001)cr magnetic superlattices*, Phys. Rev. Lett., 61 (1988), pp. 2472–2475.

[16] S. A. Baig, J. L. Boland, D. A. Damry, H. H. Tan, C. Jagadish, H. J. Joyce, and M. B. Johnston, *An ultrafast switchable terahertz polarization modulator based on iii-v semiconductor nanowires*, Nano Lett, 17 (2017), pp. 2603–2610.

[17] J. Ballato and U. J. Gibson, *Core opportunities for future optical fibers*, Journal of Physics: Photonics, 3 (2021).

[18] V. Balos, N. K. Kaliannan, H. Elgabarty, M. Wolf, T. D. Kuhne, and M. Sajadi, *Time-resolved terahertz-raman spectroscopy reveals that cations and anions distinctly modify intermolecular interactions of water*, Nat Chem, (2022).

[19] V. Baltz, A. Manchon, M. Tsoi, T. Moriyama, T. Ono, and Y. Tserkovnyak, *Antiferromagnetic spintronics*, Reviews of Modern Physics, 90 (2018).

[20] A. S. Barker, *Infrared lattice vibrations and dielectric dispersion in corundum*, Physical Review, 132 (1963), pp. 1474–1481.

[21] P. Barla, V. K. Joshi, and S. Bhat, *Spintronic devices: a promising alternative to cmos devices*, Journal of Computational Electronics, 20 (2021), pp. 805–837.

[22] M. Bass, P. A. Franken, J. F. Ward, and G. Weinreich, *Optical rectification*, Phys. Rev. Lett., 9 (1962), pp. 446–448.

[23] V. Basso, G. Bertotti, A. Infortuna, and M. Pasquale, *Peisach model study of the connection between magnetic and microstructural properties of soft magnetic materials*, IEEE Transactions on Magnetics, 31 (1995).

[24] G. E. W. Bauer, E. Saitoh, B. J. V. Wees, and P. St, *Spin caloritronics*, Nature Publishing Group, 11 (2012), pp. 391–399.

[25] E. Beaurepaire, G. M. Turner, S. M. Harrel, M. C. Beard, J. Y. Bigot, and C. A. Schmuttenmaer, *Coherent terahertz emission from ferromagnetic films excited by femtosecond laser pulses*, Applied Physics Letters, 84 (2004), pp. 3465–3467.

[26] M. Beck, H. Schäfer, G. Klatt, J. Demsar, S. Winnerl, M. Helm, and T. Dekorsy, *Impulsive terahertz radiation with high electric fields from an amplifier-driven large-area photoconductive antenna*, Optics Express, 18 (2010), pp. 9251–9257.

[27] M. Beens, R. A. Duine, and B. Koopmans, *s-d model for local and nonlocal spin dynamics in laser-excited magnetic heterostructures*, Physical Review B, 102 (2020), p. 054442.

[28] K. P. Belov, *Electronic processes in magnetite (or 'enigmas in magnetite')*, Physics-Uspekhi, 36 (1993), pp. 380–391.

[29] K. P. Belov, *Ferrimagnets with a weak magnetic sublattice*, Physics-Uspekhi, 39 (1996), pp. 623–634.

[30] K. P. Belov, *On the nature of a low-temperature transition in magnetite*, JETP, 36 (1996), pp. 1152–1155.

[31] G. Bierhance, A. Markou, O. Gueckstock, R. Rouzegar, Y. Behovits, A. L. Chekhov, M. Wolf, T. S. Seifert, C. Felser, and T. Kampfrath, *Spin-voltage-driven efficient terahertz spin currents from the magnetic weyl semimetals co2mnga and co2mnal*, Applied Physics Letters, 120 (2022), p. 082401.

[32] R. R. Birss, *Symmetry and Magnetism*, North-Holland Publishing Company, 1966.

[33] S. Blundell, *Magnetism in Condensed Matter*, Oxford University Press Inc., 2001.

[34] S. Y. Bodnar, L. Smejkal, I. Turek, T. Jungwirth, O. Gomonay, J. Sinova, A. A. Sapozhnik, H. J. Elmers, M. Klaui, and M. Jourdan, *Writing and reading antiferromagnetic mn2au by neel spin-orbit torques and large anisotropic magnetoresistance*, Nat Commun, 9 (2018), p. 348.

[35] S. R. Boona, R. C. Myers, and J. P. Heremans, *Spin caloritronics*, Energy Environ. Sci., 7 (2014), pp. 885–910.

[36] R. W. Boyd, *Nonlinear Optics*, Academic Press, Burlington, third ed., 2008.

[37] L. Braun, G. Mussler, A. Hruban, M. Konczykowski, T. Schumann, M. Wolf, M. Munzenberg, L. Perfetti, and T. Kampfrath, *Ultrafast photocurrents at the surface of the three-dimensional topological insulator bi2se3*, Nat Commun, 7 (2016), p. 13259.

[38] L. Z. Braun, *Electron and Phonon Dynamics in Topological Insulators at THz Frequencies*, PhD thesis, Freie Universität Berlin, Berlin, 2016.

[39] E. Bründermann, H.-W. Hübers, and M. FitzGerald Kimmitt, *Terahertz Techniques*, Springer, Berlin, 2012.

[40] C. Bull, S. M. Hewett, R. Ji, C.-H. Lin, T. Thomson, D. M. Graham, and P. W. Nutter, *Spintronic terahertz emitters: Status and prospects from a materials perspective*, APL Materials, 9 (2021).

[41] N. M. Burford and M. O. El-Shenawee, *Review of terahertz photoconductive antenna technology*, Optical Engineering, 56 (2017), pp. 1 – 20.

[42] S. Cardoso, P. P. Freitas, C. de Jesus, P. Wei, and J. C. Soares, *Spin-tunnel-junction thermal stability and interface interdiffusion above 300°c*, Applied Physics Letters, 76 (2000), pp. 610–612.

[43] C. Chappert, A. Fert, and F. N. Van Dau, *The emergence of spin electronics in data storage*, Nature Materials, 6 (2007), pp. 813–823.

[44] P. Che, K. Baumgaertl, A. Kukol'ova, C. Dubs, and D. Grundler, *Efficient wavelength conversion of exchange magnons below 100 nm by magnetic coplanar waveguides*, Nat Commun, 11 (2020), p. 1445.

[45] A. L. Chekhov, Y. Behovits, J. J. F. Heitz, C. Denker, D. A. Reiss, M. Wolf, M. Weinelt, P. W. Brouwer, M. Münzenberg, and T. Kampfrath, *Ultrafast demagnetization of iron induced by optical versus terahertz pulses*, Physical Review X, 11 (2021), p. 041055.

[46] M. Chen, R. Mishra, Y. Wu, K. Lee, and H. Yang, *Terahertz emission from compensated magnetic heterostructures*, Advanced Optical Materials, 6 (2018).

[47] Q. Chen and X. C. Zhang, *Polarization modulation in optoelectronic generation and detection of terahertz beams*, Applied Physics Letters, 74 (1999), pp. 3435–3437.

[48] X. Chen, X. Wu, S. Shan, F. Guo, D. Kong, C. Wang, T. Nie, C. Pandey, L. Wen, W. Zhao, C. Ruan, J. Miao, Y. Li, and L. Wang, *Generation and manipulation of chiral broadband terahertz waves from cascade spintronic terahertz emitters*, Applied Physics Letters, 115 (2019).

[49] L. Cheng, Z. Li, D. Zhao, and E. E. M. Chia, *Studying spin–charge conversion using terahertz pulses*, APL Materials, 9 (2021).

[50] L. Cheng, X. Wang, W. Yang, J. Chai, M. Yang, M. Chen, Y. Wu, X. Chen, D. Chi, K. E. J. Goh, J.-X. Zhu, H. Sun, S. Wang, J. C. W. Song, M. Battiato, H. Yang, and E. E. M. Chia, *Far out-of-equilibrium spin populations trigger giant spin injection into atomically thin mos2*, Nature Physics, 15 (2019), pp. 347–351.

[51] R. Cheng, M. W. Daniels, and J. G. Z. andD. Xiao, *Antiferromagnetic spin wave field-effect transistor*, Scientific Reports, 6 (2016).

[52] V. Cherepanov, I. Kolokolov, and V. L'Vov, *The saga of yig: Spectra, thermodynamics, interaction and relaxation of magnons in a complex magnet*, Physics Reports, 229 (1993), pp. 81–144.

[53] G.-M. Choi, B.-C. Min, K.-J. Lee, and D. G. Cahill, *Spin current generated by thermally driven ultrafast demagnetization*, Nature Communications, 5 (2014), pp. 4334–4334.

[54] E. M. Chudnovsky, *Theory of spin hall effect: extension of the drude model*, Phys Rev Lett, 99 (2007), p. 206601. Chudnovsky, Eugene M eng Phys Rev Lett. 2007 Nov 16;99(20):206601. doi: 10.1103/PhysRevLett.99.206601. Epub 2007 Nov 14.

[55] A. V. Chumak, V. I. Vasyuchka, A. A. Serga, and B. Hillebrands, *Magnon spintronics*, Nature Physics, 11 (2015), pp. 453–461.

[56] T. L. Cocker, D. Peller, P. Yu, J. Repp, and R. Huber, *Tracking the ultrafast motion of a single molecule by femtosecond orbital imaging*, Nature, 539 (2016), pp. 263–267.

[57] J. M. D. Coey, *Magnetism and Magnetic Materials*, Cambridge University Press, 2010.

[58] R. M. Cornell and U. Schwertmann, *The Iron Oxides: Structure, Properties, Reactions, Occurrences and Uses*, Wiley-VCH, Weinheim, 2nd ed., 2003.

[59] J. Cramer, T. Seifert, A. Kronenberg, F. Fuhrmann, G. Jakob, M. Jourdan, T. Kampfrath, and M. Klaui, *Complex terahertz and direct current inverse spin hall effect in yig/cu1-xirx bilayers across a wide concentration range*, Nano Lett, 18 (2018), pp. 1064–1069.

[60] F. D. Czeschka, L. Dreher, M. S. Brandt, M. Weiler, M. Althammer, I. M. Imort, G. Reiss, A. Thomas, W. Schoch, W. Limmer, H. Huebl, R. Gross, and S. T. Goennenwein, *Scaling behavior of the spin pumping effect in ferromagnet-platinum bilayers*, Phys Rev Lett, 107 (2011), p. 046601.

[61] H. Danan, A. Herr, and A. J. P. Meyer, *New determinations of the saturation magnetization of nickel and iron*, Journal of Applied Physics, 39 (1968), pp. 669–670.

[62] T. H. Dang, Q. Barbedienne, D. Q. To, E. Rongione, N. Reyren, F. Godel, S. Collin, J. M. George, and H. Jaffrès, *Anomalous hall effect in 3d/5d multilayers mediated by interface scattering and nonlocal spin conductivity*, Physical Review B, 102 (2020).

[63] T. H. Dang, J. Hawecker, E. Rongione, G. Baez Flores, D. Q. To, J. C. Rojas-Sanchez, H. Nong, J. Mangeney, J. Tignon, F. Godel, S. Collin, P. Seneor, M. Bibes, A. Fert, M. Anane, J. M. George, L. Vila, M. Cosset-Cheneau, D. Dolfi, R. Lebrun, P. Bortolotti, K. Belashchenko, S. Dhillon, and H. Jaffrès, *Ultrafast spin-currents and charge conversion at 3d-5d interfaces probed by time-domain terahertz spectroscopy*, Applied Physics Reviews, 7 (2020).

[64] W. P. Davey, *Precision measurements of the lattice constants of twelve common metals*, Physical Review, 25 (1925), pp. 753–761.

[65] A. V. Davydenko, A. G. Kozlov, A. G. Kolesnikov, M. E. Stebliy, G. S. Suslin, Y. E. Vekovshinin, A. V. Sadovnikov, and S. A. Nikitov, *Dzyaloshinskii-moriya interaction in symmetric epitaxial [co/pd(111)]n superlattices with different numbers of co/pd bilayers*, Physical Review B, 99 (2019).

[66] W. Demtröder, *Experimentalphysik 2 - Elektrizität und Optik*, Springer, 2013.

[67] S. L. Dexheimer, *Terahertz Spectroscopy: Principles and Applications*, CRC Press, 2017.

[68] S. S. Dhillon, M. S. Vitiello, E. H. Linfield, A. G. Davies, M. C. Hoffmann, J. Booske, C. Paoloni, M. Gensch, P. Weightman, G. P. Williams, E. Castro-Camus, D. R. S. Cumming, F. Simoens, I. Escorcia-Carranza, J. Grant, S. Lucyszyn, M. Kuwata-Gonokami, K. Konishi, M. Koch, C. A. Schmuttenmaer, T. L. Cocker, R. Huber, A. G. Markelz, Z. D. Taylor, V. P. Wallace, J. Axel Zeitler, J. Sibik, T. M. Korter, B. Ellison, S. Rea, P. Goldsmith, K. B. Cooper, R. Appleby, D. Pardo, P. G. Huggard, V. Krozer, H. Shams, M. Fice, C. Renaud, A. Seeds, A. Stöhr, M. Naftaly, N. Ridler, R. Clarke, J. E. Cunningham, and M. B. Johnston, *The 2017 terahertz science and technology roadmap*, Journal of Physics D: Applied Physics, 50 (2017), p. 043001.

[69] B.-W. Dong, L. Baldrati, C. Schneider, T. Niizeki, R. Ramos, A. Ross, J. Cramer, E. Saitoh, and M. Kläui, *Antiferromagnetic nio thickness dependent sign of the spin hall magnetoresistance in γ-fe₂o₃/nio/pt epitaxial stacks*, Applied Physics Letters, 114 (2019).

[70] R. L. DOUGLASS, *Spin-wave spectrum of yttrium iron garnet*, Physical Review, 120 (1960), pp. 1612–1614.

[71] M. DRESSEL AND G. GRÜNER, *Electrodynamics of Solids: Optical Properties of Electrons in Matter*, Cambridge University Press, 2002.

[72] M. DRESSEL AND M. SCHEFFLER, *Verifying the drude response*, Ann. Phys., 15 (2006).

[73] B. J. DROUIN, S. YU, J. C. PEARSON, AND H. GUPTA, *Terahertz spectroscopy for space applications: 2.5–2.7thz spectra of hd, h2o and nh3*, Journal of Molecular Structure, 1006 (2011), pp. 2–12.

[74] H. ELAYAN, O. AMIN, R. M. SHUBAIR, AND M.-S. ALOUINI, *Terahertz communication: The opportunities of wireless technology beyond 5g*, in 2018 International Conference on Advanced Communication Technologies and Networking (CommNet), IEEE, 2018, pp. 1–5.

[75] R. F. L. EVANS, W. J. FAN, P. CHUREEMART, T. A. OSTLER, M. O. A. ELLIS, AND R. W. CHANTRELL, *Atomistic spin model simulations of magnetic nanomaterials*, Journal of Physics: Condensed Matter, 26 (2014), p. 103202.

[76] J. FABIAN AND S. D. SARMA, *Spin relaxation of conduction electrons*, Journal of Vacuum Science & Technology B: Microelectronics and Nanometer Structures, 17 (1999).

[77] Z. FENG, H. QIU, D. WANG, C. ZHANG, S. SUN, B. JIN, AND W. TAN, *Spintronic terahertz emitter*, Journal of Applied Physics, 129 (2021).

[78] M. E. FERMANN, A. GALVANAUSKAS, AND G. SUCHA, *Ultrafast lasers: Technology and applications*, CRC Press, 2002.

[79] J. P. FERROLINO, N. I. CABELLO, A. DE LOS REYES, H. BARDOLAZA, I. C. VERONA, V. K. MAG-USARA, J. P. AFALLA, M. TALARA, H. KITAHARA, W. GARCIA, A. SOMINTAC, A. SALVADOR, M. TANI, AND E. ESTACIO, *Thickness dependence of the spintronic terahertz emission from ni/pt bilayer grown on mgo via electron beam deposition*, Applied Physics Express, 14 (2021), p. 093001.

[80] A. FERT, P. GRÜNBERG, A. BARTHÉLÉMY, F. PETROFF, AND W. ZINN, *Layered magnetic structures: interlayer exchange coupling and giant magnetoresistance*, Journal of Magnetism and Magnetic Materials, 140-144 (1995), pp. 1–8. International Conference on Magnetism.

[81] A. FERT AND P. M. LEVY, *Spin hall effect induced by resonant scattering on impurities in metals*, Phys Rev Lett, 106 (2011), p. 157208.

[82] M. Fix, R. Schneider, J. Bensmann, S. Michaelis de Vasconcellos, R. Bratschitsch, and M. Albrecht, *Thermomagnetic control of spintronic thz emission enabled by ferrimagnets*, Applied Physics Letters, 116 (2020).

[83] M. Fix, R. Schneider, S. Michaelis de Vasconcellos, R. Bratschitsch, and M. Albrecht, *Spin valves as magnetically switchable spintronic thz emitters*, Applied Physics Letters, 117 (2020).

[84] J. A. Fülöp, S. Tzortzakis, and T. Kampfrath, *Laser-driven strong-field terahertz sources*, Advanced Optical Materials, 8 (2019).

[85] A. Fognini, T. U. Michlmayr, A. Vaterlaus, and Y. Acremann, *Laser-induced ultrafast spin current pulses: a thermodynamic approach*, Journal of Physics: Condensed Matter, 29 (2017), p. 214002.

[86] M. Fonin, Y. S. Dedkov, R. Pentcheva, U. Rüdiger, and G. Güntherodt, *Magnetite: A search for the half-metallic state*, Journal of Physics Condensed Matter, 19 (2007), p. 315217.

[87] L. Frangou, S. Oyarzun, S. Auffret, L. Vila, S. Gambarelli, and V. Baltz, *Enhanced spin pumping efficiency in antiferromagnetic irmn thin films around the magnetic phase transition*, Phys Rev Lett, 116 (2016), p. 077203. Frangou, L Oyarzun, S Auffret, S Vila, L Gambarelli, S Baltz, V eng Phys Rev Lett. 2016 Feb 19;116(7):077203. doi: 10.1103/PhysRevLett.116.077203. Epub 2016 Feb 17.

[88] B. D. Fulthorpe, T. P. A. Hase, B. K. Tanner, C. H. Marrows, and B. J. Hickey, *Structural and magnetic changes on annealing permalloy/copper multilayers*, Journal of Magnetism and Magnetic Materials, 226-230 (2001), pp. 1733–1734.

[89] S. Geprags, A. Kehlberger, F. D. Coletta, Z. Qiu, E. J. Guo, T. Schulz, C. Mix, S. Meyer, A. Kamra, M. Althammer, H. Huebl, G. Jakob, Y. Ohnuma, H. Adachi, J. Barker, S. Maekawa, G. E. W. Bauer, E. Saitoh, R. Gross, S. T. B. Goennenwein, and M. Klaui, *Origin of the spin seebeck effect in compensated ferrimagnets*, Nat Commun, 7 (2016), p. 10452.

[90] T. Gilbert, *A phenomenological theory of damping in ferromagnetic materials*, IEEE Transactions on Magnetics, 40 (2004), pp. 3443–3449.

[91] O. Gladii, L. Frangou, G. Forestier, R. L. Seeger, S. Auffret, I. Joumard, M. Rubio-Roy, S. Gambarelli, and V. Baltz, *Unraveling the influence of electronic and magnonic spin-current injection near the magnetic ordering transition of irmn metallic antiferromagnets*, Physical Review B, 98 (2018).

[92] O. Gladii, L. Frangou, A. Hallal, R. L. Seeger, P. Noël, G. Forestier, S. Auffret, M. Rubio-Roy, P. Warin, L. Vila, S. Wimmer, H. Ebert,

S. Gambarelli, M. Chshiev, and V. Baltz, *Self-induced inverse spin hall effect in ferromagnets: Demonstration through nonmonotonic temperature dependence in permalloy*, Physical Review B, 100 (2019).

[93] R. E. Glover and M. Tinkham, *Conductivity of superconducting films for photon energies between 0.3 and $40kT_c$*, Phys. Rev., 108 (1957), pp. 243–256.

[94] O. Gomonay, T. Jungwirth, and J. Sinova, *High antiferromagnetic domain wall velocity induced by neel spin-orbit torques*, Phys Rev Lett, 117 (2016), p. 017202. Gomonay, O Jungwirth, T Sinova, J eng Phys Rev Lett. 2016 Jul 1;117(1):017202. doi: 10.1103/PhysRevLett.117.017202. Epub 2016 Jun 29.

[95] C. Goss, *Saturation magnetisation, coercivity and lattice parameter changes in the system fe304-gf2o3, and their relationship to structure*, Phys Chem Minerals, 16 (1988), pp. 164–171.

[96] M. Gradhand, M. Czerner, D. V. Fedorov, P. Zahn, B. Y. Yavorsky, L. Szunyogh, and I. Mertig, *Spin polarization on fermi surfaces of metals by the kkr method*, Physical Review B, 80 (2009).

[97] M. Gradhand, D. V. Fedorov, P. Zahn, and I. Mertig, *Extrinsic spin hall effect from first principles*, Phys Rev Lett, 104 (2010), p. 186403.

[98] O. Gueckstock, *Characterizing spintronic materials by terahertz spectroscopy*, Master's thesis, Technische Universität Berlin, Berlin, 2018.

[99] O. Gueckstock, L. Nadvornik, M. Gradhand, T. S. Seifert, G. Bierhance, R. Rouzegar, M. Wolf, M. Vafaee, J. Cramer, M. A. Syskaki, G. Woltersdorf, I. Mertig, G. Jakob, M. Klaui, and T. Kampfrath, *Terahertz spin-to-charge conversion by interfacial skew scattering in metallic bilayers*, Adv Mater, 33 (2021), p. e2006281.

[100] O. Gueckstock, L. Nádvorník, T. S. Seifert, M. Borchert, G. Jakob, G. Schmidt, G. Woltersdorf, M. Kläui, M. Wolf, and T. Kampfrath, *Modulating the polarization of broadband terahertz pulses from a spintronic emitter at rates up to 10 khz*, Optica, 8 (2021).

[101] O. Gueckstock, R. L. Seeger, T. S. Seifert, S. Auffret, S. Gambarelli, J. N. Kirchhof, K. I. Bolotin, V. Baltz, T. Kampfrath, and L. Nádvorník, *Impact of gigahertz and terahertz transport regimes on spin propagation and conversion in the antiferromagnet irmn*, Applied Physics Letters, 120 (2022).

[102] R. Gupta, S. Husain, A. Kumar, R. Brucas, A. Rydberg, and P. Svedlindh, *Co2feal full heusler compound based spintronic terahertz emitter*, Advanced Optical Materials, 9 (2021).

[103] P. Y. Han and X. C. Zhang, *Free-space coherent broadband terahertz time-domain spectroscopy*, Measurement Science and Technology, 12 (2001), pp. 1747–1756.

[104] W. Han, Y. Otani, and S. Maekawa, *Quantum materials for spin and charge conversion*, npj Quantum Materials, 3 (2018).

[105] T. Harter, C. Füllner, J. N. Kemal, S. Ummethala, J. L. Steinmann, M. Brosi, J. L. Hesler, E. Bründermann, A. S. Müller, W. Freude, S. Randel, and C. Koos, *Generalized kramers–kronig receiver for coherent terahertz communications*, Nature Photonics, 14 (2020), pp. 601–606.

[106] S. G. Hassan and E. J. Mohammad, *Study of the skin depth in different metallic atoms*, Materials Today: Proceedings, 42 (2021), pp. 2749–2751. 3rd International Conference on Materials Engineering & Science.

[107] J. Hawecker, T. Dang, E. Rongione, J. Boust, S. Collin, J. George, H. Drouhin, Y. Laplace, R. Grasset, J. Dong, J. Mangeney, J. Tignon, H. Jaffrès, L. Perfetti, and S. Dhillon, *Spin injection efficiency at metallic interfaces probed by thz emission spectroscopy*, Advanced Optical Materials, 9 (2021).

[108] S. Heidtfeld, R. Adam, T. Kubota, K. Takanashi, D. Cao, C. Schmitz-Antoniak, D. E. Bürgler, F. Wang, C. Greb, G. Chen, I. Komissarov, H. Hardtdegen, M. Mikulics, R. Sobolewski, S. Suga, and C. M. Schneider, *Generation of terahertz transients from co2fe0.4mn0.6si-heusler-alloy/normal-metal nanobilayers excited by femtosecond optical pulses*, Physical Review Research, 3 (2021), p. 043025.

[109] J. J. F. Heitz, L. Nádvorník, V. Balos, Y. Behovits, A. L. Chekhov, T. S. Seifert, K. Olejník, Z. Kašpar, K. Geishendorf, V. Novák, R. P. Campion, M. Wolf, T. Jungwirth, and T. Kampfrath, *Optically gated terahertz-field-driven switching of antiferromagnetic cumnas*, Physical Review Applied, 16 (2021).

[110] T. Helgaker, S. Coriani, P. Jørgensen, K. Kristensen, J. Olsen, and K. Ruud, *Recent advances in wave function-based methods of molecular-property calculations*, Chemical Reviews, 112 (2012), pp. 543–631.

[111] R. I. Herapath, S. M. Hornett, T. S. Seifert, G. Jakob, M. Kläui, J. Bertolotti, T. Kampfrath, and E. Hendry, *Impact of pump wavelength on terahertz emission of a cavity-enhanced spintronic trilayer*, Applied Physics Letters, 114 (2019).

[112] C. Herschbach, D. V. Fedorov, I. Mertig, M. Gradhand, K. Chadova, H. Ebert, and D. Ködderitzsch, *Insight into the skew-scattering mechanism of*

the spin hall effect: Potential scattering versus spin-orbit scattering, Physical Review B, 88 (2013).

[113] Y. HIROTA, R. HATTORI, M. TANI, AND M. HANGYO, *Polarization modulation of terahertz electromagnetic radiation by four-contact photoconductive antenna*, Optics Express, 14 (2006), pp. 4486–4493.

[114] A. HOFFMANN, *Pure spin-currents*, physica status solidi (c), 4 (2007), pp. 4236–4241.

[115] E. HOFMEISTER, A. M. KEPPEL AND A. K. SPECK, *Absorption and reflection infrared spectra of mgo and other diatomic compounds*, Mon. Not. R. Astron. Soc., 345 (2003), pp. 16–38.

[116] C. HOLZMANN, A. ULLRICH, O.-T. CIUBOTARIU, AND M. ALBRECHT, *Stress-induced magnetic properties of gadolinium iron garnet nanoscale-thin films: Implications for spintronic devices*, ACS Applied Nano Materials, 5 (2022), pp. 1023–1033.

[117] W. HOPPE, J. WEBER, S. TIRPANCI, O. GUECKSTOCK, T. KAMPFRATH, AND G. WOLTERSDORF, *On-chip generation of ultrafast current pulses by nanolayered spintronic terahertz emitters*, ACS Applied Nano Materials, 4 (2021), pp. 7454–7460.

[118] H.-W. HUBERS, *Terahertz heterodyne receivers*, IEEE Journal of Selected Topics in Quantum Electronics, 14 (2008), pp. 378–391.

[119] M. HUDL, M. D'AQUINO, M. PANCALDI, S. H. YANG, M. G. SAMANT, S. S. P. PARKIN, H. A. DURR, C. SERPICO, M. C. HOFFMANN, AND S. BONETTI, *Nonlinear magnetization dynamics driven by strong terahertz fields*, Phys Rev Lett, 123 (2019), p. 197204.

[120] T. J. HUISMAN, C. CICCARELLI, A. TSUKAMOTO, R. V. MIKHAYLOVSKIY, T. RASING, AND A. V. KIMEL, *Spin-photo-currents generated by femtosecond laser pulses in a ferrimagnetic gdfeco/pt bilayer*, Applied Physics Letters, 110 (2017).

[121] T. J. HUISMAN, R. V. MIKHAYLOVSKIY, J. D. COSTA, F. FREIMUTH, E. PAZ, J. VENTURA, P. P. FREITAS, S. BLUGEL, Y. MOKROUSOV, T. RASING, AND A. V. KIMEL, *Femtosecond control of electric currents in metallic ferromagnetic heterostructures*, Nat Nanotechnol, 11 (2016), pp. 455–8.

[122] T. J. HUISMAN, R. V. MIKHAYLOVSKIY, A. TSUKAMOTO, T. RASING, AND A. V. KIMEL, *Simultaneous measurements of terahertz emission and magneto-optical kerr effect for resolving ultrafast laser-induced demagnetization dynamics*, Physical Review B, 92 (2015), p. 104419.

[123] H. Y. HWANG, S. FLEISCHER, N. C. BRANDT, B. G. PERKINS, M. LIU, K. FAN, A. STERNBACH, X. ZHANG, R. D. AVERITT, AND K. A. NELSON, *A review of non-*

linear terahertz spectroscopy with ultrashort tabletop-laser pulses, Journal of Modern Optics, 62 (2015), pp. 1447–1479.

[124] S. INGVARSSON, L. RITCHIE, X. Y. LIU, G. XIAO, J. C. SLONCZEWSKI, P. L. TROUILLOUD, AND R. H. KOCH, *Role of electron scattering in the magnetization relaxation of thinni81fe19films*, Physical Review B, 66 (2002).

[125] M. JAMALI, Y. LV, Z. ZHAO, AND J.-P. WANG, *Sputtering of cobalt film with perpendicular magnetic anisotropy on disorder-free graphene*, AIP Advances, 4 (2014).

[126] C. M. JAWORSKI, J. YANG, S. MACK, D. D. AWSCHALOM, J. P. HEREMANS, AND R. C. MYERS, *Observation of the spin-seebeck effect in a ferromagnetic semiconductor*, Nat Mater, 9 (2010), pp. 898–903.

[127] H. T. JENG, G. Y. GUO, AND D. J. HUANG, *Charge-orbital ordering and verwey transition in magnetite*, Physical Review Letters, 93 (2004), pp. 156403–156403.

[128] S. JENKINS, R. W. CHANTRELL, AND R. F. L. EVANS, *Spin wave excitations in exchange biased irmn/cofe bilayers*, Journal of Applied Physics, 128 (2020).

[129] X. JIA, K. LIU, K. XIA, AND G. E. W. BAUER, *Spin transfer torque on magnetic insulators*, EPL (Europhysics Letters), 96 (2011).

[130] D. C. JILES, *Frequency dependence of hysteresis curves in conducting magnetic materials*, Journal of Applied Physics, 76 (1994), pp. 5849–5855.

[131] P. JIMÉNEZ-CAVERO, O. GUECKSTOCK, L. NÁDVORNÍK, I. LUCAS, T. S. SEIFERT, M. WOLF, R. ROUZEGAR, P. W. BROUWER, S. BECKER, G. JAKOB, M. KLÄUI, C. GUO, C. WAN, X. HAN, Z. JIN, H. ZHAO, D. WU, L. MORELLÓN, AND T. KAMPFRATH, *Transition of laser-induced terahertz spin currents from torque- to conduction-electron-mediated transport*, Phys. Rev. B, 105 (2022), p. 184408.

[132] P. JIMÉNEZ-CAVERO, I. LUCAS, A. ANADÓN, R. RAMOS, T. NIIZEKI, M. H. AGUIRRE, P. A. ALGARABEL, K. UCHIDA, M. R. IBARRA, E. SAITOH, AND L. MORELLÓN, *Spin seebeck effect in insulating epitaxial γ-fe$_2$o$_3$ thin films*, APL Materials, 5 (2017), p. 026103.

[133] M. JULLIERE, *Tunneling between ferromagnetic films*, Physics Letters A, 54 (1975), pp. 225–226.

[134] S. JUNG, H. LEE, S. MYUNG, H. KIM, S. K. YOON, S. W. KWON, Y. JU, M. KIM, W. YI, S. HAN, B. KWON, B. SEO, K. LEE, G. H. KOH, K. LEE, Y. SONG, C. CHOI, D. HAM, AND S. J. KIM, *A crossbar array of magnetoresistive memory devices for in-memory computing*, Nature, 601 (2022), pp. 211–216.

[135] M. B. Jungfleisch, Q. Zhang, W. Zhang, J. E. Pearson, R. D. Schaller, H. Wen, and A. Hoffmann, *Control of terahertz emission by ultrafast spin-charge current conversion at rashba interfaces*, Phys Rev Lett, 120 (2018), p. 207207.

[136] T. Jungwirth, X. Marti, P. Wadley, and J. Wunderlich, *Antiferromagnetic spintronics*, Nat Nanotechnol, 11 (2016), pp. 231–41. Jungwirth, T Marti, X Wadley, P Wunderlich, J eng Research Support, Non-U.S. Gov't Review England Nat Nanotechnol. 2016 Mar;11(3):231-41. doi: 10.1038/nnano.2016.18.

[137] T. Kampfrath, *Charge-Carrier Dynamics in Solids and Gases Observed by Time-Resolved Terahertz Spectroscopy*, PhD thesis, 2006.

[138] T. Kampfrath, M. Battiato, P. Maldonado, G. Eilers, J. Notzold, S. Mahrlein, V. Zbarsky, F. Freimuth, Y. Mokrousov, S. Blugel, M. Wolf, I. Radu, P. M. Oppeneer, and M. Munzenberg, *Terahertz spin current pulses controlled by magnetic heterostructures*, Nat Nanotechnol, 8 (2013), pp. 256–60.

[139] T. Kampfrath, J. Nötzold, and M. Wolf, *Sampling of broadband terahertz pulses with thick electro-optic crystals*, Applied Physics Letters, 90 (2007).

[140] T. Kampfrath, R. G. Ulbrich, F. Leuenberger, M. Münzenberg, B. Sass, and W. Felsch, *Ultrafast magneto-optical response of iron thin films*, Physical Review B, 65 (2002).

[141] A. Kamra, T. Wimmer, H. Huebl, and M. Althammer, *Antiferromagnetic magnon pseudospin: Dynamics and diffusive transport*, Physical Review B, 102 (2020).

[142] R. Karplus and J. M. Luttinger, *Hall effect in ferromagnetics*, Physical Review, 95 (1954), pp. 1154–1160.

[143] F. N. Kholid, D. Hamara, M. Terschanski, F. Mertens, D. Bossini, M. Cinchetti, L. McKenzie-Sell, J. Patchett, D. Petit, R. Cowburn, J. Robinson, J. Barker, and C. Ciccarelli, *Temperature dependence of the picosecond spin seebeck effect*, Applied Physics Letters, 119 (2021).

[144] S.-M. Kim, K.-H. Kim, and M.-J. Keum, *Deposition of an al cathode for an oled by using low-damage sputtering method*, Journal of the Korean Physical Society, 51 (2007), pp. 1023–1026.

[145] J. Kimling, G. M. Choi, J. T. Brangham, T. Matalla-Wagner, T. Huebner, T. Kuschel, F. Yang, and D. G. Cahill, *Picosecond spin seebeck effect*, Physical Review Letters, 118 (2017), p. 057201.

[146] C. Kittel, *Introduction to solid state physics*, Wiley, 2005.

[147] T. Kürner and S. Priebe, *Towards thz communications - status in research, standardization and regulation*, Journal of Infrared, Millimeter, and Terahertz Waves, 35 (2013), pp. 53–62.

[148] R. Kubo, *Statistical-mechanical theory of irreversible processes. i. general theory and simple applications to magnetic and conduction problems*, Journal of the Physical Society of Japan, 12 (1957), pp. 570–586.

[149] S. Kumar, A. Nivedan, A. Singh, Y. Kumar, P. Malhotra, M. Tondusson, E. Freysz, and S. Kumar, *Optical damage limit of efficient spintronic thz emitters*, iScience, 24 (2021), p. 103152.

[150] K. T. Y. Kung, L. K. Louie, and G. L. Gorman, *Mnfe structure-exchange anisotropy relation in the nife/mnfe/nife system*, Journal of Applied Physics, 69 (1991), pp. 5634–5636.

[151] K. Lal and H. K. Jhans, *The dielectric constant of gadolinium gallium garnet and α -al$_2$o$_3$ single crystals*, Journal of Physics C: Solid State Physics, 10 (1977), pp. 1315–1319.

[152] M. L. M. Lalieu, R. Lavrijsen, R. A. Duine, and B. Koopmans, *Investigating optically excited terahertz standing spin waves using noncollinear magnetic bilayers*, Physical Review B, 99 (2019), p. 184439.

[153] M. Laska and E. Dudkiewicz, *Research of co2concentration in naturally ventilated lecture room*, E3S Web of Conferences, 22 (2017).

[154] J.-S. Lee, Y.-J. Song, H.-S. Hsu, C.-R. Lin, J.-Y. Huang, and J. Chen, *Magnetic enhancement of carbon-encapsulated magnetite nanoparticles*, Journal of Alloys and Compounds, 790 (2019), pp. 716–722.

[155] A. Leitenstorfer, S. Hunsche, J. Shah, M. C. Nuss, and W. H. Knox, *Detectors and sources for ultrabroadband electro-optic sampling: Experiment and theory*, Applied Physics Letters, 74 (1999), pp. 1516–1518.

[156] M. Lezius, T. Wilken, C. Deutsch, M. Giunta, O. Mandel, A. Thaller, V. Schkolnik, M. Schiemangk, A. Dinkelaker, A. Kohfeldt, A. Wicht, M. Krutzik, A. Peters, O. Hellmig, H. Duncker, K. Sengstock, P. Windpassinger, K. Lampmann, T. Hülsing, T. W. Hänsch, and R. Holzwarth, *Space-borne frequency comb metrology*, Optica, 3 (2016), pp. 1381–1387.

[157] C. Li, B. Fang, L. Zhang, Q. Chen, X. Xie, N. Xu, Z. Zeng, Z. Wang, L. Fang, and T. Jiang, *Terahertz generation via picosecond spin-to-charge conversion in irmn3/ni-fe heterojunction*, Physical Review Applied, 16 (2021).

[158] G. Li, R. Medapalli, R. V. Mikhaylovskiy, F. E. Spada, T. Rasing, E. E. Fullerton, and A. V. Kimel, *Thz emission from co/pt bilayers with varied roughness, crystal structure, and interface intermixing*, Physical Review Materials, 3 (2019).

[159] G. Li, R. V. Mikhaylovskiy, K. A. Grishunin, J. D. Costa, T. Rasing, and A. V. Kimel, *Laser induced thz emission from femtosecond photocurrents in co/zno/pt and co/cu/pt multilayers*, Journal of Physics D: Applied Physics, 51 (2018).

[160] J. Li, C. B. Wilson, R. Cheng, M. Lohmann, M. Kavand, W. Yuan, M. Aldosary, N. Agladze, P. Wei, M. S. Sherwin, and J. Shi, *Spin current from sub-terahertz-generated antiferromagnetic magnons*, Nature, 578 (2020), pp. 70–74.

[161] T. Lichtenberg, M. Beens, M. H. Jansen, B. Koopmans, and R. A. Duine, *Probing optically induced spin currents using terahertz spin waves in noncollinear magnetic bilayers*, Physical Review B, 105 (2022), p. 144416.

[162] V. Linss, M. Bivour, H. Iwata, and K. Ortner, *Comparison of low damage sputter deposition techniques to enable the application of very thin a-si passivation films*, 2019.

[163] C. Q. Liu, W. T. Lu, Z. X. Wei, Y. F. Miao, P. Wang, H. Xia, Y. P. Liu, F. L. Zeng, J. R. Zhang, C. Zhou, H. B. Zhao, Y. Z. Wu, Z. Yuan, and J. Qi, *Strain-induced anisotropic terahertz emission from a fe(211)/pt(110) bilayer*, Physical Review Applied, 15 (2021), p. 044022.

[164] L. Liu, O. J. Lee, T. J. Gudmundsen, D. C. Ralph, and R. A. Buhrman, *Current-induced switching of perpendicularly magnetized magnetic layers using spin torque from the spin hall effect*, Phys Rev Lett, 109 (2012), p. 096602.

[165] Y. Liu, H. Cheng, Y. Xu, P. Vallobra, S. Eimer, X. Zhang, X. Wu, T. Nie, and W. Zhao, *Separation of emission mechanisms in spintronic terahertz emitters*, Physical Review B, 104 (2021), p. 064419.

[166] G. M. Luo, Z. H. Mai, T. P. A. Hase, B. D. Fulthorpe, B. K. Tanner, C. H. Marrows, and B. J. Hickey, *Variable wavelength grazing incidence x-ray reflectivity measurements of structural changes on annealingcu/nifemultilayers*, Physical Review B, 64 (2001).

[167] S. Maehrlein, A. Paarmann, M. Wolf, and T. Kampfrath, *Terahertz sum-frequency excitation of a raman-active phonon*, Phys Rev Lett, 119 (2017), p. 127402.

[168] S. F. Maehrlein, *Nonlinear Terahertz Phononics: A Novel Route to Controlling Matter*, PhD thesis, Freie Universität Berlin, Berlin, 2016.

[169] S. Maekawa, S. Valenzuela, E. Saitoh, and T. Kimura, *Spin Current*, Oxford Science Publications, Oxford University Press, 2015.

[170] S. Maekawa, S. O. Valenzuela, E. Saitoh, and T. Kimura, *Spin Current*, Oxford University Press, 09 2017.

[171] G. Malinowski, N. Bergeard, M. Hehn, and S. Mangin, *Hot-electron transport and ultrafast magnetization dynamics in magnetic multilayers and nanostructures following femtosecond laser pulse excitation*, The European Physical Journal B, 91 (2018).

[172] A. Manchon, J. Železný, I. M. Miron, T. Jungwirth, J. Sinova, A. Thiaville, K. Garello, and P. Gambardella, *Current-induced spin-orbit torques in ferromagnetic and antiferromagnetic systems*, Reviews of Modern Physics, 91 (2019).

[173] A. Manchon and S. Zhang, *Theory of spin torque due to spin-orbit coupling*, Phys. Rev. B, 79 (2009), p. 094422.

[174] P. E. Martin and E. F. Barker, *The infrared absorption spectrum of carbon dioxide*, Phys. Rev., 41 (1932), pp. 291–303.

[175] M. Matthiesen, D. Afanasiev, J. R. Hortensius, T. C. van Thiel, R. Medapalli, E. E. Fullerton, and A. D. Caviglia, *Temperature dependent inverse spin hall effect in co/pt spintronic emitters*, Applied Physics Letters, 116 (2020).

[176] K. Maussang, J. Palomo, J. Mangeney, S. S. Dhillon, and J. Tignon, *Large-area photoconductive switches as emitters of terahertz pulses with fully electrically controlled linear polarization*, Optics Express, 27 (2019), pp. 14784–14797.

[177] M. Meinert, B. Gliniors, O. Gueckstock, T. S. Seifert, L. Liensberger, M. Weiler, S. Wimmer, H. Ebert, and T. Kampfrath, *High-throughput techniques for measuring the spin hall effect*, Physical Review Applied, 14 (2020), p. 064011.

[178] M. Meinert, D. Graulich, and T. Matalla-Wagner, *Electrical switching of antiferromagnetic mn2au and the role of thermal activation*, Physical Review Applied, 9 (2018).

[179] P. Merodio, A. Ghosh, C. Lemonias, E. Gautier, U. Ebels, M. Chshiev, H. Béa, V. Baltz, and W. E. Bailey, *Penetration depth and absorption mechanisms of spin currents in ir20mn80 and fe50mn50 polycrystalline films by ferromagnetic resonance and spin pumping*, Applied Physics Letters, 104 (2014).

[180] B. F. Miao, S. Y. Huang, D. Qu, and C. L. Chien, *Inverse spin hall effect in a ferromagnetic metal*, Phys Rev Lett, 111 (2013), p. 066602.

[181] P. Mohn, *Magnetism in the solid state: an introduction*, Springer, 2006.

[182] R. Mondal, M. Berritta, and P. M. Oppeneer, *Relativistic theory of spin relaxation mechanisms in the landau-lifshitz-gilbert equation of spin dynamics*, Phys. Rev. B, 94 (2016), p. 144419.

[183] C. M. Morris, R. V. Aguilar, A. V. Stier, and N. P. Armitage, *Polarization modulation time-domain terahertz polarimetry*, Optics Express, 20 (2012), pp. 12303–12317.

[184] N. F. Mott, *The scattering of fast electrons by atomic nuclei*, Proceedings of the Royal Society A, 124 (1929), pp. 425–442.

[185] B. Y. Mueller and B. Rethfeld, *Thermodynamic μt model of ultrafast magnetization dynamics*, Physical Review B, 90 (2014), p. 144420.

[186] G. M. Muller, J. Walowski, M. Djordjevic, G. X. Miao, A. Gupta, A. V. Ramos, K. Gehrke, V. Moshnyaga, K. Samwer, J. Schmalhorst, A. Thomas, A. Hutten, G. Reiss, J. S. Moodera, and M. Munzenberg, *Spin polarization in half-metals probed by femtosecond spin excitation*, Nat Mater, 8 (2009), pp. 56–61.

[187] M. A. Musa, R. S. Azis, N. H. Osman, J. Hassan, and T. Zangina, *Structural and magnetic properties of yttrium iron garnet (yig) and yttrium aluminum iron garnet (yalg) nanoferrite via sol-gel synthesis*, Results in Physics, 7 (2017), pp. 1135–1142.

[188] A. R. Muxworthy and E. McClelland, *Review of the low-temperature magnetic properties of magnetite from a rock magnetic perspective*, Geophysical Journal International, 140 (2000), pp. 101–114.

[189] T. L. Myers, B. D. Cannon, C. S. Brauer, S. M. Hansen, and B. G. Crowther, *Proton and gamma irradiation of fabry-perot quantum cascade lasers for space qualification*, Appl. Opt., 54 (2015), pp. 527–534.

[190] N. Nagaosa, J. Sinova, S. Onoda, A. H. MacDonald, and N. P. Ong, *Anomalous hall effect*, Reviews of Modern Physics, 82 (2010), pp. 1539–1592.

[191] H. Nakayama, M. Althammer, Y.-T. Chen, K. Uchida, Y. Kajiwara, D. Kikuchi, T. Ohtani, S. Geprägs, M. Opel, S. Takahashi, R. Gross, G. E. W. Bauer, S. T. B. Goennenwein, and E. Saitoh, *Spin hall magnetoresistance induced by a nonequilibrium proximity effect*, Phys. Rev. Lett., 110 (2013), p. 206601.

[192] D. A. Naylor and M. K. Tahic, *Apodizing functions for fourier transform spectroscopy*, Journal of the Optical Society of America A, 24 (2007), pp. 3644–3648.

[193] L. Nádvorník, M. Borchert, L. Brandt, R. Schlitz, K. A. de Mare, K. Vyborny, I. Mertig, G. Jakob, M. Kläui, S. T. B. Goennenwein, M. Wolf, G. Woltersdorf, and T. Kampfrath, *Broadband terahertz probes of anisotropic magnetoresistance disentangle extrinsic and intrinsic contributions*, Physical Review X, 11 (2021), p. 021030.

[194] L. Nádvorník, O. Gueckstock, L. Braun, C. Niu, J. Gräfe, G. Richter, G. Schütz, H. Takagi, T. S. Seifert, P. Kubaščík, A. K. Pandeya, A. Anane, H. Yang, A. Bedoya-Pinto, S. S. P. Parkin, M. Wolf, Y. Mokrousov, H. Nakamura, and T. Kampfrath, *Terahertz spin-to-charge current conversion in stacks of ferromagnets and the transition-metal dichalcogenide nbse$_2$*, arXiv, 2208.00846 (2022).

[195] D. M. Nenno, R. Binder, and H. C. Schneider, *Simulation of hot-carrier dynamics and terahertz emission in laser-excited metallic bilayers*, Physical Review Applied, 11 (2019), p. 054083.

[196] D. M. Nenno, L. Scheuer, D. Sokoluk, S. Keller, G. Torosyan, A. Brodyanski, J. Losch, M. Battiato, M. Rahm, R. H. Binder, H. C. Schneider, R. Beigang, and E. T. Papaioannou, *Modification of spintronic terahertz emitter performance through defect engineering*, Sci Rep, 9 (2019), p. 13348.

[197] Y. Ni, Z. Jin, B. Song, X. Zhou, H. Chen, C. Song, Y. Peng, C. Zhang, F. Pan, G. Ma, Y. Zhu, and S. Zhuang, *Temperature-dependent terahertz emission from co/mn2au spintronic bilayers*, physica status solidi (RRL) – Rapid Research Letters, 15 (2021).

[198] J. Noh, O. I. Osman, S. G. Aziz, P. Winget, and J. L. Bredas, *A density functional theory investigation of the electronic structure and spin moments of magnetite*, Sci Technol Adv Mater, 15 (2014), p. 044202.

[199] W. Nolting and A. Ramakanth, *Quantum Theory of Magnetism*, Springer, 2009.

[200] M. Obstbaum, M. Härtinger, H. G. Bauer, T. Meier, F. Swientek, C. H. Back, and G. Woltersdorf, *Inverse spin hall effect inni81fe19/normal-metal bilayers*, Physical Review B, 89 (2014).

[201] Y. W. Oh, S. H. Chris Baek, Y. M. Kim, H. Y. Lee, K. D. Lee, C. G. Yang, E. S. Park, K. S. Lee, K. W. Kim, G. Go, J. R. Jeong, B. C. Min, H. W. Lee, K. J. Lee, and B. G. Park, *Field-free switching of perpendicular magnetization through spin-orbit torque in antiferromagnet/ferromagnet/oxide structures*, Nat Nanotechnol, 11 (2016), pp. 878–884.

[202] Y. Ohnuma, H. Adachi, E. Saitoh, and S. Maekawa, *Enhanced dc spin pumping into a fluctuating ferromagnet near tc*, Physical Review B, 89 (2014).

[203] K. OLEJNIK, V. SCHULER, X. MARTI, V. NOVAK, Z. KASPAR, P. WADLEY, R. P. CAMPION, K. W. EDMONDS, B. L. GALLAGHER, J. GARCES, M. BAUMGARTNER, P. GAMBARDELLA, AND T. JUNGWIRTH, *Antiferromagnetic cumnas multi-level memory cell with microelectronic compatibility*, Nat Commun, 8 (2017), p. 15434.

[204] K. OLEJNÍK, T. SEIFERT, Z. KAŠPAR, V. NOVÁK, P. WADLEY, R. P. CAMPION, M. BAUMGARTNER, P. GAMBARDELLA, P. NĚMEC, J. WUNDERLICH, J. SINOVA, P. KUŽEL, M. MÜLLER, T. KAMPFRATH, AND T. JUNGWIRTH, *Terahertz electrical writing speed in an antiferromagnetic memory*, Science Advances, 4 (2018).

[205] N. ONG AND W. LEE, *Geometry and the anomalous hall effect in ferromagnets*, Proceedings of the 8th International Symposium on Foundations of Quantum Mechanics in the Light of New Technology, ISQM-Tokyo 2005, World Scientific Publishing Co. Pte Ltd, 2006, pp. 121–126.

[206] P. M. OPPENEER, *Handbook of Magnetic Materials Vol. 13*, Elsevier, 2001, book Magneto-Optical Kerr Spectra.

[207] E. D. PALIK, *Handbook of Optical Constants of Solids*, Academic Press handbook series, Elsevier Science, 1998. v. 3.

[208] E. T. PAPAIOANNOU, G. TOROSYAN, S. KELLER, L. SCHEUER, M. BATTIATO, V. K. MAG-USARA, J. L'HUILLIER, M. TANI, AND R. BEIGANG, *Efficient terahertz generation using fe/pt spintronic emitters pumped at different wavelengths*, IEEE Transactions on Magnetics, 54 (2018), pp. 1–5.

[209] S. S. P. PARKIN, *Giant magnetoresistance in magnetic nanostructures*, Annual Review of Materials Science, 25 (1995), pp. 357–388.

[210] A. PASHKIN, A. SELL, T. KAMPFRATH, AND R. HUBER, *Electric and magnetic terahertz nonlinearities resolved on the sub-cycle scale*, New Journal of Physics, 15 (2013), p. 065003.

[211] K.-E. PEIPONEN, A. ZEITLER, AND M. KUWATA-GONOKAMI, *Terahertz spectroscopy and imaging*, Springer, 2012.

[212] L. PETERSEN AND P. HEDEGÅRD, *A simple tight-binding model of spin–orbit splitting of sp-derived surface states*, Surface Science, 459 (2000), pp. 49–56.

[213] A. K. PETFORD-LONG, M. B. STEARNS, C. H. CHANG, S. R. NUTT, D. G. STEARNS, N. M. CEGLIO, AND A. M. HAWRYLUK, *High-resolution electron microscopy study of x-ray multilayer structures*, Journal of Applied Physics, 61 (1987), pp. 1422–1428.

[214] T. K. H. PHAM, M. RIBEIRO, J. H. PARK, N. J. LEE, K. H. KANG, E. PARK, V. Q. NGUYEN, A. MICHEL, C. S. YOON, S. CHO, AND T. H. KIM, *Interface*

morphology effect on the spin mixing conductance of pt/fe3o4 bilayers, Sci Rep, 8 (2018), p. 13907.

[215] G. Prenat, K. Jabeur, G. D. Pendina, O. Boulle, and G. Gaudin, *Beyond STT-MRAM, spin orbit torque RAM SOT-MRAM for high speed and high reliability applications*, Springer, 2015.

[216] G. A. Prinz, *Spin-polarized transport*, Physics Today, 48 (1995), pp. 58–63.

[217] L. Qian, W. Chen, K. Wang, X. Wu, and G. Xiao, *Spin hall effect and current induced magnetic switching in antiferromagnetic irmn*, AIP Advances, 8 (2018).

[218] H. Qiu, L. Zhou, C. Zhang, J. Wu, Y. Tian, S. Cheng, S. Mi, H. Zhao, Q. Zhang, D. Wu, B. Jin, J. Chen, and P. Wu, *Ultrafast spin current generated from an antiferromagnet*, Nature Physics, 17 (2020), pp. 388–394.

[219] H. S. Qiu, K. Kato, K. Hirota, N. Sarukura, M. Yoshimura, and M. Naka-jima, *Layer thickness dependence of the terahertz emission based on spin current in ferromagnetic heterostructures*, Opt Express, 26 (2018), pp. 15247–15254.

[220] X. P. Qiu, Y. J. Shin, J. Niu, N. Kulothungasagaran, G. Kalon, C. Qiu, T. Yu, and H. Yang, *Disorder-free sputtering method on graphene*, AIP Advances, 2 (2012).

[221] Z. Qiu, K. Ando, K. Uchida, Y. Kajiwara, R. Takahashi, H. Nakayama, T. An, Y. Fujikawa, and E. Saitoh, *Spin mixing conductance at a well-controlled platinum/yttrium iron garnet interface*, Applied Physics Letters, 103 (2013).

[222] Z. Q. Qiu and S. D. Bader, *Surface magneto-optic kerr effect*, Review of Scientific Instruments, 71 (2000), pp. 1243–1255.

[223] M. R. Querry, *Optical constants*, Contractor Report, (1985), p. CRDC CR 85034.

[224] M. Rahm, J.-S. Li, and W. J. Padilla, *Thz wave modulators: A brief review on different modulation techniques*, Journal of Infrared, Millimeter, and Terahertz Waves, 34 (2012), pp. 1–27.

[225] R. Ramos, T. Kikkawa, A. Anadón, I. Lucas, T. Niizeki, K. Uchida, P. A. Algarabel, L. Morellón, M. H. Aguirre, M. R. Ibarra, and E. Saitoh, *Interface-induced anomalous nernst effect in fe3o4/pt-based heterostructures*, Applied Physics Letters, 114 (2019).

[226] R. Ramos, T. Kikkawa, K. Uchida, H. Adachi, I. Lucas, M. H. Aguirre, P. Algarabel, L. Morellón, S. Maekawa, E. Saitoh, and M. R. Ibarra, *Observation of the spin seebeck effect in epitaxial fe3o 4 thin films*, Applied Physics Letters, 102 (2013), pp. 7–12.

[227] I. Razdolski, A. Alekhin, N. Ilin, J. P. Meyburg, V. Roddatis, D. Diesing, U. Bovensiepen, and A. Melnikov, *Nanoscale interface confinement of ultrafast spin transfer torque driving non-uniform spin dynamics*, Nat Commun, 8 (2017), p. 15007.

[228] H. Reichlova, R. Lopes Seeger, R. Gonzalez-Hernandez, I. Kounta, R. Schlitz, D. Kriegner, P. Ritzinger, M. Lammel, M. Leiviska, V. Petricek, P. Dolezal, E. Schmoranzerova, A. in Badura, A. Thomas, V. Baltz, L. Michez, J. Sinova, S. T. B. Goennenwein, T. Jungwirth, and L. Smejkal, *Macroscopic time reversal symmetry breaking bystaggered spin-momentum interaction*, arXiv, 2012.15651 (2021).

[229] J. C. Rojas-Sanchez, N. Reyren, P. Laczkowski, W. Savero, J. P. Attane, C. Deranlot, M. Jamet, J. M. George, L. Vila, and H. Jaffres, *Spin pumping and inverse spin hall effect in platinum: the essential role of spin-memory loss at metallic interfaces*, Phys Rev Lett, 112 (2014), p. 106602.

[230] A. Rostami, H. Rasooli, and H. Baghban, Springer, Berlin, Heidelberg, 2011.

[231] R. Rouzegar, L. Brandt, L. Nadvornik, D. A. Reiss, A. L. Chekhov, O. Gueckstock, C. In, M. Wolf, T. S. Seifert, P. W. Brouwer, G. Woltersdorf, and T. Kampfrath, *Laser-induced terahertz spin transport in magnetic nanostructures arises from the same force as ultrafast demagnetization*, arXiv, 2103.11710 (2021).

[232] A. Rubano, L. Braun, M. Wolf, and T. Kampfrath, *Mid-infrared time-domain ellipsometry: Application to nb-doped srtio3*, Applied Physics Letters, 101 (2012).

[233] A. Rückriegel and P. Kopietz, *Spin currents, spin torques, and the concept of spin superfluidity*, Phys. Rev. B, 95 (2017), p. 104436.

[234] C. Rulliere, *Femtosecond Laser Pulses: Principles and Experiments*, Springer, second ed., 2003.

[235] H. Saglam, W. Zhang, M. B. Jungfleisch, J. Sklenar, J. E. Pearson, J. B. Ketterson, and A. Hoffmann, *Spin transport through the metallic antiferromagnet femn*, Physical Review B, 94 (2016), p. 140412(R).

[236] M. Sajadi, M. Wolf, and T. Kampfrath, *Transient birefringence of liquids induced by terahertz electric-field torque on permanent molecular dipoles*, Nat Commun, 8 (2017), p. 14963.

[237] J. C. Sanchez, L. Vila, G. Desfonds, S. Gambarelli, J. P. Attane, J. M. De Teresa, C. Magen, and A. Fert, *Spin-to-charge conversion using rashba*

coupling at the interface between non-magnetic materials, Nat Commun, 4 (2013), p. 2944.

[238] D. Sander, S. O. Valenzuela, D. Makarov, C. H. Marrows, E. E. Fullerton, P. Fischer, J. McCord, P. Vavassori, S. Mangin, P. Pirro, B. Hillebrands, A. D. Kent, T. Jungwirth, O. Gutfleisch, C. G. Kim, and A. Berger, *The 2017 magnetism roadmap*, Journal of Physics D: Applied Physics, 50 (2017), p. 363001.

[239] Y. Sasaki, G. Li, T. Moriyama, T. Ono, R. V. Mikhaylovskiy, A. V. Kimel, and S. Mizukami, *Laser stimulated thz emission from pt/coo/fecob*, Applied Physics Letters, 117 (2020).

[240] Y. Sasaki, K. Z. Suzuki, and S. Mizukami, *Annealing effect on laser pulse-induced thz wave emission in ta/cofeb/mgo films*, Applied Physics Letters, 111 (2017).

[241] K. Sato and E. Saitoh, *Spintronics for Next Generation Innovative Devices*, John Wiley & Sons, Ltd, 2015.

[242] M. Sato, T. Higuchi, N. Kanda, K. Konishi, K. Yoshioka, T. Suzuki, K. Misawa, and M. Kuwata-Gonokami, *Terahertz polarization pulse shaping with arbitrary field control*, Nature Photonics, 7 (2013), pp. 724–731.

[243] A. Schlegel, S. F. Alvarado, and P. Wachter, *Optical properties of magnetite (fe3o4)*, J. Phys. C Solid State Phys., 12 (1979), pp. 1157–1164.

[244] R. Schneider, M. Fix, J. Bensmann, S. Michaelis de Vasconcellos, M. Albrecht, and R. Bratschitsch, *Spintronic gdfe/pt thz emitters*, Applied Physics Letters, 115 (2019).

[245] T. Seifert, *Generation of intense and spectrally narrow terahertz pulses*, Master's thesis, Freie Universität Berlin, Berlin, 2013.

[246] T. Seifert, S. Jaiswal, U. Martens, J. Hannegan, L. Braun, P. Maldonado, F. Freimuth, A. Kronenberg, J. Henrizi, I. Radu, E. Beaurepaire, Y. Mokrousov, P. M. Oppeneer, M. Jourdan, G. Jakob, D. Turchinovich, L. M. Hayden, M. Wolf, M. Münzenberg, M. Kläui, and T. Kampfrath, *Efficient metallic spintronic emitters of ultrabroadband terahertz radiation*, Nature Photonics, 10 (2016), pp. 483–488.

[247] T. Seifert, S. Jaiswal, M. Sajadi, G. Jakob, S. Winnerl, M. Wolf, M. Kläui, and T. Kampfrath, *Ultrabroadband single-cycle terahertz pulses with peak fields of 300 kv cm^{-1} from a metallic spintronic emitter*, Applied Physics Letters, 110 (2017).

[248] T. S. SEIFERT, *Spintronics with Terahertz Radiation: Probing and driving spins at highest frequencies*, PhD thesis, Freie Universität Berlin, Berlin, 2017.

[249] T. S. SEIFERT, L. CHENG, Z. WEI, T. KAMPFRATH, AND J. QI, *Spintronic sources of ultrashort terahertz electromagnetic pulses*, Applied Physics Letters, 120 (2022), p. 180401.

[250] T. S. SEIFERT, S. JAISWAL, J. BARKER, S. T. WEBER, I. RAZDOLSKI, J. CRAMER, O. GUECKSTOCK, S. F. MAEHRLEIN, L. NADVORNIK, S. WATANABE, C. CICCARELLI, A. MELNIKOV, G. JAKOB, M. MUNZENBERG, S. T. B. GOENNENWEIN, G. WOLTERSDORF, B. RETHFELD, P. W. BROUWER, M. WOLF, M. KLAUI, AND T. KAMPFRATH, *Femtosecond formation dynamics of the spin seebeck effect revealed by terahertz spectroscopy*, Nature Communications, 9 (2018), p. 2899.

[251] T. S. SEIFERT, U. MARTENS, F. RADU, M. RIBOW, M. BERRITTA, L. NADVORNIK, R. STARKE, T. JUNGWIRTH, M. WOLF, I. RADU, M. MUNZENBERG, P. M. OPPENEER, G. WOLTERSDORF, AND T. KAMPFRATH, *Frequency-independent terahertz anomalous hall effect in dyco5 , co32 fe68 , and gd27 fe73 thin films from dc to 40 thz*, Adv Mater, 33 (2021), p. e2007398.

[252] T. S. SEIFERT, N. M. TRAN, O. GUECKSTOCK, S. M. ROUZEGAR, L. NADVORNIK, S. JAISWAL, G. JAKOB, V. V. TEMNOV, M. MÜNZENBERG, M. WOLF, M. KLÄUI, AND T. KAMPFRATH, *Terahertz spectroscopy for all-optical spintronic characterization of the spin-hall-effect metals pt, w and cu80ir20*, Journal of Physics D: Applied Physics, 51 (2018), p. 364003.

[253] F. N. SHAFIEE, M. S. MUSTAFFA, N. H. ABDULLAH, M. N. HAMIDON, I. ISMAIL, R. NAZLAN, I. R. IBRAHIM, F. M. IDRIS, AND M. S. E. SHAFIE, *Effect of microstructural evolution from nano to micron grain size regime towards structural, magnetic, electrical and microwave properties of gadolinium iron garnet (gd3fe5o12)*, Journal of Materials Science: Materials in Electronics, 32 (2021), pp. 10160–10179.

[254] M. SHALABY AND C. P. HAURI, *Demonstration of a low-frequency three-dimensional terahertz bullet with extreme brightness*, Nat Commun, 6 (2015), p. 5976.

[255] K. SHI, W. ZHANG, Z. NING, H. WANG, J. LIAO, Y. YANG, N. LIU, AND J. YANG, *Proton and au-ion irradiation induced damage and hardening in ferritic/martensitic steel*, Nuclear Materials and Energy, 26 (2021).

[256] P. H. SIEGEL, *Thz instruments for space*, IEEE Transactions on Antennas and Propagation, 55 (2007), pp. 2957–2965.

[257] A. SINGH, A. PASHKIN, S. WINNERL, M. HELM, AND H. SCHNEIDER, *Gapless broadband terahertz emission from a germanium photoconductive emitter*, ACS Photonics, 5 (2018), pp. 2718–2723.

[258] J. Sinova and I. Žutić, *New moves of the spintronics tango*, Nature Materials, 11 (2012), pp. 368–371.

[259] J. Sinova, S. O. Valenzuela, J. Wunderlich, C. H. Back, and T. Jungwirth, *Spin hall effects*, Reviews of Modern Physics, 87 (2015), pp. 1213–1260.

[260] A. Slachter, F. L. Bakker, J. P. Adam, and B. J. Van Wees, *Thermally driven spin injection from a ferromagnet into a non-magnetic metal*, Nature Physics, 6 (2010), pp. 879–882.

[261] L. Smejkal, J. Sinova, and T. Jungwirth, *Altermagnetism: a third magnetic class delimited by spinsymmetry groups*, arXiv, 2105.05820 (2021).

[262] M. P. Spencer, W. Lee, A. Alsaati, C. M. Breznak, R. Braga Nogueira Branco, J. Dai, E. D. Gomez, A. Marconnet, P. Lockette, and N. Yamamoto, *Cold sintering to form bulk maghemite for characterization beyond magnetic properties*, International Journal of Ceramic Engineering & Science, 1 (2019), pp. 119–124.

[263] J. Stöhr and H. C. Siegmann, *Magnetism: From Fundamentals to Nanoscale Dynamics*, Springer Series in Solid-State Sciences, Springer, 2006.

[264] F.-F. Stiewe, T. Winkel, Y. Sasaki, T. Tubandt, T. Kleinke, C. Denker, U. Martens, N. Meyer, T. S. Parvini, S. Mizukami, J. Walowski, and M. Münzenberg, *Spintronic emitters for super-resolution in thz-spectral imaging*, Applied Physics Letters, 120 (2022), p. 032406.

[265] S. Sugano and N. Kojima, *Magneto-Optics*, Springer, 2000.

[266] Q.-f. Sun and X. C. Xie, *Definition of the spin current: The angular spin current and its physical consequences*, Phys. Rev. B, 72 (2005), p. 245305.

[267] N. Thiery, V. V. Naletov, L. Vila, A. Marty, A. Brenac, J. F. Jacquot, G. de Loubens, M. Viret, A. Anane, V. Cros, J. Ben Youssef, N. Beaulieu, V. E. Demidov, B. Divinskiy, S. O. Demokritov, and O. Klein, *Electrical properties of epitaxial yttrium iron garnet ultrathin films at high temperatures*, Physical Review B, 97 (2018), p. 064422.

[268] W. Thomson, *Xix. on the electro-dynamic qualities of metals: Effects of magnetization on the electric conductivity of nickel and of iron*, Proceedings of the Royal Society of London, 8 (1857), pp. 546–550.

[269] M. Tonouchi, *Cutting-edge terahertz technology*, Nature Photonics, 1 (2007), pp. 97–105.

[270] Y. Tserkovnyak, A. Brataas, and G. E. W. Bauer, *Spin pumping and magnetization dynamics in metallic multilayers*, Physical Review B, 66 (2002).

[271] V. Tshitoyan, C. Ciccarelli, A. P. Mihai, M. Ali, A. C. Irvine, T. A. Moore, T. Jungwirth, and A. J. Ferguson, *Electrical manipulation of ferromagnetic nife by antiferromagnetic irmn*, Physical Review B, 92 (2015).

[272] R. P. Turner, *LC Circuits*, Howard W. Sams & Co., Indianapolis, 1980.

[273] K. Uchida, M. Ishida, T. Kikkawa, A. Kirihara, T. Murakami, and E. Saitoh, *Longitudinal spin seebeck effect: From fundamentals to applications (journal of physics condensed matter (2014) 26 (343202))*, Journal of Physics Condensed Matter, 26 (2014), pp. 343202–343202.

[274] K. I. Uchida, H. Adachi, T. Ota, H. Nakayama, S. Maekawa, and E. Saitoh, *Observation of longitudinal spin-seebeck effect in magnetic insulators*, Applied Physics Letters, 97 (2010), p. 172505.

[275] R. Ulbricht, E. Hendry, J. Shan, T. F. Heinz, and M. Bonn, *Carrier dynamics in semiconductors studied with time-resolved terahertz spectroscopy*, Rev. Mod. Phys., 83 (2011), pp. 543–586.

[276] P. Vaidya, S. A. Morley, J. v. Tol, Y. Liu, R. Cheng, A. Brataas, D. Lederman, and E. d. Barco, *Subterahertz spin pumping from an insulating antiferromagnet*, Science, 368 (2020), pp. 160–165.

[277] A. van den Brink, G. Vermijs, A. Solignac, J. Koo, J. T. Kohlhepp, H. J. M. Swagten, and B. Koopmans, *Field-free magnetization reversal by spin-hall effect and exchange bias*, Nat Commun, 7 (2016), p. 10854.

[278] K. Vandaele, S. J. Watzman, B. Flebus, A. Prakash, Y. Zheng, S. R. Boona, and J. P. Heremans, *Thermal spin transport and energy conversion*, Materials Today Physics, 1 (2017), pp. 39–49.

[279] H. B. Vasili, M. Gamino, J. Gazquez, F. Sanchez, M. Valvidares, P. Gargiani, E. Pellegrin, and J. Fontcuberta, *Magnetoresistance in hybrid pt/cofe2o4 bilayers controlled by competing spin accumulation and interfacial chemical reconstruction*, ACS Appl Mater Interfaces, 10 (2018), pp. 12031–12041.

[280] E. Y. Vedmedenko, R. K. Kawakami, D. D. Sheka, P. Gambardella, A. Kirilyuk, A. Hirohata, C. Binek, O. Chubykalo-Fesenko, S. Sanvito, B. J. Kirby, J. Grollier, K. Everschor-Sitte, T. Kampfrath, C. Y. You, and A. Berger, *The 2020 magnetism roadmap*, Journal of Physics D: Applied Physics, 53 (2020).

[281] I. D. Vugmeyster, J. F. Whitaker, and R. Merlin, *Gap based terahertz time-domain spectrometer optimized for the 5-8 thz range*, Applied Physics Letters, 101 (2012).

[282] P. Wadley, B. Howells, J. Železný, C. Andrews, V. Hills, R. P. Campion, V. Novák, K. Olejník, F. Maccherozzi, S. S. Dhesi, S. Y. Martin, T. Wagner, J. Wunderlich, F. Freimuth, Y. Mokrousov, J. Kuneš, J. S. Chauhan, M. J. Grzybowski, A. W. Rushforth, K. W. Edmonds, B. L. Gallagher, and T. Jungwirth, *Electrical switching of an antiferromagnet*, Science, 351 (2016), p. 587.

[283] M. A. Wahada, E. Şaşioğlu, W. Hoppe, X. Zhou, H. Deniz, R. Rouzegar, T. Kampfrath, I. Mertig, S. S. P. Parkin, and G. Woltersdorf, *Atomic scale control of spin current transmission at interfaces*, Nano Letters, 22 (2022), pp. 3539–3544.

[284] J. Walowski and M. Münzenberg, *Perspective: Ultrafast magnetism and thz spintronics*, Journal of Applied Physics, 120 (2016).

[285] H. Wang, C. Du, P. Chris Hammel, and F. Yang, *Spin current and inverse spin hall effect in ferromagnetic metals probed by y3fe5o12-based spin pumping*, Applied Physics Letters, 104 (2014).

[286] W. Wang, J. M. Mariot, M. C. Richter, O. Heckmann, W. Ndiaye, P. De Padova, A. Taleb-Ibrahimi, P. Le Fèvre, F. Bertran, F. Bondino, E. Magnano, J. Krempaský, P. Blaha, C. Cacho, F. Parmigiani, and K. Hricovini, *Fe t2g band dispersion and spin polarization in thin films of fe3o4(0 0 1)/mgo(0 0 1): Half-metallicity of magnetite revisited*, Physical Review B, 87 (2013), pp. 1–7.

[287] X. Wang, L. Cheng, D. Zhu, Y. Wu, M. Chen, Y. Wang, D. Zhao, C. B. Boothroyd, Y. M. Lam, J. X. Zhu, M. Battiato, J. C. W. Song, H. Yang, and E. E. M. Chia, *Ultrafast spin-to-charge conversion at the surface of topological insulator thin films*, Adv Mater, 30 (2018), p. e1802356.

[288] Y.-P. Wang, H. Zhou, L. Zhou, R. L. Headrick, A. T. Macrander, and A. S. Özcan, *Interface roughness evolution in sputtered wsi2/si multilayers*, Journal of Applied Physics, 101 (2007), p. 023503.

[289] D. H. Wei, Y. Niimi, B. Gu, T. Ziman, S. Maekawa, and Y. Otani, *The spin hall effect as a probe of nonlinear spin fluctuations*, Nat Commun, 3 (2012), p. 1058. Wei, D H Niimi, Y Gu, B Ziman, T Maekawa, S Otani, Y eng Research Support, Non-U.S. Gov't England Nat Commun. 2012;3:1058. doi: 10.1038/ncomms2063.

[290] M. Weiler, M. Althammer, M. Schreier, J. Lotze, M. Pernpeintner,

S. Meyer, H. Huebl, R. Gross, A. Kamra, J. Xiao, Y. T. Chen, H. Jiao, G. E. W. Bauer, and S. T. B. Goennenwein, *Experimental test of the spin mixing interface conductivity concept*, Physical Review Letters, 111 (2013), pp. 176601–176601.

[291] J. Weischenberg, F. Freimuth, J. Sinova, S. Blügel, and Y. Mokrousov, *Ab initio theory of the scattering-independent anomalous hall effect*, Phys. Rev. Lett., 107 (2011), p. 106601.

[292] A. W. J. Wells, P. M. Shepley, C. H. Marrows, and T. A. Moore, *Effect of interfacial intermixing on the dzyaloshinskii-moriya interaction in pt/co/pt*, Physical Review B, 95 (2017).

[293] S. H. Wemple, S. L. Blank, J. A. Seman, and W. A. Biolsi, *Optical properties of epitaxial iron garnet thin films*, Physical Review B, 9 (1974), pp. 2134–2144.

[294] R. M. White, *Quantum Theory of Magnetism*, Springer, 2007.

[295] J. Wieczorek, A. Eschenlohr, B. Weidtmann, M. Rösner, N. Bergeard, A. Tarasevitch, T. O. Wehling, and U. Bovensiepen, *Separation of ultrafast spin currents and spin-flip scattering in co/cu(001) driven by femtosecond laser excitation employing the complex magneto-optical kerr effect*, Physical Review B, 92 (2015).

[296] M. Wimmer, H. M. Price, I. Carusotto, and U. Peschel, *Experimental measurement of the berry curvature from anomalous transport*, Nature Physics, 13 (2017), pp. 545–550.

[297] S. A. Wolf, D. D. Awschalom, R. A. Buhrman, J. M. Daughton, S. Von Molnár, M. L. Roukes, A. Y. Chtchelkanova, and D. M. Treger, *Spintronics: A spin-based electronics vision for the future*, Science, 294 (2001), pp. 1488–1495.

[298] D. Wu, G. Yu, C.-T. Chen, S. A. Razavi, Q. Shao, X. Li, B. Zhao, K. L. Wong, C. He, Z. Zhang, P. Khalili Amiri, and K. L. Wang, *Spin-orbit torques in perpendicularly magnetized ir22mn78/co20fe60b20/mgo multilayer*, Applied Physics Letters, 109 (2016).

[299] L. Wu, A. Farid, N. J. Laurita, T. Mueller, and N. P. Armitage, *A compact broadband terahertz range quarter-wave plate*, Journal of Infrared, Millimeter, and Terahertz Waves, 41 (2020), pp. 642–654.

[300] Q. Wu and X. C. Zhang, *Ultrafast electro-optic field sensors*, Applied Physics Letters, 68 (1996), pp. 1604–1606.

[301] W. Wu, C. Yaw Ameyaw, M. F. Doty, and M. B. Jungfleisch, *Principles of spintronic thz emitters*, Journal of Applied Physics, 130 (2021).

[302] Y. Wu, M. Elyasi, X. Qiu, M. Chen, Y. Liu, L. Ke, and H. Yang, *High-performance thz emitters based on ferromagnetic/nonmagnetic heterostructures*, Adv Mater, 29 (2017).

[303] J. Xiao, G. E. W. Bauer, K. C. Uchida, E. Saitoh, and S. Maekawa, *Theory of magnon-driven spin seebeck effect*, Physical Review B - Condensed Matter and Materials Physics, 81 (2010), pp. 1–8.

[304] Y. Xu, D. D. Awschalom, and J. Nitta, *Handbook of Spintronics*, Springer Netherlands, Dordrecht, 1st ed. ed., 2016.

[305] Y. Yamamura, T. Takiguchi, and M. Ishida, *Energy and angular distributions of sputtered atoms at normal incidence*, Radiation Effects and Defects in Solids, 118 (1991), pp. 237–261.

[306] D. Yang, J. Liang, C. Zhou, L. Sun, R. Zheng, S. Luo, Y. Wu, and J. Qi, *Powerful and tunable thz emitters based on the fe/pt magnetic heterostructure*, Advanced Optical Materials, 4 (2016), pp. 1944–1949.

[307] C.-Y. You and S.-C. Shin, *Generalized analytic formulae for magneto-optical kerr effects*, Journal of Applied Physics, 84 (1998), pp. 541–546.

[308] X. Yu and W. C. Henneberger, *Origin of the darwin term*, Il Nuovo Cimento B (1971-1996), 109 (1994), pp. 439–442.

[309] Q. Zhang, Z. Luo, H. Li, Y. Yang, X. Zhang, and Y. Wu, *Terahertz emission from anomalous hall effect in a single-layer ferromagnet*, Physical Review Applied, 12 (2019), p. 054027.

[310] S. Zhang, Z. Jin, Z. Zhu, W. Zhu, Z. Zhang, G. Ma, and J. Yao, *Bursts of efficient terahertz radiation with saturation effect from metal-based ferromagnetic heterostructures*, Journal of Physics D: Applied Physics, 51 (2018).

[311] W. Zhang, M. B. Jungfleisch, W. Jiang, J. E. Pearson, and A. Hoffmann, *Spin pumping and inverse rashba-edelstein effect in nife/ag/bi and nife/ag/sb*, Journal of Applied Physics, 117 (2015).

[312] W. Zhang, M. B. Jungfleisch, W. Jiang, J. E. Pearson, A. Hoffmann, F. Freimuth, and Y. Mokrousov, *Spin hall effects in metallic antiferromagnets*, Phys Rev Lett, 113 (2014), p. 196602.

[313] W. Zhang, P. Maldonado, Z. Jin, T. S. Seifert, J. Arabski, G. Schmerber, E. Beaurepaire, M. Bonn, T. Kampfrath, P. M. Oppeneer, and D. Turchinovich, *Ultrafast terahertz magnetometry*, Nat Commun, 11 (2020), p. 4247.

[314] W. Zhang, V. Vlaminck, J. E. Pearson, R. Divan, S. D. Bader, and A. Hoffmann, *Determination of the pt spin diffusion length by spin-pumping and spin hall effect*, Applied Physics Letters, 103 (2013), p. 242414.

[315] X.-C. Zhang and J. Xu, *Introduction to THz wave photonics*, Springer, 2010.

[316] Z. Zhen-Yu, H. Sophie, and T. Jérôme, *THz generation by optical rectification and competition with other nonlinear processes*, Chinese Physics Letters, 25 (2008), pp. 1868–1870.

[317] C. Zhou, Y. P. Liu, Z. Wang, S. J. Ma, M. W. Jia, R. Q. Wu, L. Zhou, W. Zhang, M. K. Liu, Y. Z. Wu, and J. Qi, *Broadband terahertz generation via the interface inverse rashba-edelstein effect*, Phys Rev Lett, 121 (2018), p. 086801.

[318] Y.-H. Zhu, B. Hillebrands, and H. C. Schneider, *Spin-signal propagation in time-dependent noncollinear spin transport*, Physical Review B, 79 (2009).

[319] B. Zimmermann, K. Chadova, D. Ködderitzsch, S. Blügel, H. Ebert, D. V. Fedorov, N. H. Long, P. Mavropoulos, I. Mertig, Y. Mokrousov, and M. Gradhand, *Skew scattering in dilute ferromagnetic alloys*, Physical Review B, 90 (2014).

[320] I. Zutic, J. Fabian, and S. Das Sarma, *Spintronics: Fundamentals and applications*, Reviews of Modern Physics, 76 (2004), pp. 323–410.

List of Publications

Publications within this thesis

O. Gueckstock, L. Nádvorník, M. Gradhand, T. S. Seifert, G. Bierhance, R. Rouzegar, M. Wolf, M. Vafaee, J. Cramer, M. A. Syskaki, G. Woltersdorf, I. Mertig, G. Jakob, M. Kläui, T. Kampfrath. *Terahertz spin-to-charge conversion by interfacial skew scattering in metallic bilayers.* Adv. Mater. **33**, 2006281 (2021).

O. Gueckstock, L. Nádvorník, T. S. Seifert, M. Borchert, G. Jakob, Georg Schmidt, Georg Woltersdorf, M. Kläui, M. Wolf, T. Kampfrath. *Modulating the polarization of broadband terahertz pulses from a spintronic emitter at rates up to 10 kHz.* Optica **8**, 1013-1019 (2021).

O. Gueckstock, R. Lopes Seeger, T. S. Seifert, S. Auffret, S. Gambarelli, J. N. Kirchhof, K. I. Bolotin, V. Baltz, T. Kampfrath, L. Nádvorník. *Impact of gigahertz and terahertz transport regimes on spin propagation and conversion in the antiferromagnet IrMn.* Appl. Phys. Lett. **120**, 062408 (2022).

P. Jimenez-Cavero, **O. Gueckstock**, L. Nádvorník, I. Lucas, T. S. Seifert, M. Wolf, R. Rouzegar, P. W. Brouwer, S. Becker, G. Jakob, M. Kläui, C. Guo, C. Wan, X. Han, Z. Jin, H. Zhao, D. Wu, L. Morellon, T. Kampfrath. *Transition of laser-induced terahertz spin currents from torque- to conduction-electron-mediated transport.* Phys. Rev. B **105**, 184408 (2022).

O. Gueckstock, N. Stojanovic, T. S. Seifert, T. Kampfrath, M. Gensch. *Radiation hardness of spintronic terahertz emitters.* in preparation (2022).

Publications concerning other topics

T. S. Seifert, S. Jaiswal, J. Barker, S.T. Weber, I. Razdolski, J. Cramer, **O. Gueckstock**, S. Maehrlein, L. Nadvornik, S. Watanabe, C. Ciccarelli, A. Melnikov, G. Jakob, M. Münzenberg, S.T.B. Goennenwein, G. Woltersdorf, B. Rethfeld, P.W. Brouwer, M. Wolf, M. Kläui, T. Kampfrath. *Femtosecond formation dynamics of the spin Seebeck effect revealed by terahertz spectroscopy.* Nat. Commun. **9**, 2899 (2018).

T. S. Seifert, N.M. Tranh, **O. Gueckstock**, S.M. Rouzegar, L. Nádvorník, S. Jaiswal, G. Jakob, V. Temnov, M. Münzenberg, M. Wolf, M. Kläui, T. Kampfrath. *Terahertz spectroscopy for all-optical spintronic characterization of the spin-Hall-effect metals Pt, W and $Cu_{80}Ir_{20}$.* J. Phys. D: Appl. Phys. **51**, 364003 (2018).

U. Nandi, M.S. Abdelaziz, S. Jaiswal, G. Jakob, **O. Gueckstock**, S.M. Rouzegar, T.S. Seifert, M. Kläui, T. Kampfrath, and S. Preu. *Antenna-coupled spintronic terahertz emitters driven by a 1550 nm pulsed laser.* Appl. Phys. Lett. **115**, 022405 (2019).

U. Nandi, M.S. Abdelaziz, S. Jaiswal, G. Jakob, **O. Gueckstock**, S.M. Rouzegar, T.S. Seifert, M. Kläui, T. Kampfrath, S. Preu. *Effect of DC Electric Field on the Emitted THz Signal of Antenna-Coupled Spintronic Emitters.* 2019 44$^{\text{th}}$ International Conference on Infrared, Millimeter, and Terahertz Waves (IRMMW-THz), IEEE (2019).

M. Meinert, B. Gliniors, **O. Gueckstock**, T. S. Seifert, L. Liensberger, M. Weiler, S. Wimmer, H. Ebert, T. Kampfrath. *High-Throughput Techniques for Measuring the Spin Hall Effect.* Phys. Rev. Applied **14**, 064011 (2020).

D. Yagodkin, L. Nádvorník, **O. Gueckstock**, C. Gahl, T. Kampfrath, K. I. Bolotin. *Ultrafast photocurrents in MoSe$_2$ probed by terahertz spectroscopy.* 2D Mater. **8**, 025012 (2021).

W. Hoppe, J. Weber, S. Tirpanci, **O. Gueckstock**, T. Kampfrath, G. Woltersdorf. *On-Chip Generation of Ultrafast Current Pulses by Nanolayered Spintronic Terahertz Emitters.* ACS Appl. Nano Mater., **4**, 7454-7460 (2021).

G. Bierhance, A. Markou, **O. Gueckstock**, R. Rouzegar, Y. Behovits, A. L. Chekhov, M. Wolf, T. S. Seifert, C. Felser, T. Kampfrath. *Spin-voltage-driven efficient terahertz spin currents from the magnetic Weyl semimetals Co$_2$MnGa and Co$_2$MnAl.* Appl. Phys. Lett. **120**, 082401 (2022).

R. Rouzegar, L. Brandt, L. Nádvorník, D. A. Reiss, A. L. Chekhov, **O. Gueckstock**, C. In, M. Wolf, T. S. Seifert, P. W. Brouwer, G. Woltersdorf, T. Kampfrath. *Laser-induced terahertz spin transport in magnetic nanostructures arises from the same force as ultrafast demagnetization.* arXiv:2103.11710, accepted for publication in Phys. Rev. B (2022).

E. Rongione, **O. Gueckstock**, M. Mattern, O. Gomonay, H. Meer, C. Schmitt, E. Saitoh, J. Sinova, H. Jaffres, T. Kampfrath, M. Kläui, M. Bargheer, T. S. Seifert, S. Dhillon, R. Lebrun. *Emission of coherent THz magnons in an antiferromagnetic insulator triggered by ultrafast spin-phonon interactions.* arXiv:2205.11965, under review in Nat. Commun. (2022).

L. Nádvorník, **O. Gueckstock**, L. Braun, C. Niu, J. Gräfe, G. Richter, G. Schütz, H. Takagi, T. S. Seifert, P. Kubaščík, A. K. Pandeya, A. Anane, H. Yang, A. Bedoya-Pinto, S. S. P. Parkin, M. Wolf, Y. Mokrousov, H. Nakamura, T. Kampfrath. *Terahertz spin-to-charge current conversion in stacks of ferromagnets and the transition-metal dichalcogenide NbSe$_2$.* arXiv:2208.00846, under review in Adv. Mat. Interfaces (2022).

Academic curriculum vitae

Oliver Philipp Gückstock
14195 Berlin

Der Lebenslauf ist in dieser Version aus Gründen des Datenschutzes nicht enthalten.

Acknowledgments

Selbstständigkeitserklärung

Ich erkläre gegenüber der Freien Universität Berlin, dass ich die vorliegende Dissertation selbstständig und ohne Benutzung anderer als der angegebenen Quellen und Hilfsmittel angefertigt habe. Die vorliegende Arbeit ist frei von Plagiaten. Alle Ausführungen, die wörtlich oder inhaltlich aus anderen Schriften entnommen sind, habe ich als solche kenntlich gemacht. Diese Dissertation wurde in gleicher oder ähnlicher Form noch in keinem früheren Promotionsverfahren eingereicht.

Mit einer Prüfung meiner Arbeit durch ein Plagiatsprüfungsprogramm erkläre ich mich einverstanden.

Berlin, den

Oliver Philipp Gückstock